FNAL--

Centro de Investigación y de Estudios Avanzados
del I.P.N.

Búsqueda de Producción Anómala
$$WW/WZ \rightarrow e\nu jj \text{ en DØ}$$

TESIS

Presentada al Departamento de Física como

requesito parcial para la obtención del

grado de DOCTOR EN CIENCIAS

en la especialidad de Física

por

Alberto Sánchez Hernández

México D.F., MÉXICO

Febrero de 1997

Centro de Investigación y de Estudios Avanzados
del I.P.N.

Search for Anomalous $WW/WZ \rightarrow e\nu jj$ Production at DØ

DISSERTATION

Submitted to the Physics Department

in Partial Fulfillment of the Requirements

for the Degree of

DOCTOR OF PHILOSOPHY

in

Physics

by

Alberto Sánchez Hernández

Mexico City, MEXICO

February 1997

DISCLAIMER

DISCLAIMER

Portions of this document may be illegible in electronic image products. Images are produced from the best available original document.

Centro de Investigacion y de Estudios Avanzados

Physics Department

Alberto Sánchez Hernández

We, the dissertation committee for the above candidate for the Doctor of Philosophy degree, accept the dissertation "Search for Anomalous $WW/WZ \to e\nu jj$ Production at DØ."

_____

Heriberto Castilla Valdez, Ph.D. (director)
CINVESTAV-IPN

_____

Henry Eugene Fisk, Ph.D.
FERMILAB

_____

Augusto García González, Ph.D.
CINVESTAV-IPN

_____

Miguel Angel Pérez Angón, Ph.D.
CINVESTAV-IPN

_____

Modesto Antonio Sosa Aquino, Ph.D.
Universidad de Guanajuato

_____

Takahiro Yasuda, Ph.D.
Northeastern University

Mexico City, MEXICO

February 1997

Abstract

A search for anomalous WW and WZ production in $p\bar{p}$ collisions at $\sqrt{s} = 1.8$ TeV using the DØ detector at Fermilab is presented. With a data sample of $p\bar{p} \rightarrow e\nu jjX$ events corresponding to an integrated luminosity of $76.5 \pm 4.1\mathrm{pb}^{-1}$, 399 candidate events were identified, from which, 387.1 ± 39.8 events were estimated to be background. No deviations from the Standard Model were seen, which predicts 16.2 ± 2.7 events. The 95% CL limit on the cross section $\sigma(p\bar{p} \rightarrow W^+W^-X)$ was calculated to be 93.8 pb. Limits on the CP-conserving anomalous $WW\gamma$ and WWZ coupling parameters were obtained from a binned likelihood fit to the transverse momentum spectrum of the W boson. Assuming that the $WW\gamma$ and WWZ coupling parameters are equal, the 95% CL limits on the CP-conserving couplings are $-0.56 < \Delta\kappa < 0.75$ (with $\lambda = 0$) and $-0.42 < \lambda < 0.44$ (with $\Delta\kappa = 0$), for a form factor scale $\Lambda_{FF} = 1.5$ TeV. Limits on other assumptions are also reported.

These results were combined with the previous DØ $WW, WZ \rightarrow e\nu jj$ published results ($13.7 \pm 0.7\mathrm{pb}^{-1}$), and the limits on the anomalous coupling parameters were set to $-0.44 < \Delta\kappa < 0.60$ (with $\lambda = 0$) and $-0.34 < \lambda < 0.37$ (with $\Delta\kappa = 0$), for a form factor scale $\Lambda_{FF} = 2.0$ TeV.

Resumen

Las autointeracciones de los bosones de norma son una consecuencia directa de
la simetría de norma no Abeliana del Modelo Estándar. Estas pueden ser confirmadas
a través del estudio de la producción de pares de bosones de norma en colisiones $p p$
a la energía del Tevatron en FERMILAB, $\sqrt{s} = 1.8$ TeV. Dado que estos procesos
no han sido medidos con suficiente precisión es factible que surjan indicios de Física
nueva, más allá del Modelo Estándar, a través de la manifestación de acoplamientos
anómalos de los bosones de norma. En esta tesis se presenta la determinación de
límites en los acoplamientos anómalos de $WW\gamma$ y WWZ obtenidos a partir de la
búsqueda de eventos $p\bar{p} \rightarrow WWX$ seguido de $W \rightarrow e\nu$ y $W \rightarrow jj$. y $pp \rightarrow WZX$
seguido de $W \rightarrow e\nu$ y $Z \rightarrow jj$, donde j representa un chorro de hadrones (jet).

Este análisis utiliza datos tomados con el detector DØ en FERMILAB durante
la operación en modo de colisionador 1993-1995 correspondiente a 76.5 ± 4.1 pb^{-1}. La
muestra de datos fue obtenida con un filtro para un candidato a electrón con energía
transversa $E_T > 20$ GeV y suficiente energía transversa faltante $\not{E}_T > 15$ GeV. La
selección de eventos posterior requirió que este candidato a electrón estuviera en la

región del calorímetro determinada por $|\eta| < 1.1$ ó $1.5 < |\eta| < 2.5$. El candidato a electrón además debería safisfacer los requerimientos: (i) fracción de energía electromagnética mayor que 0.9; (ii) forma longitudinal y tranversal consistente con la de un electrón; (iii) aislamiento menor que 0.1; y (iv) deberá existir una traza asociada en el detector central. El decaimiento $W{\rightarrow}e\nu$ fue identificado requiriendo un electrón con $E_T^e > 25$ GeV y una energía transversa faltante de $\not{E}_T > 25$ GeV formando una masa transversal $M_T^{e\nu} > 40$ GeV/c^2. Los jets fueron reconstruidos aplicando el algoritmo de cono con radio $\mathcal{R} = 0.5$. Se requirió que cada jet estuviera en la región del calorímetro determinada por $|\eta| < 2.5$ y que satisfaciera requerimientos estándares de selección. Los eventos candidatos deberán tener al menos 2 jets con $E_T^j > 20$ GeV y una masa invariante del sistema bijet, $50 < M_{jj} < 110$ GeV, consistente con las masas invariantes de los bosones de norma W y Z. Este proceso de selección identificó 399 eventos candidatos.

Las estimaciones de ruido incluyen contribuciones de: producción QCD de eventos $W + \geq 2$ jets; eventos QCD con muchos jets, donde un jet es erróneamente identificado como un electrón y además se mide suficiente energía transversa faltante; $t\bar{t}{\rightarrow}W^+\bar{b}W^-b{\rightarrow}e\nu jjX$; WW, WZ con $W{\rightarrow}\tau\nu jj$ seguido de $\tau{\rightarrow}e\nu\nu$; $ZX{\rightarrow}eeX$ donde uno de los electrones no fue reconstruido; y $ZX{\rightarrow}\tau\tau{\rightarrow}e\nu jjX'$. El ruido proveniente de eventos QCD con muchos jets fue estimado de una muestra de control utilizando métodos estándares. El ruido $W + \geq 2$ jets fue estimado usando el generator de eventos de Monte Carlo VECBOS seguido de un proceso de hadronización mediante

el programa HERWIG y una simulación completa del detector. El ruido debido a los procesos $t\bar{t} \to W^+bW^-b$, $WW/WZ \to \tau\nu jj$, $ZX \to eeX$ y $ZX \to \tau\tau$ fue estimado usando los generadores de eventos ISAJET y PYTHIA seguido de una simulación completa del detector y se encontró que su contribución era pequeña. El número total estimado de eventos provenientes de estas fuentes de ruido fue 387.1 ± 39.8. No se observó niguna señal estadísticamente significativa por encima del ruido, ni exceso de eventos con grandes momentos tranversos (p_T^W).

El estudio de eficiencias del proceso de identificación de electrones de realizó empleando datos del tipo $Z \to ee$ mientras el estudio de eficiencias para la selección de $W \to jj$ fue realizado utilizando multiples muestras de eventos generados con ISAJET y PYTHIA seguidos de una simulación completa del detector. Las prediciones para producción de WW y WZ en el Modelo Estándar y acoplamientos anómalos fueron obtenidas usando el programa de generación de eventos de Monte Carlo de Zeppenfeld, en el cual los procesos son generados a primer orden y las correcciones para ordenes superiores fueron aproximadas mediante un factor-K y la inclusión de los efectos de movimiento de retroceso del sistema de acuerdo al espectro p_T medido para el bosón Z. Los efectos del detector fueron incluidos a través de las funciones de resolución y eficiencias. Así, la eficiencia total para acoplamientos dentro del Modelo Estándar se estimó en $(14.7 \pm 1.2)\%$ para WW y $(14.6 \pm 1.2)\%$ para WZ. El número total de eventos predicho por el Modeo Estándar es 16.2 ± 2.7. Se calculó el límite superior en la sección eficaz $\sigma(p\bar{p} \to W^+W^-X)$ al 95% de nivel de confiabilidad en 93.8 pb.

La ausencia de un exceso de eventos con grandes momentos transversales p_T^W excluye grandes desviaciones de los acoplamientos del Modelo Estándar. Para establecer límites en los parámetros que miden los acoplamientos anómalos de $WW\gamma$ y WWZ se comparó, utilizando un ajuste likelihood, el momento transverso del bosón W de los candidatos con diversas muestras de acoplamientos anómalos a los que se les agregó la estimación de ruido. Las incertidumbres en la estimación de ruido, eficiencias, luminosidad integrada y estimaciones teóricas fueron incorporadas al ajuste permitiendo que los valores nominales fluctuaran con distribuciones Gaussianas. Suponiendo que los parámetros de acoplamiento para WWZ son iguales a los $WW\gamma$: $\Delta\kappa = \Delta\kappa_\gamma = \Delta_Z$ y $\lambda = \lambda_\gamma = \lambda_Z$; los límites preliminares a 95% de nivel de confiabilidad obtenidos fueron $-0.56 < \Delta\kappa < 0.75$ (con $\lambda = 0$) y $-0.42 < \lambda < 0.44$ (con $\Delta\kappa = 0$) para una escala del factor de forma de $\Lambda_{FF} = 1.5$ TeV. También se estimaron límites considerando otras relaciones entre los parámetros de acoplamiento.

Los resultados fueron combinados con el resultado previo de DØ correspondiente a $13.7 \pm 0.7\text{pb}^{-1}$. Los límites preliminares en los parámetros de acoplamiento obtenidos fueron $-0.44 < \Delta\kappa < 0.60$ (con $\lambda = 0$) y $-0.34 < \lambda < 0.37$ (con $\Delta\kappa = 0$) para una escala del factor de forma de $\Lambda_{FF} = 2.0$ TeV.

Acknowledgments

My sincere thanks go to all the people who have devoted so much of their knowledgement and time to help me reach this point. Some of them deserve special mention. First of all I am grateful to all members of the DØ Collaboration for their hard work building and operating the detector successfully and making this analysis possible. Special thanks go to my thesis director, Heriberto Castilla Valdez, for the support and advice he has provided over the last few years. I also thank to him for allowing me to graduate in a reasonable time. I thank to H. Eugene Fisk and Miguel Angel Pérez Angón for providing economical support (through the DØ Department and CINVESTAV respectively) during my stay at FERMILAB.

I have also been fortunate to have worked with Takahiro Yasuda, who in the last months provided advice and took so much of his time reviewing my plots. Nobuoki Oshima helped with the Monte Carlo simulation and gave useful inputs. Ling-Ping Chen performed the 1A analysis and shared many of his software programs. I also thank my colleagues in the Diboson and Electroweak analysis groups for their valuable

Agradecimientos

To my family with love and gratitude.

A mi familia con amor y gratitud.

Contents

List of Tables

List of Figures

Chapter 1

Introduction

Since the beginning of history, human beings have always tried to explain their surrounding world. Several theories have been formulated to achieve this goal. In the last 30 years we have witnessed the extraordinary success of one of these theories, the Standard Model (SM). The development of the Standard Model has been the recent major achievement in understanding the universe. Since its formulation by S. Weinberg, A. Salam, and S. L. Glashow in the 60's [1], the Standard Model has been tested many times experimentally, and it has not seen any serious deviation from its predictions.

In the present work a direct test of the SM has been performed. We have searched for $WW\gamma$ and WWZ anomalous couplings production at $\sqrt{s} = 1.8$ TeV. Since the gauge boson self-couplings have not yet been measured with good precision, it is possible in principle that the new physics beyond the SM will demostrate itself

in this sector through the existence of anomalous trilinear gauge boson couplings.

This thesis is organized as follows. The theoretical and experimental background on WWZ and $WW\gamma$ production is discussed in chapter 2. Chapter 3 describes the experimental apparatus. The trigger and identification of objects are discussed in chapter 4. Chapter 5 explains the event selection that we applied to study WWZ and $WW\gamma$ vertices. The background studies are addressed in chapter 6. Chapter 7 describes the efficiencies, predictions and uncertainties. The results are shown in chapter 8 and the conclusions are presented in chapter 9.

Chapter 2

Theoretical Background

This chapter will briefly describe the Standard Model. Special emphasis will be placed on the electroweak sector. A discussion on gauge boson self-interactions is also included. At the end, a review of previous experimental results on trilinear gauge boson couplings is presented. The discussion will be from the experimental point of view rather than a rigorous mathematical one.

2.1 The Standard Model

High energy physics is the science of the fundamental nature of matter [2, 3]. Its objective is to find the truth about the way our world and our universe work. In order to achieve this goal Physicists have developed a theory called the Standard Model that attempts to describe all matter and forces in the universe (except for gravity[1]). The

---

[1] Although gravity has not been incorporated into the SM, its effects are negligible at present energies.

Standard Model is a surprisingly simple picture of the world of so-called elementary particles and the laws they obey. Many people have contributed to its development, among which S.L. Glashow, S. Weinberg, and A. Salam [1] deserve special credit.

According to the Standard Model, the most fundamental particles[2] fall into three categories: the leptons, the quarks, and the gauge bosons. Leptons include the electrically charged electrons, two similar unstable particles, heavier than electrons (called muons and taus), and three neutral particles called neutrinos[3]. Two kinds of quarks, called "up" and "down", make up the protons and neutrons, but heavier, less stable quarks also exist: strange, charm, bottom, and top. Quarks have the unusual characteristic of having fractional electric charge of either 2/3 or -1/3, unlike the -1 charge of an electron. Quarks also carry another type of charge called color charge. The leptons and quarks have odd-half-integer intrinsic angular momentum (spin), and they obey the Pauli Exclusion Principle. Gauge bosons give rise to the strong, weak, and electromagnetic forces, which govern the interaction of the quarks and leptons. The photon transmits the electromagnetic force, the $W^{\pm}$ and Z bosons transmit the weak force, and gluons transmit the strong force. These gauge bosons are spin-1 particles.

---

[2] We have to point out that for every particle (matter) there is a corresponding antiparticle (antimatter). Antiparticles are the same as the corresponding matter particle in every respect except for their opposite charges. But there are some particles which are their own antiparticles, like the photon and Z boson, they are called Majorana particles.

[3] Neutrinos have no charge, and little, if any, mass and because of their weak coupling, they almost never interact with other particles.

In the Standard Model the weak and the electromagnetic interactions are combined into a unified electroweak theory. The present work is focussed on this sector of the Standard Model. To provide a framework, in the next section we will briefly discuss the electroweak sector of the Standard Model.

2.2 Electroweak Interactions

The Standard Model of electroweak interactions is based on the gauge group $SU(2)_L \times U(1)_Y$ [4, 5]. To construct the theory, four gauge bosons, W_μ^i ($i = 1, 2, 3$) for $SU(2)_L$ and B_μ for $U(1)_Y$, are introduced. The fermions are introduceed as left-handed and right-handed fields, which interact with these gauge bosons. The left-handed fermion fields

$$\begin{pmatrix} \nu_{Li} \\ l_{Li}^- \end{pmatrix} \quad \text{and} \quad \begin{pmatrix} u_{Li} \\ d'_{Li} \end{pmatrix} \quad \text{of the } i^{th} \text{ fermion family}$$

must transform as isospin doublets under $SU(2)$, where $d'_i = \sum_j V_{ij} d_j$, and V is the Cabibbo-Kobayashi-Maskawa mixing matrix. The right-handed fields are weak-isospin singlets under $SU(2)$

$$l_{Ri} \text{ and } u_{Ri}, \quad d_{Ri}.$$

The Abelian group $U(1)_Y$ is associated with a new quantum number Y called the *weak hypercharge*, which is related to the electric charge (Q) and the weak-isospin (I) by the Gell-Mann-Nishijima relation: $Q = I_3 + Y/2$ (I_3 is the 3-projection of I).

Now, a scalar field (the Higgs field) is introduced to give masses to the gauge bosons and the fermions via spontaneous local symmetry breaking (LSB) (Higgs mechanism), in a manner consistent with low-energy phenomenology, e.g. the photon is massless. The complex doublet of scalar fields which transforms as an $SU(2)_L$ doublet is

$$\begin{pmatrix} \phi^+ \\ \phi^0 \end{pmatrix} \xrightarrow{LSB} \frac{1}{\sqrt{2}} \begin{pmatrix} 0 \\ v + H \end{pmatrix}$$

where v is the vaccum expectation value of the scalar field in the spontaneously broken $SU(2)_L \times U(1)_Y$ symmetry and H represents excitations above the minimum of the potential.

After spontaneous symmetry breaking the Lagrangian density of the standard electroweak model can be considered to be the sum of:

$$\mathcal{L} = \mathcal{L}_g + \mathcal{L}_f + \mathcal{L}_s + \mathcal{L}_{f-s}$$

where $\mathcal{L}_f$ represents the Lagrangian density for the fermion fields and their couplings to the gauge fields, $\mathcal{L}_s$ for the scalar fields, $\mathcal{L}_{f-s}$ determines the couplings between the fermions and the scalar fields (sometimes called Yukawa term), and $\mathcal{L}_g$ for the gauge fields. This last term is responsible for cubic and quartic self-interactions of the gauge fields

$$\mathcal{L}_g = -\frac{1}{4} W_{i\mu\nu} W_i^{\mu\nu} - \frac{1}{4} B_{\mu\nu} B^{\mu\nu},$$

with the field-strength tensors $W_{i\mu\nu}$ and $B_{\mu\nu}$:

$$W_{i\mu\nu} = \partial_\mu W_{i\nu} - \partial_\nu W_{i\mu} - g\varepsilon_{ijk}W_{j\mu}W_{k\nu};$$

$$B_{\mu\nu} = \partial_\mu B_\nu - \partial_\nu M_\mu,$$

where ε_{ijk} are the structure constants of the isospin group $SU(2)$: $[\tau^i, \tau^j] = 2i\varepsilon_{ijk}\tau^k$. There are three free independent parameters which determine the gauge sector of the standard Model: g, g' [4], and $v = 2m_W/g = (\sqrt{2}\,G_F)^{-1/2}$. For low energy electroweak interactions an equivalent set of parameters is used: [6] the fine structure constant $\alpha = e^2/(4\pi) = 1/(137.0359895 \pm 0.0000061)$, the Fermi coupling constant $G_F = (1.16639 \pm 0.00002) \times 10^{-5}$ GeV^{-2}, and the Weinberg angle θ_W, $\sin^2\theta_W = 0.2315 \pm 0.0005$. In this scheme the Glashow-Weinberg-Salam (GWS) electroweak theory is renormalizable as was proved by t'Hooft [7]. This fact allows radiative corrections in a well defined way. This theory has amazing predictions some of which have already been proved with very high accuracy.

2.3 Gauge Boson Self-interactions

The Tevatron offers the best opportunity to test the non-Abelian self-couplings of the W, Z, and γ bosons, which are a direct consequence of the gauge structure of the Standard Model [8, 9, 10, 11, 12, 13, 14, 15]. The gauge boson self-couplings can be studied through the gauge boson pair (diboson) production processes. In this section, the mathematical formalism [16] of the gauge boson self-interactions is presented.

---

[4]g is the coupling constant for the weak-isospin group $SU(2)_L$ and $g'/2$ is the coupling constant for the weak-hypercharge group $U(1)_Y$.

In the Standard Model, the direct WW and WZ production in $p\bar{p}$ collisions at $\sqrt{s} = 1.8$ TeV occurs in the s-channel boson exchange [17], as shown in Fig. 2.1. At tree level, the WW or WZ final state can also be generated by the $t-$ or $u-$channel quark exchange. There are substantial cancellations between the $t-$ or $u-$ diagrams, which involve only the couplings of the bosons to fermions, and the $s-$ channel diagrams which contains the three boson couplings. These cancellations result in Standard Model cross sections of 9.5 pb and 2.5 pb [16] for WW and WZ production, respectively. Since the fermionic couplings of the W, Z, and γ have been well tested [18], we may regard diboson production as primarily a test of the three-boson couplings. The $s-$channel WW production is sensitive to $WW\gamma$ and WWZ couplings, and WZ production is sensitive to the WWZ couplings.

In order to quantify the WWV couplings a generalized effective Lagrangian has been developed to describe the WWV vertex [19]. The Lorentz invariant effective Lagrangian for the gauge boson self-interactions contains fourteen dimensionless coupling parameters, seven parameters for WWZ and another seven for $WW\gamma$:

$$
\begin{aligned}
\mathcal{L}_{WWV}/g_{WWV} = \quad & ig_1^V \left(W_{\mu\nu}^\dagger W^\mu V^\nu - W_\mu^\dagger V_\nu W^{\mu\nu} \right) + i\kappa_V W_\mu^\dagger W_\nu V^{\mu\nu} \\
& + \frac{i\lambda_V}{M_W^2} W_{\lambda\mu}^\dagger W_\nu^\mu V^{\nu\lambda} - g_4^V W_\mu^\dagger W_\nu \left(\partial^\mu V^\nu + \partial^\nu V^\mu \right) \\
& + g_5^V \epsilon^{\mu\nu\rho\sigma} \left(W_\mu^\dagger \overset{\leftrightarrow}{\partial}_\rho W_\nu \right) V_\sigma + i\tilde{\kappa}_V W_\mu^\dagger W_\nu \tilde{V}^{\mu\nu} \\
& + \frac{i\tilde{\lambda}_V}{M_W^2} W_{\lambda\mu}^\dagger W_\nu^\mu \tilde{V}^{\nu\lambda}
\end{aligned}
$$

where V^μ stands for photon or Z field, corresponding to $V = \gamma$ or Z respectively, W^μ denotes the W^- field, $W_{\mu\nu} = \partial_\mu W_\nu - \partial_\nu W_\mu$, $V_{\mu\nu} = \partial_\mu V_\nu - \partial_\nu V_\mu$, $\tilde{V}_{\mu\nu} = \frac{1}{2}\epsilon_{\mu\nu\rho\sigma} V^{\rho\sigma}$,
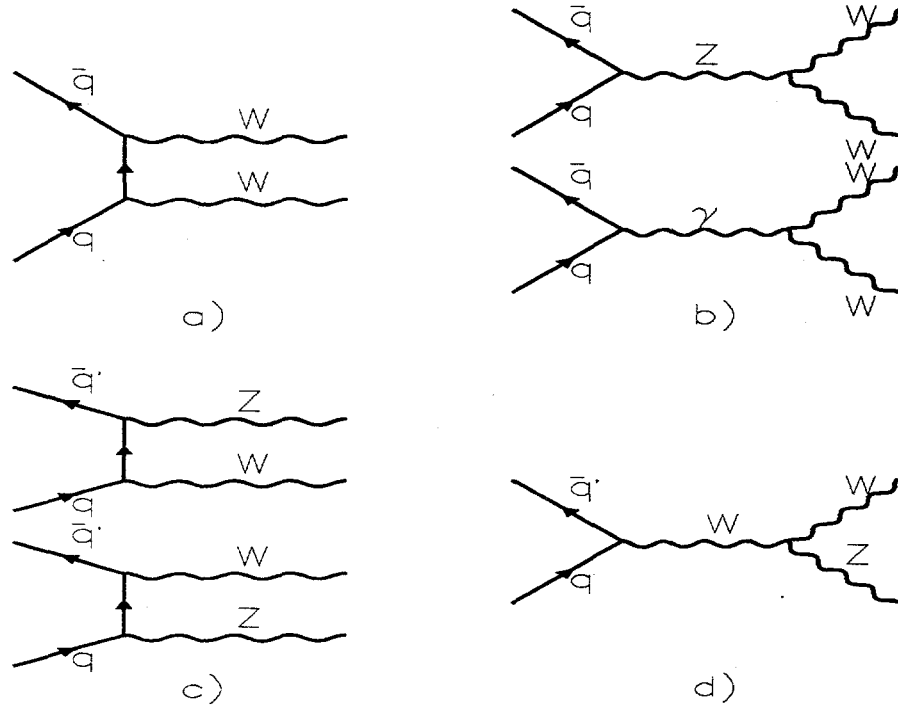
Figure 2.1: Feynman diagrams for WW and WZ production at leading order. a), c): $t-$, $u-$channel, fermion-boson couplings; b), d): $s-$channel boson-boson couplings.

and $(A \overset{\leftrightarrow}{\partial_\mu} B) = A(\partial_\mu B) - (\partial_\mu A)B$. M_W is the mass of the W boson. The overall couplings g_{WWV} are $g_{WW\gamma} = -e$ and $g_{WWZ} = -e(\cot \theta_W)$ as in the SM, where e and θ_W are the positron charge and the weak mixing angle. The couplings λ_V and κ_V conserve C and P. The couplings g_4^V are odd under CP and C, g_5^V are odd under C and P, and $\tilde{\kappa}_V$ and $\tilde{\lambda}_V$ are odd under CP and P. Within the SM at tree level, all these couplings are zero except g_1^V and κ_V ($g_1^\gamma = g_1^Z = \kappa_\gamma = \kappa_Z = 1$). Electromagnetic gauge invariance forbids any deviations of g_1^γ, g_4^γ, and g_5^γ from their SM values 1, 0, and 0, respectively, for on shell photons. The CP-violating $WW\gamma$ couplings $\tilde{\lambda}_\gamma$ and $\tilde{\kappa}_\gamma$ are tightly constrained by measurements of the neutron electric dipole moment [20]. In

the present study the C, P and CP symmetries are assumed, reducing the number of

couplings parameters to five : κ_V, λ_V, and g_1^Z (where $V = \gamma$, Z). Further assumptions

will reduce the number of couplings parameters to two [21, 22]. This will be discussed

later. The CP-conserving $WW\gamma$ couplings parameters are related to the magnetic

dipole moment (μ_W) and electric quadrupole moment (Q_W^e) of the W boson [23]:

$$\mu_{W+} = \frac{e}{2M_W}(1 + \kappa_\gamma + \lambda_\gamma),$$

$$Q_{W+}^e = -\frac{e}{M_W^2}(\kappa_\gamma - \lambda_\gamma).$$

2.3.1 Signatures for Anomalous Couplings

Since the gauge boson self-interactions have not yet been measured with good

precision, it is possible in principle that signals for new physics beyond the Standard

Model will exhibit themselves in this sector. Thus, any non-SM couplings would mean

a violation of the SM, and they are usually referred to as *anomalous couplings*.

If all the coupling parameters for the WWZ vertex take the Standard Model

values except for κ and λ, the reduced amplitudes of the s-channel diagram for $q\bar{q} \rightarrow$

WZ would have the form [16]

$$\mathcal{A}(0, \pm) = a\sqrt{\hat{s}}(\kappa - 1 + \lambda)$$

$$\mathcal{A}(\pm, 0) = b\sqrt{\hat{s}}\,\lambda$$

$$\mathcal{A}(\pm, \pm) = (\kappa - 1)/2 + c\hat{s}\lambda$$

$$\mathcal{A}(0, 0) = d(\kappa - 1) + e\lambda$$

where a, b, c, d, and e are parameters independent of the center of mass energy ($\sqrt{\hat{s}}$). Similar expressions can be derived for W^+W^- production [19]. For finite and constant values of κ and/or λ it is obvious that the reduced amplitudes will grow as $\sqrt{\hat{s}}$ increases. This results in unphysically large cross sections at high energy (which violate tree-level unitarity) and also leads to a substantial overestimate of experimental sensitivities. A consistent description hence requires κ and λ to show a form factor behavior which causes them to vanish at very high energies. Here we will use the simple power law

$$\lambda_V(\hat{s}) = \frac{\lambda_V^0}{(1 + \hat{s}/\Lambda_{FF}^2)^n}$$

and similarly for the other parameters. For WWV we shall use the exponent $n = 2$. The form factor with $n = 2$ is referred to as the dipole form factor. Λ_{FF} is a phenomenological parameter which must be chosen a priori. The physical meaning of this parameter is the scale of energy where the new physics might appear. The anomalous coupling parameters can not take arbitrary values. They are restricted by S-matrix unitarity. Assuming that the independent coupling parameters are $\kappa = \kappa_\gamma = \kappa_Z$ and $\lambda = \lambda_\gamma = \lambda_Z$, the tree-level unitarity is satisfied if [16, 24]

$$\Lambda_{FF} \leq \left(\frac{6.88}{(\kappa - 1)^2 + 2\lambda^2 + 2\tilde{\lambda}^2} \right)^{1/4} \text{TeV}.$$

Therefore the experimental limits obtained must be compared with the bounds derived from S-matrix unitarity. Experiments constrain the WWV couplings non-trivially only if the experimental limits are more stringent than the unitarity bounds, for a

given value of Λ_{FF}. The effect of anomalous values of λ_V on the reduced amplitudes $\mathcal{A}(\pm, \pm)$ is enhanced by $\hat{s}$, as seen in the above equation. Terms containing $\Delta\kappa_V$[5] mainly contribute to $\mathcal{A}(\pm, 0)$ and grow only with $\sqrt{\hat{s}}$. In $q\bar{q} \to W^+W^-$, on the other hand, the $\Delta\kappa_V$ term mostly contributes to the (0,0) amplitude and is enhanced by a factor of $\hat{s}$. The best limits on $\Delta\kappa_V$ are therefore expected from $q\bar{q} \to W^+W^-$.

For large values of diboson invariant mass $\sqrt{\hat{s}}$, the non-standard contributions to the helicity amplitudes would dominate. Since anomalous couplings only contribute via $s-$channel W, Z or photon exchange, their effects are concentrated in the region of small vector boson rapidities, and the transverse momentum distribution of the vector boson is particularly sensitive to non-standard WWV couplings. This is demonstrated in Fig. 2.2, which shows the p_T^W distribution in $p\bar{p} \to WW \to e\nu jj$, at the Tevatron for the SM and various anomalous WWV couplings. A dipole form factor with scale $\Lambda_{FF} = 1.5$ TeV is used and the couplings for $WW\gamma$ and WWZ are assumed to be equal. These theoretical calculations for the Standard Model and anomalous couplings processes were carried out using a Monte Carlo generator program by D. Zeppenfeld [25]. This generator will be described in Chapter 4.

Information on anomalous WWV couplings can be obtained by comparing the shape of the measured and predicted p_T distribution of the W boson, provided that the signal is not overwhelmed by background. Even if the background is much larger than the SM prediction, limits on anomalous couplings can still be extracted using a phase space region where the effects of non-standard three vector couplings dominate.

---

[5] $\Delta\kappa$ is defined as $\Delta\kappa \equiv (\kappa - 1)$.
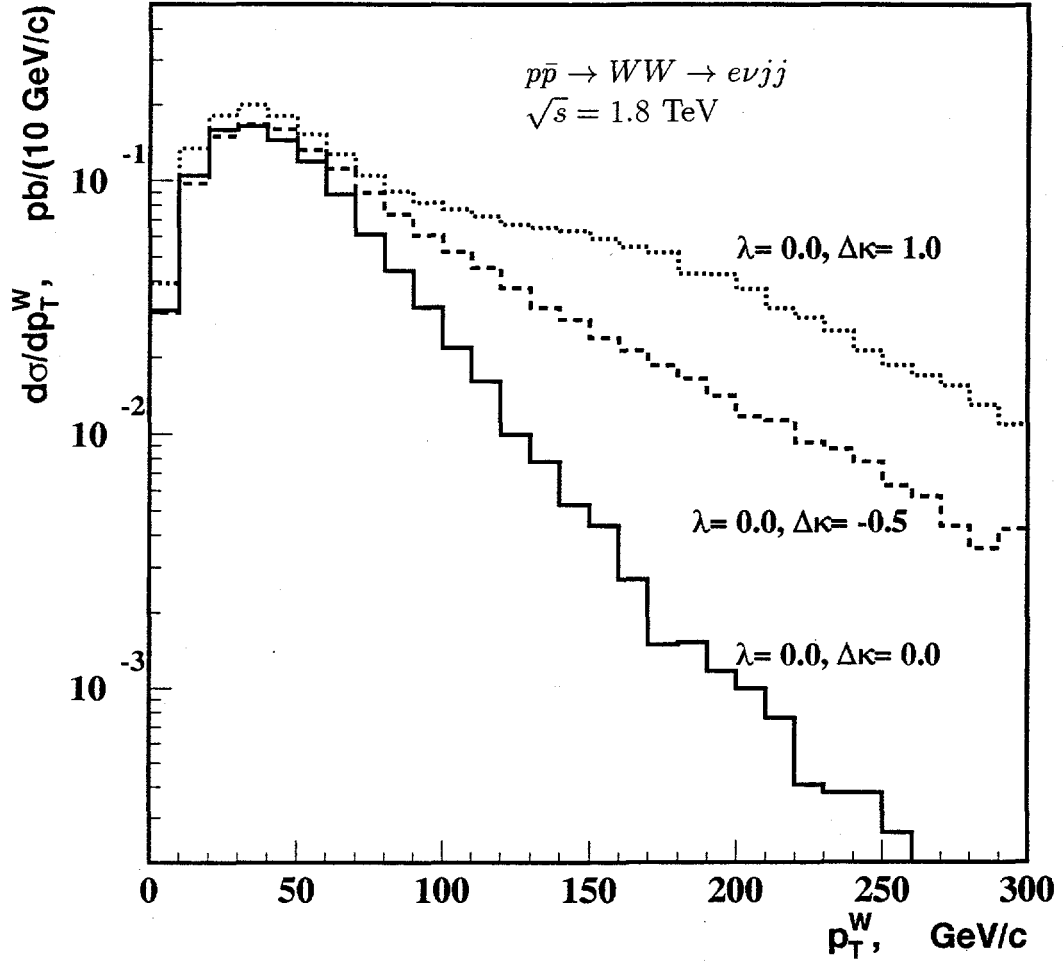
Figure 2.2: The p_T^W spectrum of generated $p\bar{p} \rightarrow WW \rightarrow e\nu jj$ reaction with SM couplings and two example of anomalous couplings.

To observe gauge boson pair production signals, the decay products of W's and/or Z's have to be observed above possible backgrounds. While leptonic decays of both vector bosons provide a virtually background-free signal, branching ratios for this double-leptonic mode are tiny, even when adding up electron and muon decay channels. On the other extreme, purely hadronic decays of both vector bosons are

expected to be unobservable in view of the large four-jet QCD background. One is led,
to look for dilepton plus dijet, or the semihadronic decay signature for vector-boson
pairs. Decay modes where one of the bosons decay hadronically have significantly
larger branching ratios than all leptonic decays:

$$Br(WW \to e\nu_e e\nu_e, \mu\nu_\mu\mu\nu_\mu) = 2.4\%, \qquad Br(WW \to e\nu_e\mu\nu_\mu) = 2.4\%.$$

$$Br(WZ \to l_1\nu_1 l_2^+ l_2^-) = 1.5\%, \qquad l_{1,2} = e, \mu,$$

$$Br(WW \to l\nu jj) = 29\%, \qquad l = e, \mu,$$

$$Br(WZ \to l\nu jj) = 15\%, \qquad Br(WZ \to jj l^+ l^-) = 4.5\%.$$

The production cross section times branching ratio for WW final states is
approximately eight times larger than for WZ final states. The major background to
$WW/WZ \to l\nu jj$ events is from the W+jets production which has a much higher
cross section than the WW process. In Ref. [14], this background was estimated from
data and a fit to data was performed using the estimated background spectrum. On
the other hand, a kinematical cut was applied to data to eliminate this background
in Ref. [10]. In $p\bar{p} \to W^+W^-$ production, $t\bar{t} \to bW^+\bar{b}W^-$ production represents an
additional non-negligible background.

Besides the study of trilinear couplings, the search for WW production is
important since the SM predicts the production of the Higgs boson and its decays to
WW through a quark triangle diagram. An upper limit on the WW cross section
is a direct limit on SM Higgs production. As there are some additional interesting
processes which produce the same final state, for example gluon-gluon fusion to WW

through a quark box diagram and weak boson fusion, an upper limit on the WW cross section is also a direct limit on these processes. For determination of the boson self couplings, these processes are background channels. However, the predicted cross section of these processes are so small [26, 27] that they are ignored for the results shown in this thesis.

2.3.2   Experimental Studies of the WWV Vertex

The WWV vertex has already been studied by several experiments. The $WW\gamma$ vertex has been studied using $W\gamma$ production events in $p\bar{p}$ collisions at UA2 [28], CDF [8], and DØ [13, 15] experiments. The UA2 results are based on data taken during the 1988-1990 CERN $p\bar{p}$ collider run at $\sqrt{s} = 630$ GeV with an integrated luminosity of 13 pb^{-1}. CDF and DØ have studied the $W\gamma$ production using 1992-1993 and 1993-1995 Fermilab $p\bar{p}$ collider run at $\sqrt{s} = 1.8$ TeV. The WWZ vertex together with the $WW\gamma$ vertex has also been studied by the CDF [10] and DØ collaborations using W pair production in the dilepton decay modes [11] and WW/WZ production in the semihadronic modes [14] with the data from the 1992-1993 run. Table 2.1 summarizes the current results on anomalous WWV couplings at hadron colliders.

In the present thesis we will describe a search for $p\bar{p} \to WWX$ followed by $W \to e\nu$ and $W \to jj$, and $p\bar{p} \to WZX$ followed by $W \to e\nu$ and $Z \to jj$, where j represents a jet. Due to the limited jet energy resolution, $W \to jj$ decay can not be differentiated from $Z \to jj$ decay. The experiment was carried out with the DØ

experiment	channel	limit
UA2 (13 pb^{-1})	$p\bar{p} \to W^{\pm} \to l^{\pm}\nu\gamma$	$-3.5 < \Delta\kappa_{\gamma} < 5.9$
1988-1990	$l = e, \mu$	$-3.6 < \lambda_{\gamma} < 3.5$
CDF (67 pb^{-1})	$p\bar{p} \to W^{\pm} \to l^{\pm}\nu\gamma$	$-1.8 < \Delta\kappa_{\gamma} < 2.0$
1992-1995	$l = e, \mu$	$-0.7 < \lambda_{\gamma} < 0.6$
DØ (13.8 pb^{-1})	$p\bar{p} \to W^{\pm} \to l^{\pm}\nu\gamma$	$-1.6 < \Delta\kappa_{\gamma} < 1.8$
1992-1993	$l = e, \mu$	$-0.6 < \lambda_{\gamma} < 0.6$
DØ (89.1 pb^{-1})	$p\bar{p} \to W^{\pm} \to l^{\pm}\nu\gamma$	$-0.98 < \Delta\kappa_{\gamma} < 1.01$
1992-1995	$l = e, \mu$	$-0.33 < \lambda_{\gamma} < 0.31$
DØ (14 pb^{-1})	$p\bar{p} \to W^{+}W^{-} \to l_1\nu_1 l_2\nu_2$	$-2.6 < \Delta\kappa_{V} < 2.8$
1992-1993	$l_{1,2} = e, \mu$, "$\gamma = Z$", $\Lambda_{FF} = 0.9$ TeV	$-2.1 < \lambda_{V} < 2.1$
CDF (110 pb^{-1})	$p\bar{p} \to W^{+}W^{-}, W^{\pm}Z \to l^{\pm}\nu jj, l^{+}l^{-}jj$	$-0.49 < \Delta\kappa_{V} < 0.54$
1992-1995	$l = e, \mu$, "$\gamma = Z$", $\Lambda_{FF} = 2.0$ TeV	$-0.35 < \lambda_{V} < 0.32$
DØ (13.7 pb^{-1})	$p\bar{p} \to W^{+}W^{-}, W^{\pm}Z \to e\nu jj$	$-0.9 < \Delta\kappa_{V} < 1.1$
1992-1993	"$\gamma = Z$"	$-0.6 < \lambda_{V} < 0.7$

Table 2.1: The 95% CL limits on anomalous WWV, $V = \gamma, Z$ couplings from UA2, CDF and DØ. Only one of the independent couplings is allowed to deviate from the SM at a time. $\Lambda_{FF} = 1.5$ TeV is assumed except where indicated.

detector at Fermilab. From the number of observed signal events and background estimates the 95% confidence level upper limit on the W pair production cross section is obtained. Limits on anomalous coupling parameters, λ and $\Delta\kappa$, are also set.

Chapter 3

Experimental Apparatus

The Tevatron accelerator at the Fermi National Accelerator Laboratory (FERMILAB) currently provides the highest center-of-mass energy in the world, 1.8 TeV. There the DØ detector, designed to make world-class measurements, works when the Tevatron operates in colliding beam mode. In this chapter, the major detector subsystems are briefly described. Emphasis is placed on those aspects which are most relevant for this study. A full description of the various pieces could be found in the references.

3.1 The Tevatron

The particle accelerator complex at FERMILAB, the highest energy accelerator in the world, is called Tevatron. The machine, which has the capability to accelerate protons to nearly one trillion electron volts or 1 TeV, is composed of superconducting

magnets, and it is also used to accelerate a beam of antiprotons that circulate in an opposite direction than the beam of protons in the same vacuum chamber.

The Tevatron can be operated in one of two major modes. In fixed-target mode, it is filled with protons which are accelerated and then extracted and directed through a series of underground tunnels to the fixed target experimental areas where the protons strike a variety of stationary targets. This cycle repeats with a frequency of about once per minute. In collider mode, the Tevatron is filled with six bunches of protons and six bunches of antiprotons, traveling in opposite directions. The beams are ramped together to the energy of 900 GeV per beam and they are then crossed at the BØ (CDF) and DØ luminous regions. The beams are typically kept colliding for about 12-18 hours. The Tevatron is the last stage of the system of seven components. Fig. 3.1 shows these components. Since the processes for accelerator operation are quite complicated we will describe them very briefly. For more details consult reference [29].

The acceleration process starts in a electrostatic Cockroft-Walton accelerator, where hydrogen ions consisting of one proton and two electrons are formed and accelerated to 750 KeV. The ions are bunched and transported to the start of a 150 meters long linear accelerator, the Linac, where they are accelerated to 400 MeV, using oscillating electric fields. After emerging from the Linac, the two electrons are stripped off the negative hydrogen ions by passing them through a carbon foil, leaving only bare protons. These protons are then injected into a 151 meters diameter synchrotron [1],

---

[1] A synchrotron uses magnets to bend electrically charged particles in a circular path so they
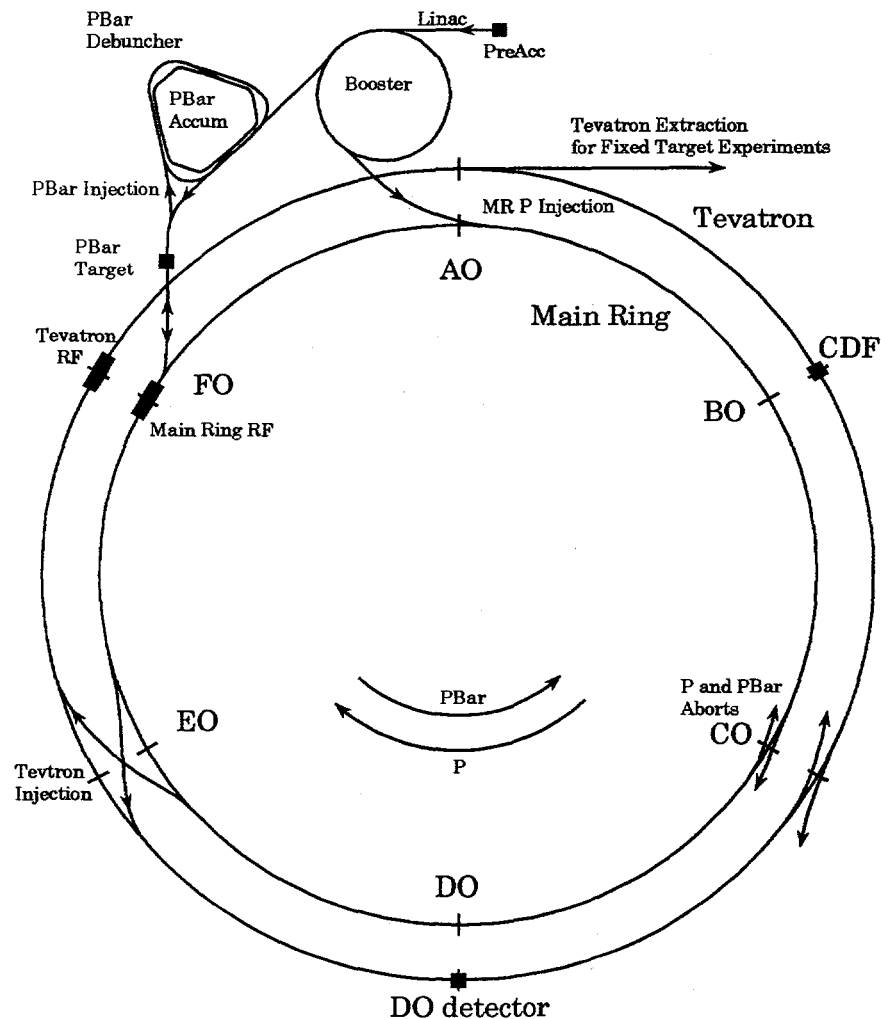
Figure 3.1: Schematic diagram of the Fermilab accelerator complex.

known as the Booster. The Booster accelerates the protons to an energy of 8 GeV. The protons are injected into a 1000 meters radius synchrotron, called the Main Ring, where they are accelerated to 150 GeV using conventional magnets and are finally injected into the Tevatron. The protons can be accelerated up to 900 GeV, using superconducting magnets. When the system operates in collider mode, the protons in

repeatedly experience accelerating electric fields.

the Main Ring are used to initiate production of antiprotons. Every 2.4 seconds 120 GeV protons are extracted from the Main Ring onto a nickel target, which produces a spray of nuclear debris including some antiprotons. These are finally focused by lithium lenses into the Debuncher ring, a triangularly shaped machine that equalizes the energies of the antiprotons and collects them into a beam by a process called stochastic cooling. The monoenergetic antiprotons are then injected into the Accumulator ring before the next batch of antiprotons arrives from the nickel target. The antiprotons are merged into a single beam, cooled further, and stored over a period of hours or even days. The Debuncher and Accumulator rings operate at 8 GeV, the same energy as the Booster accelerator. When a large number of antiprotons (typically 10^{11} to 10^{12}) have been stored, they are extracted into 6 different bunches and transferred back into the Main Ring, accelerated to 150 GeV, and injected into the Tevatron. The antiprotons circulate counterclockwise in the Main Ring and the Tevatron, whereas the protons circulate clockwise. Table 3.1 lists several Tevatron parameters.

The performance of the collider is described by the term called luminosity ($\mathcal{L}$) which is the interaction rate per unit cross section ($cm^{-2}s^{-1}$). Luminosity is proportional to the frequency of bunch collisions, the numbers of protons in one bunch and the number of antiprotons in the bunch which hits the protons. It is also inversely proportional to the cross sectional area of the two colliding bunches. The luminosity at the Tevatron during the period of collider operation was typically $10^{31} cm^{-2}s^{-1}$. The number of events of a specific type after a period of time of operation is found

Accelerator radius	1000 m
Maximum beam energy	900 GeV
Injection energy	150 GeV
Peak luminosity	$\sim 10 \times 10^{30}$ cm^{-2}s^{-1}
Number of bunches	6 p, 6 $\bar{p}$
Intensity per bunch	$\sim 100 \times 10^{9}$ p, 50×10^{9} $\bar{p}$
Bunch length	50 cm
Transverse beam radius	43 μm
RF frequency	53 MHz
$\bar{p}$ stacking rate	$\sim 3.5 \times 10^{10}$/hour
Beam crossing frequency	290 kHz
Period between crossings	3.5 μs

Table 3.1: Tevatron parameters.

by multiplying the cross section by the luminosity integrated over time. The total integrated luminosity, typically expressed in barns (where 1 barn = 10^{-24} cm^2), for the run 1993-1995 at DØ was over 100 pb^{-1} from which around 90 pb^{-1} of data was stored to tape.

3.2 The DØ Detector

The DØ detector [30], located at the DØ interaction region on the Tevatron ring, is a general purpose detector designed to study proton-antiproton collisions at $\sqrt{s}$ = 1.8 TeV. With emphasis on precision measurements of leptons, photons, and jets, DØ is optimized for the study of physics at high mass and large transverse processes momentum such as W and Z boson production, search for the top quark, various studies of perturbative QCD, the production of b-quark hadrons, and searches

for new phenomena beyond the Standard Model.
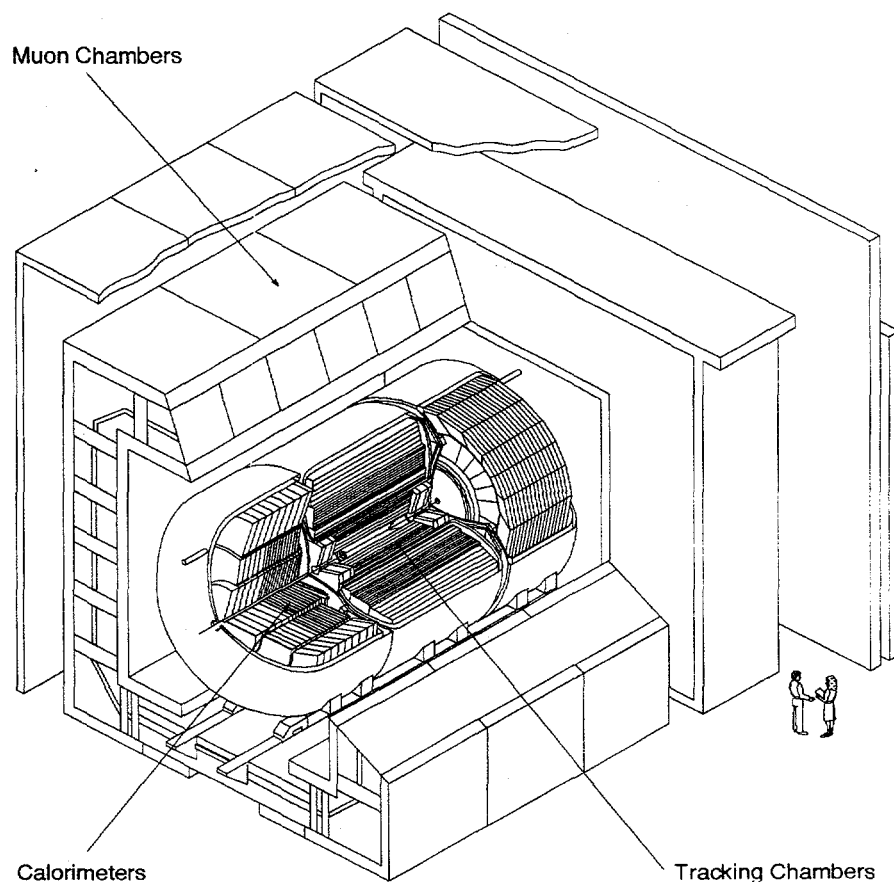
Figure 3.2: Cutaway view of the DØ detector

The DØ detector, illustrated in Fig. 3.2, consists of a set of tracking detectors surrounding the beam pipe. DØ does not have a central magnetic field to bend trajectories of charged particles. The absence of a central magnetic field implies the need of very good calorimeters. DØ uses liquid argon sampling calorimeters made mostly from depleted uranium. The calorimeter is thick enough to stop all the

particles except muons and neutrinos. To identify muons, an additional set of tracking chambers is installed surrounding the calorimeter. To provide a measurement of the muon momentum, magnetized iron toroids are placed between the first two muon tracking layers.

The full detector is about 13 m high × 11 m wide × 17 m long with a total weight of about 5500 tons. The Tevatron beam pipe passes through the center of the detector, while the Main Ring passes through the upper portion of the calorimeter, 89.2 inches above the Tevatron beam pipe. The global coordinate system used in DØ is a right-handed coordinate system, with the z-axis aligned along the beam in the direction of the protons (southward), and y-axis pointing up. Therefore the polar angle $\theta = 0$ along the proton direction, and the azimuthal angle $\phi = 0$ along the eastward direction. Instead of θ the pseudorapidity, $\eta = -\ln(\tan(\theta/2))$, is often used. This quantity approximates the true rapidity $y = 1/2\ln((E+p_z)/(E-p_z))$, when the rest mass is much smaller than the energy.

3.2.1 Tracking Detectors

The DØ tracking and transition radiation detectors comprise the central detector (CD). The main goal of the CD is to measure with high precision the position of charged particle tracks and determine the z position of the interaction vertex. This information can be used to decide if an electromagnetic cluster in the calorimeter was caused by an electron or by a γ/π^0. Additional information such as the number of
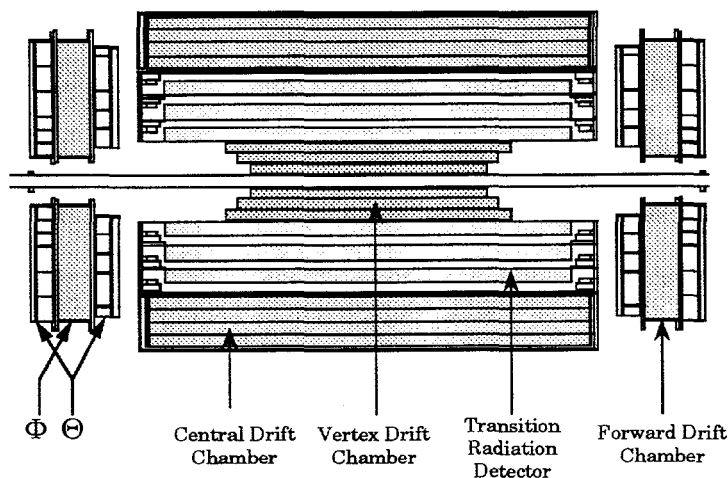
Figure 3.3: DØ tracking and transition radiation detectors.

tracks and the ionizing energy along the track (dE/dx) can be used to determine if the track was actually caused by several closely spaced charged particles, such as a photon/pion conversion. Fig. 3.3 shows the CD system, which consists of four separate subsystems: the vertex drift chamber (VTX), the transition radiation detector (TRD), the central drift chamber (CDC), and two forward drift chambers (FDC). The full set of CD detectors fits within the inner cylindrical aperture of the calorimeters in a volume of radius $r = 78$ cm and length $l = 270$ cm. The system provides charged particle tracking over the region $|\eta| < 3.2$ in pseudorapidity. It measures the trajectories of charged particles with a resolution of 2.5 mrad in ϕ and 28 mrad in θ. From these measurements the position of the interaction vertex along the beam direction (z) can be determined with a resolution of 6 mm.

The VTX is the innermost tracking chamber in the DØ detector. It is comprised of three mechanically independent concentric layers of cells parallel to the beam

pipe, from 3.7 cm to 16.2 cm. The innermost layer has sixteen cells while the outer two layers have thirty-two cells each. The VTX was originally designed to provide precise position determination of primary and secondary vertices, from heavy (charm, bottom) quark decays, and a large η coverage. It also serves as a complementary tool for track reconstruction, dE/dx measurement, and vertex identification.

The TRD occupies the space between the VTX and the CDC; it extends from 17.5 cm to 49 cm. It was designed to provide independent electron identification in addition to that given by the calorimeters. The TRD consists of three separate units, each containing a radiator (393 foils of 18 μm thick polypropylene in a volume filled with nitrogen gas) and an X-ray detection chamber filled with Xe gas. For this configuration, the X-rays have an energy distribution which peaks at 8 keV and is mainly contained below 30 keV. The TRD information is not used in this analysis.

The CDC is a cylindrical shell of length 184 cm with radii between 49.5 and 74.5 cm, which provides coverage for $|\eta| < 1.2$. It is made up of four concentric rings of 32 azimuthal cells per ring. Each cell contains seven sense wires (staggered by 200 μm relative to each other to help resolve left-right ambiguities), and two delay lines. The CDC is operated with $Ar(92.5\%)CH_4(4\%)CO_2(3\%)$ gas and small amount of $H_2O(0.5\%)$. The $r\phi$ position of a hit is determined via the drift time and the wire hit. The z position of a hit is measured using inductive delay lines embedded in the module walls in the sense wire plane. When an avalanche occurs near an outer sense wire, a pulse is induced in the nearby delay line. By comparing the arrival times of

the pulse at both ends, the z position can be determined.
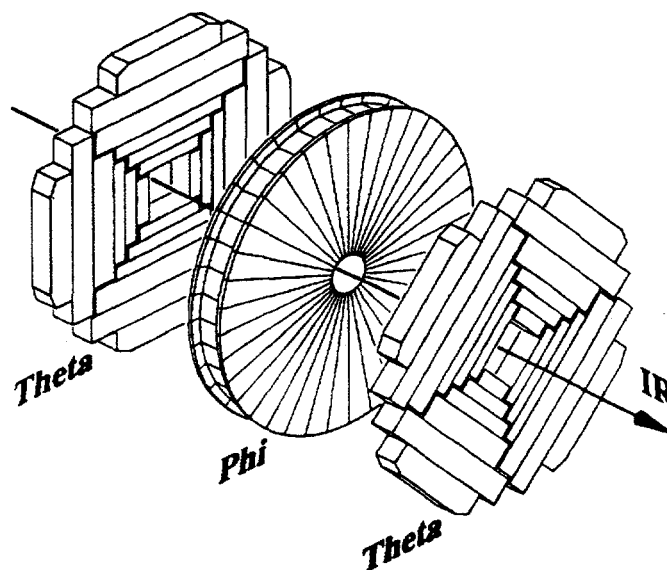
Figure 3.4: View of the FDC Θ and Φ modules.

The FDC (Fig. 3.4) consists of two sets of drift chambers located at the end of the CDC. They perform the same function as the CDC for $1.4 < |\eta| < 3.1$. Each FDC package consists of three separate chambers: the Φ module whose sense wires are radial and measure the ϕ coordinate, sandwiched between a pair of Θ modules whose sense wires measure the θ coordinate. The Φ layer is divided into 36 azimuthal drift cells, each containing sixteen radial sense wires arranged in a plane containing the beam line. The two Θ cells consists of four separate quadrant modules, each of which is composed of six rectangular-shaped cells at increasing radii. Each cell contains eight sense wires oriented in a plane parallel to the z-axis and normal to the radial direction. Each Θ cell also contains a delay line of the same type as in the CDC

to measure the position along the length of the cell. There are no delay lines in the Φ chamber. The two Θ chambers are rotated relative to each other by an angle of $\pi/4$. The FDC chambers are operated with the same gas as the CDC, with similar performance.

3.2.2 Calorimeters

The calorimeter design is crucial for the optimization of the D$\emptyset$ detector. Since there is no central magnetic field, the calorimeter must provide the energy measurement for most types of particles. In addition, the calorimeter plays an important role in the identification of electrons, photons, jets and muons, and in establishing the transverse energy balance in the event. For the present analysis the calorimeter is the most important part of the detector, since electron and jets are identified from the patterns of energy deposited in the calorimeter.

The D$\emptyset$ calorimeter is a sampling calorimeter, with liquid argon (LAr) as the ionization medium. The primary absorber material is depleted uranium, with copper and stainless steel in the outer regions. Since uranium is very dense, the calorimeter is relatively compact. The calorimeter is divided into three modules contained in separate cryostats: the Central Calorimeter (CC), the North End Calorimeter (ECN), and the South End Calorimeter (ECS). The CC covers roughly $|\Delta\eta| \leq 1$ and the EC Modules extends the coverage out to $|\eta| \approx 4$. In each module the absorber plates cause the incident particles to shower, and the resulting particles deposit ionization in the
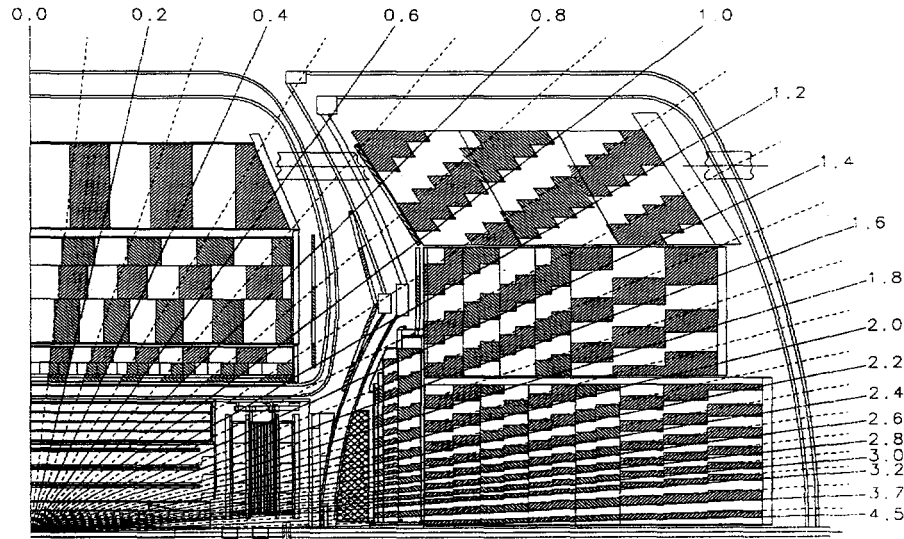
Figure 3.5: Side view of one quadrant of the calorimeter and central detector showing the transverse and longitudinal segmentation pattern. The shading pattern indicates the distinct cells for signal readout. The rays indicate the pseudorapidity intervals seen from the center of the detector.

LAr gaps. A voltage gradient causes the resulting charges to drift and induce a signal on pickup boards located in the gaps. Signals from several boards are then ganged to form readout cells. These cells are arranged with a pseudo-projective geometry, as shown in Fig. 3.5. In this arrangement the center of each cell points toward the center of the interaction region, but the cell boundaries are aligned perpendicular to the absorber plates.

Taking advantage of the difference between the electromagnetic and strong interactions in matter, the DØ calorimeter modules are further subdivided by depth into three distinct types of modules: an electromagnetic section (EM) with relatively thin uranium absorber plates, a fine-hadronic section (FH) with thicker uranium plates

and a coarse-hadronic section (CH) with thick copper or stainless steel plates. There are four separate depth layers for the EM modules in CC and EC. The first two layers are typically 2 radiation lengths (X_0) thick and are included to help measure the longitudinal shower development near the beginning of showers where photons and π^0s differ statistically. The third layer spans the region of maximum EM shower energy deposits and the fourth completes the EM coverage of approximately $20X_0$. The fine hadronic modules are typically segmented into three or four layers. Typical transverse sizes of towers in both EM and hadronic modules are $\Delta\eta = 0.1$ and $\Delta\phi = 2\pi/64 \approx 0.1$. The third section of EM modules is twice as finely segmented in both η and ϕ to allow more precise location of EM shower centroids.

Section	EM	FH	CH
Pseudorapidity Coverage (η)	±1.2	±1.0	±0.6
Absorber Material	U	U (1.7% Nb)	Cu
Absorber Thickness (mm)	3.0	6.0	46.5
Number of Readout Layers	4	3	1
Depth per Readout Layer	2, 2, 7, 10 X_0 (0.76 λ_a)	1.3, 1.0, 0.9 λ_a	3.2 λ_a
Total Radiation Lengths (X_0)	21	96	33
Total Nuc. Abs. Lengths (λ_a)	0.76	3.2	3.2
Sampling Fraction	11.79%	6.79%	1.45%
Segmentation ($\Delta\eta \times \Delta\phi$)	0.1×0.1 (Layers 1,2,4) 0.05×0.05 (Layer 3)	0.1×0.1	0.1×0.1
Total Number of Channels	10,368	3000	1224

Table 3.2: Parameters of the DØ Central Calorimeter

The CC has a length of 2.6 m covering the pseudorapidity region $|\eta| < 1.2$ and consist of three concentric cylindrical rings. There are 32 EM modules in the inner

ring, 16 fine hadronic (FH) modules in the surrounding ring, and 16 coarse hadronic

(CH) modules in the outer ring. The EM, FH and CH module boundaries are rotated

so that no projective ray encounters more than one intermodule gap. Table 3.2 lists

details of the CC.

Section	ECEM	IFH	ICH
Pseudorapidity Range (η)	$\pm$ (1.3–4.1)	$\pm$ (1.6–4.5)	$\pm$ (2.0–4.5)
Absorber Material	U	U (1.7% Nb)	Steel
Absorber Thickness (mm)	4.0	6.0	46.5
Number of Readout Layers	4	4	1
Total Depth	20 X_0 (0.95 λ_a)	4.4 λ_a	4.1 λ_a
Sampling Fraction	11.9%	5.7%	1.5%
Total Number of Channels	7488	4288	928
Section	**MFH**	**MCH**	**OH**
Pseudorapidity Range (η)	$\pm$ (1.0–1.7)	$\pm$ (1.3–1.9)	$\pm$ (0.7–1.4)
Absorber Material	U (1.7% Nb)	Steel	Steel
Absorber Thickness (mm)	6.0	46.5	46.5
Number of Readout Layers	4	1	3
Total Depth	3.6 λ_a	4.4 λ_a	4.4 λ_a
Sampling Fraction	6.7%	1.6%	1.6%
Total Number of Channels	1856	384	960

Table 3.3: Parameters of the DØ Endcap Calorimeters

The two mirror-image end calorimeters (ECN and ECS) cover the region 1.1 <

$|\eta|$ < 4.5. Each contains four module types. To avoid the dead spaces in a multi-

module design, there is just one EM module and one inner hadronic (IH) module.

Outside the EM and IH, there are concentric rings of 16 middle and outer (MH and

OH) modules. The azimuthal boundaries of the MH and OH modules are offset to

prevent cracks through which particles could penetrate the calorimeter. This makes the DØ detector almost completely hermetic and allows for a very accurate measurement of missing transverse energy. Due to the third layer segmentation in the ECEM module, 0.1×0.1 for $|\eta| > 2.5$, the electron and photon candidates are restricted to $1.5 < |\eta| < 2.5$ in the EC. In the region $|\eta| > 3.2$ the transverse cell segmentation increases to a maximum of 0.4×0.4. Table 3.3 shows additional details of the EC modules.

Between the CC and EC regions ($0.8 \leq |\eta| \leq 1.4$), there is a large amount of uninstrumented material in the form of cryostat walls, stiffening rings and module endplates, as indicated in Fig. 3.5. To correct for energy deposited in the uninstrumented walls there are two scintillation counter arrays, of size 0.1×0.1, called intercryostat detectors (ICD). In addition, separate single-cell structures called massless gaps (MG) are mounted on the surfaces of the CCFH, ECMH, and ECOH modules. Together, the ICD and MG provide a good approximation to the standard DØ sampling of EM showers.

It should also be pointed out that the Main Ring beam pipe passes through the CH section of the CC. Beam losses from the Main Ring will show up in the detector and must be rejected. To avoid those losses, DØ either can stop recording data during periods of Main Ring activity near the detector or flag the events when they are passed through the trigger system. Of the 2.4 seconds of the Tevatron cycle, approximately 21% is deadtime due to the activity of the Main Ring.

3.2.3 Muon Detectors

The DØ muon detector, located outside the calorimeter, is divided in two subsystems: the Wide Angle Muon Spectrometer (WAMUS) and the Small Angle Muon Spectrometer (SAMUS). The WAMUS detector has an angular coverage of $10° \leq \theta \leq 170°$, and SAMUS has an angular coverage of $3.7° \leq \theta \leq 10°$. The purpose of this system is the identification of muons produced in $\bar{p}$-p collisions and the determination of their trajectories and momenta. Since the calorimeter is thick enough to absorb the debris from electromagnetic and hadronic showers, muons can be identified with higher purity than electrons. The muon system is not used in this analysis and is not discussed here. The interested reader should consult Ref. [30] for details.

3.3 Multilevel Trigger, and Data Acquisition

Because it is not possible to record and process all data generated after every beam crossing at the Tevatron, DØ has to use a mechanism to filter a small number of interesting events for permanent storage and later studies. This process, called triggering, is carried out by a multilayer hierarchical trigger with increasingly complex tests applied to the data at each succeeding stage, reducing the sample of events.

The first stage, called level-0 (L0) [31], consists of two scintillator arrays mounted on the front surfaces of the EC cryostats perpendicular to the beam direction. Each

array partially covers a region in pseudorapidity of $1.9 < |\eta| < 4.3$, with nearly complete coverage over $2.2 < |\eta| < 3.9$. The L0 system is used to detect the occurrence of an inelastic $p\bar{p}$ collision and serves as the luminosity monitor for the experiment. In addition, it provides fast information on the z-coordinate of the primary collision vertex, by measuring the difference in arrival time from particles hitting both L0 arrays, for use in early trigger decisions. A slower, more accurate position of the interaction and indication of the occurrence of multiple interactions[2] are available for subsequent trigger decisions. The luminosity is estimated by measuring the rate of inelastic $\bar{p}p$ interactions, which has a known value of 48.2 mb [32] at $\sqrt{s} = 1.8$ TeV (derived by averaging measurements from E710 and CDF). A systematic normalization uncertainty of 5.4% [33] is assigned to the luminosity determination, based on differences between Monte Carlo calculations and zero-bias data. The L0 trigger is $\approx 99\%$ efficient for non-diffractive inelastic collisions. The rate of data from L0 is on the order of 150 kHz.

The next stage corresponds to the so-called Level 1 trigger (L1) [34]. It is the heart of the trigger system and is responsible for combining the result of individual L1 components into a set of global decisions that commands the readout of the digitization crates, and interacts with the next stage, the level 2 trigger (L2); see Fig. 3.6. Most of these components; such as the L1 calorimeter triggers and the muon triggers operate

---

[2] Multiple $p\bar{p}$ interactions in a beam crossing can be identified by looking at the time distribution of the hits. If the hits came from one interaction, they would arrive at nearly the same time; otherwise the hits from different interactions will in general arrive at different times. Obviously, interactions that occur at the same time and are together in z will not be resolved and the L0 detector will tag them as one interaction.
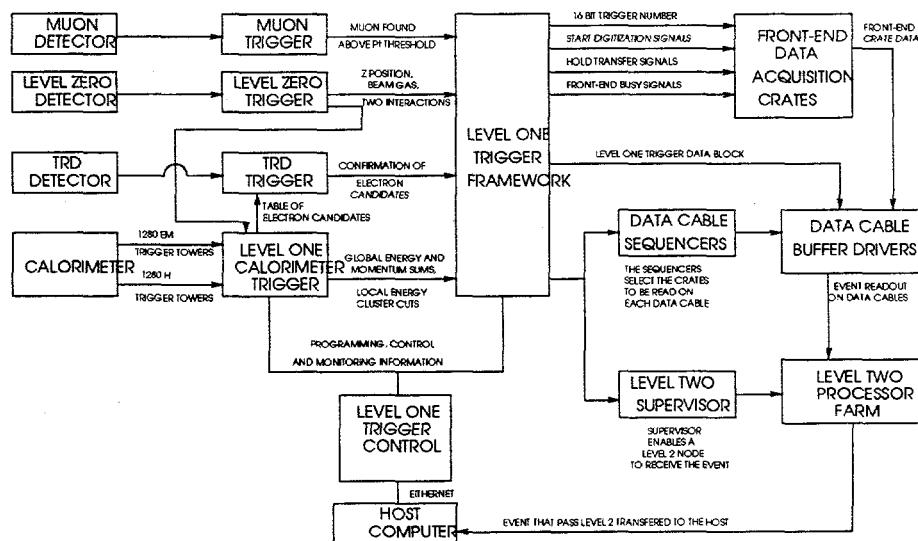
Figure 3.6: A diagram of the DØ trigger indicating individual trigger components and their interconnections.

within the $3.5\mu s$ interval between beam crossings so that no events go by unexamined. However, some other components, like the TRD trigger and some components of the muon trigger, called the level 1.5 trigger (L1.5), may require more time. The goal of the L1 trigger is to reduce the event rate from the beam crossing frequency to a rate of 100 - 200 Hz. The primary input for the L1 trigger consists of 256 trigger terms and each of which is a single bit indicating that some specific requirement is met. These 256 terms are reduced to a set of 32 L1 trigger bits, specific triggers, by a two-dimensional AND-OR network. An event is said to pass L1 if at least one of these 32 bits is set. The L1 trigger also uses information about the Main Ring activity, which can be used to veto certain events either as part of the L1 system or as part of an offline analysis. In order to prevent the saturation of the trigger system, due to the large cross sections of some process like QCD multijets, the L1 trigger can be

prescaled. This means that the trigger will actually cause readout and further trigger processing only once every N times that the trigger term conditions are satisfied.

The L1 calorimeter trigger covers up to $|\eta| < 4.0$ in trigger towers of 0.2×0.2 in $\eta - \phi$ space. These towers are subdivided longitudinally into electromagnetic and hadronic trigger towers. The output of the calorimeter L1 is the transverse energy deposited in these towers. While the output of the L1 muon trigger is the number of muon candidates and their p_T.

When events fire the L1 trigger the event data are passed on the standard DØ data acquisition pathways to a farm of 50 parallel microprocessors which serve as event builders as well as the L2 trigger system. The function of the L2 system is to collect the digitized data from all relevant detector elements and trigger blocks for events that successfully pass the Level 1 triggers and to apply sophisticated algorithms to reduce the event rate to about 2 Hz before passing events on to the host computer for event monitoring and recording. All the data for a specific event is sent over parallel paths to memory modules in a specific, selected node (one of 50). The event data are collected and formatted in final form in the node, and the L2 filter algorithms are executed.

The L2 filtering process in each node is built around a series of filter tools. Each tool has a specific function related to identification of a type of particle or event characteristic. There are tools to recognize jets, muons, calorimeter EM clusters, track association with calorimeter clusters, $\sum E_T$, and missing E_T. Other tools recognize

specific noise or background conditions. The tools are associated in particular com-
binations and orders into scripts; a specific script is associated with each of the 32
L1 triggers bits. The script can spawn several L2 filters from a given L1 trigger bit;
therefore, there are 128 L2 filters bits available. If all the L2 requirements (for at least
one of these 128 filters) are satisfied, the event is said to pass L2 and it is temporarily
stored on disk before being transferred to an 8 mm magnetic tape.

Once an event is passed by a L2 node, it is transmitted to the host cluster,
where it is received by the data logger, a program running on one of the host com-
puters. This program and others associated with it are responsible for receiving raw
data from the L2 system and copying it to magnetic tape, while performing all ne-
cessary bookkeeping tasks (e.g. time stamps, run number and output event number,
etc.). Data may also be sent to the online DAQ pool for online monitoring.

3.3.1   Electron Trigger

To trigger on electrons, L1 requires the transverse energy in the EM section
of a trigger tower to be above programmed thresholds. The L2 electron algorithm
uses the full segmentation of the EM calorimeter to identify electron showers. Using
the trigger towers that were above threshold at level 1 as seeds, the algorithms form
clusters which include all cells in the four EM layers and the first FH layer in a
region of $\Delta\eta \times \Delta\phi = 0.3 \times 0.3$, centered around the tower with the highest E_T. The
longitudinal and transverse energy profile of the cluster must satisfy the requirements:

- The fraction of the cluster energy in the EM section must be above an energy and detector position dependent threshold.

- The transverse shape classification is based on the energy deposition pattern in the third layer. The difference of the energy depositions in two regions, covering $\Delta\eta \times \Delta\phi = 0.25 \times 0.25$ and 0.15×0.15 and centered on the cell with the highest E_T, must be within a window, which depends on the total cluster energy.

3.3.2 Jet Trigger

Roughly speaking, one calls a jet the products of fragmentation or hadronization of quarks or gluons (partons) into collimated colorless, hadron collections. DØ triggers thes objects based on the following steps: The L1 jet triggers require the sum of the transverse energy in the EM and FH sections of a trigger tower to be above programmed thresholds. The L2 jet algorithm begins with an E_T ordered list of towers that were above thresholds at L1. At L2 a jet is formed by placing a cone of given radius R, where $R = \sqrt{\Delta\eta^2 + \Delta\phi^2}$, around the seed tower from L1. If another seed tower lies within the jet cone then it is passed over and not allowed to seed a new jet. The summed E_T in all of the towers included in the jet cone defines the jet E_T. If any two jets overlap, then the towers in the overlap region are added into the jet candidate which was formed first. To filter events, cuts on several quantities can be imposed. These are the minimum transverse energy of a jet, the minimum transverse size of a jet, the minimum number of jets, and the fiducial cuts on the pseudorapidity

of the jets.

3.3.3   Missing Transverse Energy Trigger

Many rare and interesting physics processes involve production of weakly in-
teracting particles such as neutrinos. These particles can not be detected with con-
ventional collider detector, like DØ. However, conservation of momentum from the
initial to final state implies that momenta of such particles can be inferred from the
vector sum of the momenta of the particles which are detected. Since much of the
energy flow near the beamline is largely undetected, this method can only be used
in the transverse plane to the beam. Therefore if a neutral stable weakly interacting
particle were produced with high p_T, the negative vector resultant of the detected
particles would have the same momentum vector. This quantity is referred as Missing
E_T and denoted by $\rlap{/}{E}_T$; it is used as an indicator of the presence of weakly interacting
particles. At L2, $\rlap{/}{E}_T$ is computed using the vector sum of all calorimeter and ICD
cells with respect to the z position of the interaction vertex, which is determined from
the timing of the hits in the L0 counters. At L2, we can require that the $\rlap{/}{E}_T$ in the
event be above a threshold.

3.3.4   Triggers for W Boson Studies

Since the present analysis is from a subset of the $W \to e\nu$ data the same trigger
selection as the standard $W \to e\nu$ analysis is used.

In order to allow diffractive studies of W boson production, the trigger conditions for the W boson did not require that Level 0 be fired. Level 1 required an electromagnetic trigger tower to have at least 10 GeV of transverse energy, E_T. The name of this trigger was EM1_1_HIGH. Level 1.5 then required the Level 1 object to pass an E_T cut of 15 GeV. This level also checked whether the electromagnetic fraction (EM energy over total energy of the tower) is greater than 85%. The Level 2 filter conditions are varied according to the purpose of the filter. The filter for the W signal had several requirements on the electron to enhance the probability that the electron was from a $W \to e\nu$. The electron candidate had to have at least 20 GeV in E_T, it had to pass shower shape cuts based on test beam data; it had to be isolated from other objects in the calorimeter; and it must have had at least 15 GeV of missing E_T. The name of this filter was EM1_EISTRKCC_MS.

There were also several L2 filters that allowed to do background studies. Two of these are EM1_ELE_MON and ELE_1_MON. They required an electron candidate with at least 20 GeV and 16 GeV, respectively, and a shower shape cut, but no isolation cut. These filters used the same L1 and L1.5 conditions as the W signal filter.

The efficiency and turn-on curves of the L2 filter for the W signal are described in Ref. [35]. The efficiency was found to be $(99 \pm 1)\%$. The integrated luminosity is estimated to be 76.5 ± 4.2 pb^{-1} [36], with the requirement of no Main Ring activity imposed off-line.

Chapter 4

Event Reconstruction and Particle Identification

After an event is selected by the trigger system, the information available from the detector is in the form of digitized pulse heights, widths, and times. To turn this information into recognizable objects like electrons and jets, DØ uses an event reconstruction program called DØRECO [37]. Since the amount of time available to select events at L2 is small (typically 200 ms), the DØRECO program is executed off-line. The DØRECO program consists of several packages: the CD track reconstruction, the vertex reconstruction, the calorimeter energy cluster reconstruction, and the muon track reconstruction. The electrons, muons, neutrinos and jets are identified using the reconstructed informations from these packages. This chapter describes some of the reconstruction packages and the particle identification criteria used in this analysis.

During reconstruction, groups of data describing an object or characteristics of a given event (called ZEBRA banks [38]) are created, linked, and either passed on or dropped. Selected events are written out to two types of files: the standard output (STA) and the data summary tapes (DST). The STA files contain the raw data plus the complete results of the reconstruction (the file size is on average about 600 kbytes/event). The DST files are compressed version of the STA files containing only processed information (the file size is approximately 20 kbytes/event). Since the amount of data available in the 1993-1995 run is very large (45M events) a third file format was introduced to further reduce the data volume. This new type of file, called microDST (μDST) [39], contains the minimum amount of information needed to perform analyses (the file size is around 5 kbytes/event). All events are placed on disks in μDST format, and these files are further filtered by analysis groups to make the size of data set manageable. In the last few months this data is also available in Column Wise Ntuples [38, 40]. This analysis will use the last format [41].

4.1 Vertex Reconstruction

The determination of the primary vertex interaction point is mainly done using information of the CDC. Prior to the execution of DØRECO, the CD-EXAMINE program [37] determined the transverse (x, y) position of the interaction point; DØRECO determined the z-coordinate of the interaction point. All CDC tracks were extrapolated to the z axis and the intersection in z for each track was stored. A cluster finding

algorithm was used to determine how many clusters were associated with any z position. For each cluster the mean value for the intersection in z of all the tracks in this cluster was taken to be the z position of the interaction point. A constrained fit was made to determine a more precise z vertex measurement. For a multiple interaction event, DØRECO provided up to three possible vertex candidates, and the vertex with most tracks was designated as the primary vertex. For the data used in this analysis the distribution of vertices was centered at $z = 0.3$ cm with an rms deviation of 29.1 cm.

4.2   Electrons

Electrons are identified by the detection of an electromagnetic shower in the calorimeter with an associated track in the central tracking system.

4.2.1   Electron Reconstruction

To reconstruct electrons (and photons) DØRECO uses a nearest neighbor algorithm [30, 34, 37]. It starts by grouping EM towers. The energy of the four EM layers and the first FH layers are summed in this purpose. The towers are then ordered in transverse energy. Next the highest energy towers are picked and clusters are created adding physically adjacent towers with $E > 50$ MeV to the cluster. They have to pass the following criteria to be considered as an electron/photon candidate: 90% of the cluster energy must be in the EM section of the calorimeter, and at least 40% of

the energy must be contained in a single tower. To distinguish electrons from photons DØRECO searches for a track in the central detector that points from the interaction vertex to the EM cluster within a window of $\Delta\eta = \pm0.1$, $\Delta\phi = \pm0.1$. If one or more tracks are found, the object is classified as an electron. Otherwise, it is classified as a photon.

4.2.2 Electron Identification

The development of EM and hadronic showers is quite different and the shower shape information can be used to differentiate between electrons (photons) and hadrons. The following variables are used to select the electrons [42, 43]:

Electromagnetic Energy Fraction. This quantity, referred to as *emf*, is based on the observation that electrons deposit almost all their energy in the EM section of the calorimeter (around 90 %), while hadrons are typically much more penetrating (only 10% of their energy is deposited in the EM section of the calorimeter) and is defined as the ratio of EM energy to the total shower energy . Therefore a cut at the high emf value provides a powerful discrimination against charged hadrons. All the electrons in this analysis are required to have at least 95% of their total energy in the EM calorimeter. This requirement is about 99% efficient (studies of these efficiencies are described below).

Covariance Matrix χ^2 [44]. The shower shape may be characterized by the fraction of the cluster energy deposited in each layer of the calorimeter. These fractions are also

dependent on the incident electron energy. However, these fractions are correlated, i.e., a shower which deposits a large fraction of its energy in the first layer will then deposit a small fraction in the subsequent layers and vice versa. To obtain the best discrimination against hadrons, we use the energy observed in a given layer and its correlations with the energy deposited in the other layers. This is done using a covariance matrix technique. Suppose one has a set of N observations of events of a given type, where each observation consists of M variables: $\mathbf{x}^n = (x_1^n, \ldots, x_M^n)$. One can form the covariance matrix from the outer products

$$M_{ij} = \frac{1}{N} \sum_{i=1}^{N} (x_i^n - \overline{x}_i)(x_j^n - \overline{x}_j),$$

where $\overline{x}_i$ is the mean of the ith observable. The H-matrix is defined by the inverse of this covariance matrix $H = M^{-1}$. We determine whether a shower k is electromagnetic by computing the covariance parameter

$$\chi^2 = \sum_{i,j=1} (x_i^k - \overline{x}_i) H_{ij} (x_j^k - \overline{x}_j).$$

The observables are the fractional energies in layers 1, 2, 4 of the EM calorimeter, and the fractional energy in each cell of 6 × 6 array of cells in layer 3 centered on the most energetic tower in the EM cluster. To parametrize the energy and the impact parameter dependence of the matrix, we also include the logarithm of the shower energy and the position of the event vertex along the beam as two independent parameters. The matrix H is thus 41-dimensional. Since H is a symmetric matrix, it can be diagonalized using a unitary matrix U so that $H' = UHU^T$ is diagonal.

Then $\chi^2 = yH'y^T$ and the components of the vector y are uncorrelated variables. For each of the 37 detector towers at different values of $|\eta|$, we build a matrix from Monte Carlo (MC) electrons. By comparing the shower shape of these electrons with shower shapes from electron beam tests we have verified excellent agreement of the MC with the calorimeter response. Slight differences in shower shapes between Monte Carlo and data can cause larger contributions to χ^2, if the eigenvalues of the matrices are unusually large. To prevent any component from dominating the value of the covariance variable χ^2, we limit the magnitude of the diagonal elements of H' to a maximum value, which optimizes the electron finding efficiency and rejection power as illustrated in Fig. 4.1. In this analysis we require that the χ^2 is less than 100 for CC electron candidates and less than 200 for EC electrons. This requirement is about 95% efficient.
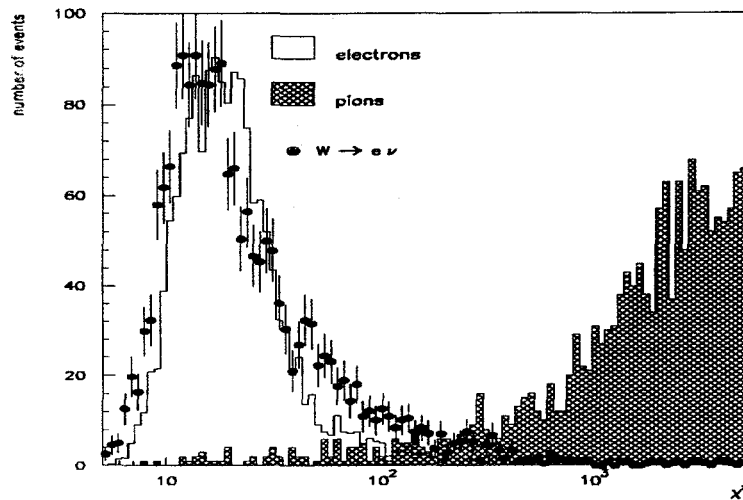
Figure 4.1: χ^2 distribution for test beam electrons (unshaded), test beam pions (shaded), and electrons from W's (dots).

Isolation. The decay electron from a W should not be close to any other object in the event. This is quantified by the isolation fraction. Let $E(0.4)$ be the energy deposited in all electron cells in the cone $\mathcal{R} < 0.4$ around the electron direction and $EM(0.2)$ the energy deposited in the EM calorimeter in the cone $\mathcal{R} < 0.2$. The isolation variable is then defined as the ratio

$$\mathcal{I} = \frac{E(0.4) - EM(0.2)}{EM(0.2)}.$$

A requirement of $\mathcal{I} < 0.1$ is approximately 97% efficient.

Track match significance. An important source of background for electrons is photons from the decay of π^0 or η mesons. Such photons do not leave tracks in the central detector, but might appear to do so if a charged particle is nearby. This background can be reduced by demanding a good spatial match between calorimeter energy cluster and nearby tracks . The significance S of the mismatch between these quantities is given by

$$S = \sqrt{\left(\frac{\Delta\phi}{\delta_{\Delta\phi}}\right)^2 + \left(\frac{\Delta z}{\delta_{\Delta z}}\right)^2},$$

where $\Delta\phi$ is the azimuthal mismatch, Δz the mismatch along the beam direction, and δ_x is the resolution of the observable x. This form is appropriate for the central calorimeter. In the end region, r replaces z. Requiring S $< 5\sigma$ is 95(78)% efficient for CC(EC) electrons.

Track-in-road. All the electrons were required to have a reconstructed track somewhere in the tracking road from the cluster to the vertex to enter the $W \to e\nu$ sample.

This implicit requirement has an efficiency associated with it which is referred to as the track-in-road efficiency. For this analysis it was found to be 83(86)% for CC(EC) electrons.

For this analysis we combined these quantities to form the electron identification criteria. A summary of the cuts used and their efficiencies is listed in table 7.1.

4.2.3 Electromagnetic Energy Corrections

The energy scale of the calorimeters was originally set using test beam calibration data. However, due to differences in conditions between the test beam setup and the DØ installation, this calibration is slightly low. Therefore we have to correct this effect on the data before starting any analysis.

The EM energy scale for the DØ calorimeter was determined by comparing the masses measured in $\pi^0 \to \gamma\gamma$ [45], $J/\psi \to ee$ [46], and $Z \to ee$ decays to their known values [6]. If the electron energy measured in the calorimeter and the true energy are related by $E_{meas} = \alpha E_{true} + \delta$, the measured and true mass values are, to first order, related by $m_{meas} = \alpha m_{true} + \delta f$. The variable f depends on the decay topology and is given by $f = 2(E_1 - E_2)\sin^2(\gamma/2)/m_{meas}$, where γ is the opening angle between the two decay products and E_1 and E_2 are their measured energies. When the three independent constraints are combined the values of α and δ are set [47].

4.2.4   Energy Resolution

The energy resolution of electrons and photons is expressed by the empirical relation

$$\left(\frac{\sigma}{E}\right)^2 = C^2 + \frac{S^2}{E} + \frac{N^2}{E^2}$$

where E is the energy of the incident electron, C is a constant term due to calibration errors, S is the sampling fluctuation of the liquid argon calorimeter and N correspond to the noise term. The sampling term is obtained from test beam results, and the constant and noise terms are tuned to match the resoultion of observed $Z \rightarrow ee$ events and simulated ones. Table 4.1 lists these parameters [48].

Quantity	CC	EC
C	0.017	0.0094
S	0.140	0.1570
N	0.490	1.1400

Table 4.1: Energy resolution parameters for electrons and photons.

4.3   Jets

Several different definitions of a jet are used in D0, depending on the nature of physics analysis. Here, we describe the fixed cone algorithm, the primary choice of DØ, since it is easily applicable to theoretical calculations.

4.3.1 Jet Reconstruction

The algorithm uses a fixed-cone radius $\mathcal{R} = \sqrt{\Delta\eta^2 + \Delta\phi^2}$. Four cone sizes were used, $\mathcal{R} = 0.3$, 0.5, 0.7, and 1.0. The algorithm begins with the highest E_T tower and preclusters are formed of contiguous cells out to a radius of about $\mathcal{R} = 0.3$. The preclusters are used to reduce the number of cells considered as possible starting points for jet formation, and to reduce the processing time. Only towers with $E_T > 1$ GeV are included in preclusters. These preclusters become the starting point for jet finding and the precluster center is used as the initial cone center. A new E_T weighted center is then formed using E_T of all towers within a radius $\mathcal{R}$ of the center, and the process is repeated until the jet is stable. A jet must have $E_T > 8$ GeV. If two jets share energy, they are combined or split, based on the fraction of energy shared relative to the E_T of the lower E_T jet. If the shared fraction exceeds 50%, the jets are combined.

The kinematic quantities defining a jet are:

$$E_i = \textstyle\sum_{towers\ k} E_i^k,$$

$$E_T = \textstyle\sum_{towers\ k} E_T^k,$$

$$\phi = \arctan(E_y/E_x),$$

$$\theta = \arccos(E_z/\sqrt{E_x^2 + E_y^2 + E_z^2}),$$

where i represents the four components of the four-momentum vector. Note that E_T is the scalar sum of the transverse energies of the individual towers, and not the magnitude of their vector sum.

4.3.2   Jet Identification

A fixed cone algorithm with a radius of 0.5 in eta-phi space is used in this analysis. The $\mathcal{R} = 0.3$ cone algorithm is more efficient [14] compared to wider cone sizes which cause undesired jet merging for high p_T W or Z. However, due to the relatively large uncertainties in the jet energy measurement of the 0.3 cone algorithm as a result of losses of energy which are caused by the energy flowing out of the cone or undesirable splitting of jets, we choose to use the 0.5 cone algorithm as the primary algorithm for our studies.

In order to remove fake jets produced by cosmic rays, calorimeter noise, and protons from the Main Ring entering the detector, DØ has developed a set of quality cuts based on the characteristics of real jets. These quality cuts are applied to every jet and are based on a detailed study [49] of fourteen thousand Monte Carlo events (which tell us how to keep good jets), noise data taken with no colliding beam (which tell us how to reject fake jets), and colliding beam data sets. The variables used are:

Electromagnetic Energy Fraction (emf). As for electrons, this quantity is defined as the fraction of energy deposited in the electromagnetic section of the calorimeter. This cut was designed to remove electrons and/or photons (which typically have a high EM fraction) and fake jets caused by the Main Ring or by hot cells (which do not have energy depositions in the EM section, resulting in a low EM fraction) from the jet sample (which in general leave energy in both electromagnetic and hadronic sections of the calorimeter since they are a mixture of hadrons and photons from π^0

decays). All jets with EM fraction within (0.05,0.95) were defined as good jets.

Hot Cell Energy Fraction (hcf). This quantity is defined as the ratio of the energy of the second highest E_T cell over the energy of the highest E_T cell within a jet. The cut was designed to removed calorimeter noise. Hot cells appear when a cell sparks; it will be misinterpreted as energy deposition since it occurs at random and without affecting neighboring cells. In this case the HC fraction will be small since the energy in a jet is expected to be spread over a number of cells. If most of its energy is concentrated in only one cell, it is very likely to be a false jet reconstructed from electronic noise. For good jets hcf was found to be grater than 0.1.

Coarse Hadronic Energy Fraction (chf). This quantity is defined as the fraction of jet energy deposited in the coarse hadronic section of the calorimeter. The cut was designed to remove activity caused by the Main Ring. The Main Ring at DØ goes through the CH modules and any energy deposition related to it will concentrate in this section of the calorimeter. It has been shown that fake jets due to Main Ring activity tend to have more than 40% of their energy in the CH region [50], while real jets have less than 10% of their energy in this section of the calorimeter. Therefore good jets were required to have a chf less than 0.4.

4.3.3   Hadronic Energy Corrections

Since the measured jet energy usually is not equal to the energy of the original parton which formed the jet, corrections are needed to avoid systemtic biases.

There are several effects which contribute to the jet energy response. such as. non-uniformities in the calorimeter, non-linearities in the calorimeter response to hadrons, noise due to the radioactivity of uranium, and energy from the products of soft interactions of spectator partons within the proton and the antiproton (underlying event). To estimate these effects DØ uses the method called Missing E_T Project Fraction (MPF).

The method starts by looking for events with an isolated EM cluster due to a photon or a jet which fragmented mostly into neutral mesons, a hadronic jet lying opposite in ϕ, and no other objects in the event. The EM cluster energy is corrected using the electromagnetic energy corrections described above. There should be no energetic neutrinos in these events so that any missing transverse energy ($\not{E}_T$) remaining in the event can be attributed to a mismeasurement of the hadronic jet. Projecting the $\not{E}_T$ along the jet axis, the needed corrections for the jet can be derived. This is averaged over similar jets in the sample to produce a correction which is a function of jet E_T, η, and electromagnetic content. Other effects such as out-of-cone showering (due to wide showers), the underlying event, and noise effects were determined in separate studies using Monte Carlo and minimum bias[1] samples. All these corrections as well as the electromagnetic energy corrections are included in the software package called CAFIX [51]. In this analysis we used the version 5.0 of the package.

In addtion to these corrections, the effect of shower leaking out of the jet cone

---

[1] minimum bias data is referred to events in which the only requirement was that the L0 trigger fired.

due to QCD out of cone radiation must be taken into account. It is not a part of CAFIX

corrections. The correction basically is an offset in energy of the jet as a function of

its energy and η [52].

η Region	Noise Term (N)	Sampling Term (S)	Constant Term (C)
$|\eta| < 0.5$	7.07±0.09	0.81±0.02	0.00±0.01
$0.5 < |\eta| < 1.0$	6.92±0.09	0.91±0.02	0.00±0.01
$1.0 < |\eta| < 1.5$	0.00±1.40	1.45±0.02	0.05±0.01
$1.5 < |\eta| < 2.0$	8.15±0.21	0.48±0.07	0.00±0.01
$2.0 < |\eta| < 3.0$	3.15±2.50	1.64±0.13	0.01±0.58

Table 4.2: Jet energy resolution parameters for each of the calorimeter regions.

4.3.4 Energy Resolution

The jet energy resolution has been studied in [43] using dijet momentum bal-

ance. The empirical formula for the jet E_T resolution is

$$\left(\frac{\sigma}{E_T}\right)^2 = C^2 + \frac{S^2}{E_T} + \frac{N^2}{E_T^2}$$

where C is the error term from the calibration, S represents the shower fluctuations

in the sampling gaps, and N denotes the contribution due to noise and the underlying

event. Table 4.2 shows the resolution parameters in each of the calorimeter η regions.

4.4 Neutrinos: Missing Transverse Energy

As we mentioned above, neutrinos cannot be detected with the DØ detector, but they are inferred from the missing E_T. In this analysis we have assumed the $\not{E}_T$ in each event corresponds to an associated neutrino in the $W \rightarrow e\nu$ decay.

The calculation of $\not{E}_T$ is based on energy deposition in the individual cells of the calorimeters. Each cell in the calorimeter is given a four-vector, with an energy equal to the measured energy in the cell, a direction pointing from the interaction vertex to the center of the cell, and a mass of zero. The vector $\vec{\not{E}}_T$ is defined by

$$\not{E}_{Tx} = -\sum_i E_i sin(\theta_i)cos(\phi_i) - \sum_j \Delta E_x^j,$$

$$\not{E}_{Ty} = -\sum_i E_i sin(\theta_i)sin(\phi_i) - \sum_j \Delta E_y^j,$$

where the first sum is over all cells in the calorimeter, ICD, and MG. The second sum is over the corrections in E_T applied to all electrons and jets in the event. The missing transverse energy, $\not{E}_T$, is the magnitude of this vector, which we call calorimeter missing-E_T. This definition does not include the muons, which (for high-p_T muons) only deposit a small portion of their energy in the calorimeter. Therefore the total missing E_T is then the calorimeter missing E_T with the transverse momenta of good muon tracks subtracted. Since in this analysis we do not use muons, we will refer to the calorimeter-$\not{E}_T$ as the $\not{E}_T$.

Also useful is $\phi_{\not{E}_T}$, the azimuthal direction of the $\not{E}_T$ vector, defined by $\phi_{\not{E}_T} = $ arctan$(\not{E}_y/\not{E}_x)$. The scalar $E_T(E_T^{scalar})$ defined as the scalar sum over all calorimeter cells of transverse energy: $E_T^{scalar} = \sum_{cells\ i} E_{Ti}$.

4.4.1 $\displaystyle{\not\mathrel{E}_T}$ Resolution

An ideal hermetic detector would measure the magnitude of $\not\mathrel{E}_T$ vector as zero for events with no real source of missing E_T. However, detector noise and energy resolution in the measurement of jets, photons, electrons and muons will contribute to some amount of missing E_T. In addition, dead regions or non-uniformity of response in the detector will also result in missing E_T. Therefore it is important to measure this contribution of $\not\mathrel{E}_T$ to gauge the sensitivity of the detector to real missing E_T. The missing E_T resolution is parameterized as [43]

$$\sigma(\not\mathrel{E}_T) = 1.08 \text{ GeV} + 0.019 \cdot \left(\sum E_T \right)$$

which was obtained using minimum bias data. The $\sum E_T$ is used for this parameterization since one would expect that the greater the total amount of transverse energy in the event, the larger the possible mismeasurement of the balance.

4.5 Monte Carlo Event Simulation

Due to the complexity of high energy experiments sometimes it is difficult to interpret the results. A detailed computer simulation of such experiments is an important element of the data analysis. The simulation is usually performed with a Monte Carlo technique. The Monte Carlo technique consists of two steps: the simulation of the physics process, called event generation, and the simulation of the response

of the detector, called detector simulation. The event generation step uses theoretical calculations and models based on experimental measurements. For the detector simulation, depending on the characteristics of the study, we can choose between two methods: a complete full simulation or a parametric simulation. The full simulation is usually resource-consuming, extremely slow, and sometimes impractical process. Besides, it relies very much on a precise description of different detector components, which is not always in agreement with the measurement based on real data. On the other hand the parametric simulation is very practical, very fast, and is based on real data wherever possible. In this analysis, depending on the purposes of the study, we have used five different event generators: ISAJET [53], PYTHIA [54], HERWIG [55], VECBOS [56] (followed by a full detector simulation based on the programs DØGEANT [57] and DØRECO, the reconstruction program), and the Zeppendfeld-Baur anomalous couplings event generator [25] (followed by a fast detector simulation [58]).

DØGEANT is the DØ implementation of the CERN detector simulation program GEANT [59]. This package provides tools for specifying volumes containing particular materials and the framework for transporting particles through these volumes with appropriate physical scattering and interaction processes included. Processes such as δ-ray production, multiple Coulomb scattering, full showering by electromagnetic and hadronic particles, particle decays, and bremsstrahlung by electrons and muons are accurately simulated. Each particle is tracked down to the preset minimum energies that depend on the processes. In DØGEANT, the minimum energies are set to 10 keV

for all processes. The step size of the track depends on the medium and is chosen so that the simulated distributions reproduce the measured ones. The geometry and materials of the DØ detector are the inputs for GEANT.

ISAJET, PYTHIA, and HERWIG generators are based on perturbative QCD calculations and phenomelogical models for parton fragmentation. The main difference between them is at the hadronization process where they use different fragmentation models, but this difference is usually small. ISAJET and PYTHIA have the ability to generate SM $W\gamma$ and WZ. In our analysis we used primarily ISAJET and PYTHIA to check possible inaccuracies in ISAJET. HERWIG, combined with VECBOS, was used to simulate $W \geq 2j$ production.

VECBOS is a more specialized event generator. We used it to generate QCD $W \geq 2j$ process which are the major source of background for $WW, WZ \rightarrow e\nu jj$ production. VECBOS generates leading order parton level processes using the tree-level exact matrix elements for $(W$ or $Z) + $ n jets processes for $1 \leq n \leq 4$. VECBOS calculations are based solely on the formalism of perturbative QCD (PQCD). Therefore some restrictions were applied in order to validate these assumptions and its accuracy:

$E_T > 15$ GeV for all final partons,

$\Delta\mathcal{R} > 0.5$ for every pair of jets,

CTEQ3M set of structure functions [60],

$\langle Q^2 \rangle = \langle p_T(j) \rangle^2$ for dynamical scale.

The events generated by VECBOS represent final state partons. In order to simulate the detector response to these events the particle fragmentation of these final states had to be simulated and the effects of the underlying ("spectator") processes included. The results from VECBOS were therefore run through a modified version of HERWIG to hadronize the partons. As VECBOS carries no information about the flavor of the final partons the assumption was made that they are all gluons. Because VECBOS calculations are only based on tree-level diagrams (leading order) there can be significant errors in the prediction of cross sections as the number of jets increases. We therefore normalized the VECBOS calculations by using data.

Since none of the event generators mentioned above has the ability to include WW and WZ production with non-Standard Model couplings, an event generator developed by D. Zeppenfeld was used. This generator calculated $p\bar{p}{\rightarrow}W^+W^-$ and $p\bar{p}{\rightarrow}WZ$ processes at 1.8 TeV with subsequent decay of a W to $e\nu$ or jj and a Z to jets. The $WW\gamma$ and WWZ couplings could be set to any value. The processes were generated to leading order. A "$K\ factor$" of $K = 1 + \frac{8}{9}\pi\alpha_s = 1.34$ was included for higher order QCD corrections. We have used the Duke-Owens set I [61] structure functions which give the lowest cross section at NNL according to Ohnemus, et al. [16]. Therefore the results based on anomalous couplings are conservative and any uncertainty in the cross section due to the choice of the structure functions should not be included. We adopted a fast detector parametrization to include the effects of the detector since the number of events required for this study is considerably large.

The fast detector simulation is based on package described in Ref. [58]. The program first modifies the kinematics to reflect the higher-order processes by including a hadronic recoil. This hadronic recoil is determined from data using the p_T^Z spectrum. The gauge boson pair system is boosted opposite the hadronic recoil and now is ready to include any other effects. For each event the z vertex position is smeared with a Gaussian distribution centered at $z \approx 0$ with a width of approximately 30 cm determined from data. All the object energies, depending on the type of particle, are smeared to correctly model detector response. The resolution functions used are those given above. The missing transverse energy is determined by the energy imbalance and the energy of the underlying event calculated from real minimum bias data. The four vectors are converted into detector geometry variables (ϕ, η) to determine if a given event passes the kinematic or fiducial requirements. All the efficiencies measured from data are taken into account. An extra efficiency due to the reconstruction of $W \rightarrow jj$ process is taken into account as described in the next chapter. For both kinematic acceptance and particle id efficiencies, a random number is used to determine if a given event passes the requirements. With this parametric Monte Carlo a large number of Monte Carlo experiments can be performed in a relatively short time. We use this method to study the gauge boson pair production processes with anomalous couplings.

Chapter 5

Event Selection

This analysis studies the $p\overline{p}{\rightarrow}WWX$ and $p\overline{p}{\rightarrow}WZX$ processes followed by $W{\rightarrow}e\nu$ and $W/Z{\rightarrow}jj$, where j represents a jet. Because of the limited jet energy resolution, we cannot distinguish WZ events from WW events. The candidate events are selected based on particle identification and kinematical criteria. Particle identification criteria are used to reduce the instrumental background, while kinematical criteria are used to control the background processes which have the same final states as our signal. In this chapter we describe the selection procedure.

5.1 Data Quality

The analysis uses data taken during the 1993-1995 Tevatron Collider Run (called Run 1b). The data sample comes from the WZ group single-electron stream. which contains all events which pass a L2 WZ EM filter, that requires at least one

electromagnetic object with $E_T >$ 15 GeV and missing $E_T >$ 15 GeV [62]. The L2 filter used was EM1_EISTRKCC_MS described above. The integrated luminosity of the data sample is estimated to be 76.5±4.5 pb^{-1}. All the events with Main Ring activity were eliminated as well as any other events for which the data acquisition system had problems (called bad runs). We have also required that the L0 counters fired, since the initial trigger conditions for the W boson did not require this.

The energy of all the objects has been corrected using the standard DØ energy correction package CAFIX v5.0, described above. In addition the energy of the jets was corrected to take into account radiation outside the jet cone. In the selection we have also imposed the requirement of at least one reconstructed interaction vertex, and we are not requiring any cut on the multiple-interaction flag [63].

Beyond the standard electron and jet identification we introduce additional fiducial requirements:

$|\eta_{\text{det}}(e)| < 1.1$ and away from the module cracks ($\Delta\phi > 0.01$) for CC electrons,

$1.5 < |\eta_{\text{det}}(e)| < 2.5$ for EC electrons, and

$|\eta_{\text{det}}(j)| < 2.5$ for jets,

where η_{det} is the pseudorapidity of the objects calculated with the vertex $z = 0$. We use η_{det} because the acceptance is determined by the geometry of the detector. We will reject events with electrons in the region $1.1 < |\eta_{\text{det}}| < 1.5$ because in this region there is essentially no EM calorimetry. The pseudorapidity upper limit for electrons and

jets is motivated by the large amount of material in front of the CDC. The tracking efficiency in this region is poor an triggering is difficult due to the high probability for photons/π^0's to convert . We also require that the electrons in the CC must be away from module cracks to avoid shower leakage.

5.2 Kinematic Criteria

The $WW, WZ \rightarrow e\nu jj$ candidates were selected by searching for events containing a $W \rightarrow e\nu$ and at least two jets consistent with $W \rightarrow jj$ or $Z \rightarrow jj$. The $W \rightarrow e\nu$ decay was identified by requiring that there be one and only one electron in the event with an E_T^e above 25 GeV and at least 25 GeV of missing transverse energy, forming a transverse mass $M_T > 40$ GeV/c^2. The transverse mass is defined as

$$M_T = \sqrt{2 \cdot E_T^e \cdot \not{E}_T \cdot (1 - cos(\phi_e - \phi_\nu))}.$$

The cut on the electron E_T at 25 GeV is to avoid the leading edge of the trigger turn-on curve which has a hardware threshold of 20 GeV. The requirement of only one electron is to reduce any contamination from Z's. The cuts on $\not{E}_T$ and M_T help us to reduce the background contributions, mainly from 'fake-electrons'. The E_T^e and $\not{E}_T$ distributions are shown in figures 5.1 and 5.2 respectively for data, SM predictions and major backgrounds[1]. The Transverse mass M_T is shown in Fig. 5.3. The $\not{E}_T$ for the candidates clearly shows two peaks, one around 35 GeV, corresponding to the

---

[1]From here on, we will refer QCD $W \geq 2$ jets events (which is estimated in chapter 6 using MC samples) and QCD multijets events (which is also estimated in chapter 6, but using a data control sample) as major backgrounds. Sometimes we also call the latter "QCD-fakes".
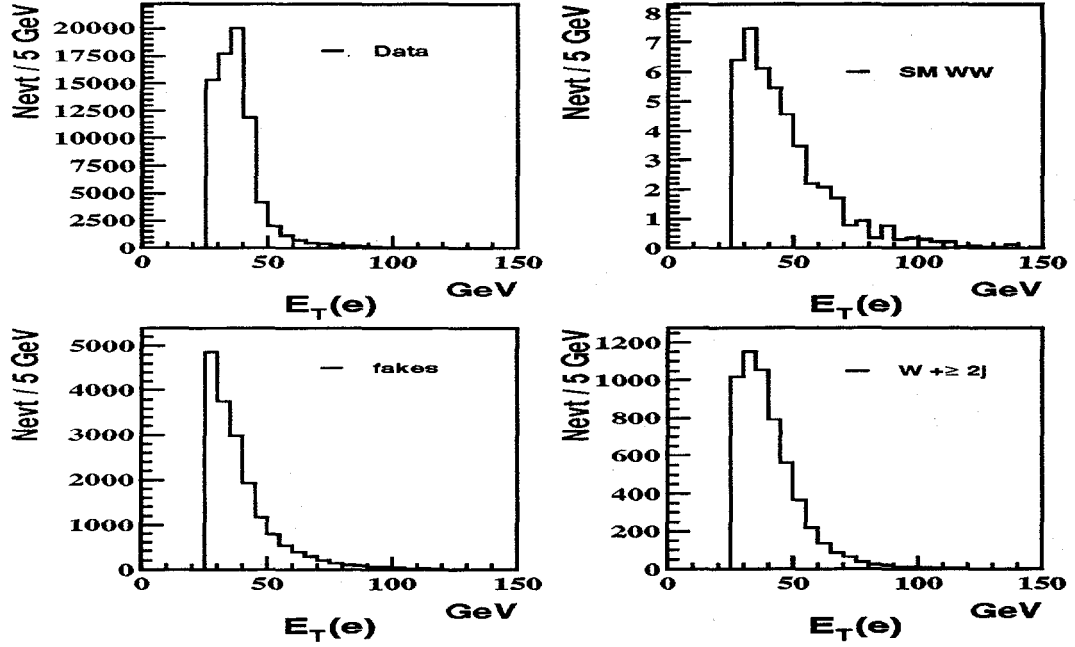
Figure 5.1: E_T^e distributions for data, SM $WW \rightarrow e\nu jj$ production and the major backgrounds.

missing E_T peak of $W \geq 2$ jets events, as seen in the lower right plot in Fig. 5.3 and another near 15 GeV, corresponding to the apparent peak of the fake background due to the trigger turn-on, as seen in the lower left plot in Fig. 5.3. The relative heights of these two peaks reflect the relative amount of background in the candidate sample.

The $W/Z \rightarrow jj$ decay was identified by requiring at least two jets with $E_T^j >$ 20 GeV and a dijet invariant mass satisfying $50 < M_{jj} < 110$ GeV/c^2. The dijet invariant mass (M_{jj}) is calculated by the formula

$$M_{jj} = \sqrt{2 \cdot E_T^{j1} \cdot E_T^{j2} \cdot (cosh(\eta_{j1} - \eta_{j2}) - cos(\phi_{j1} - \phi_{j2}))}.$$

If there are more than two jets in the event, the two jets with highest dijet
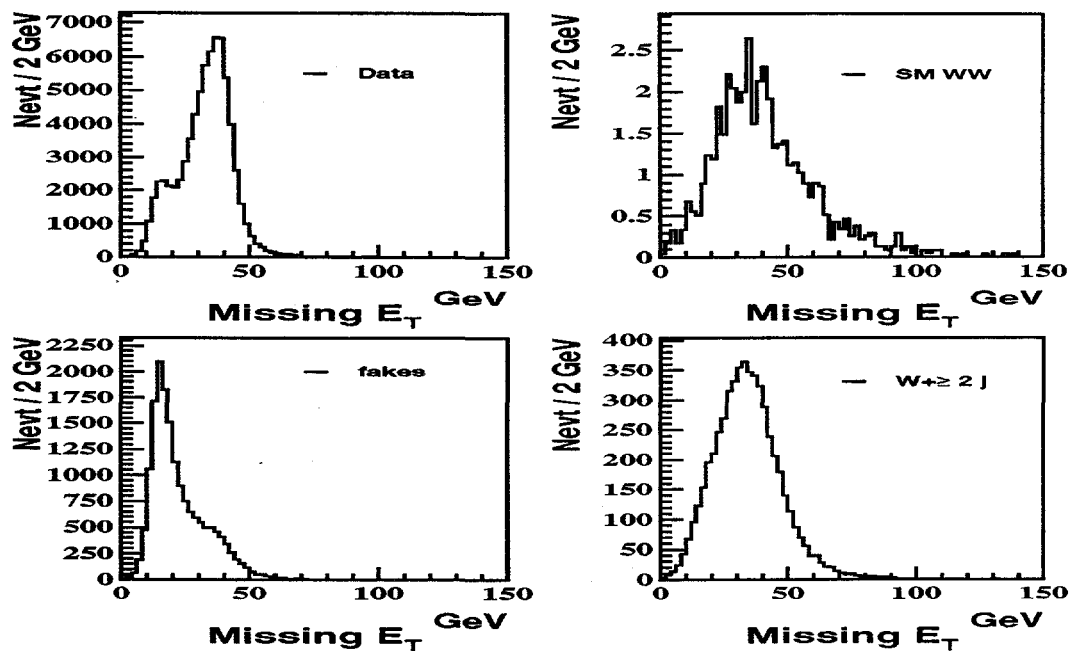
Figure 5.2: Missing E_t distributions of our samples. The QCD-FAKES distribution peaks in the same place as the lower peak in the data distribution.
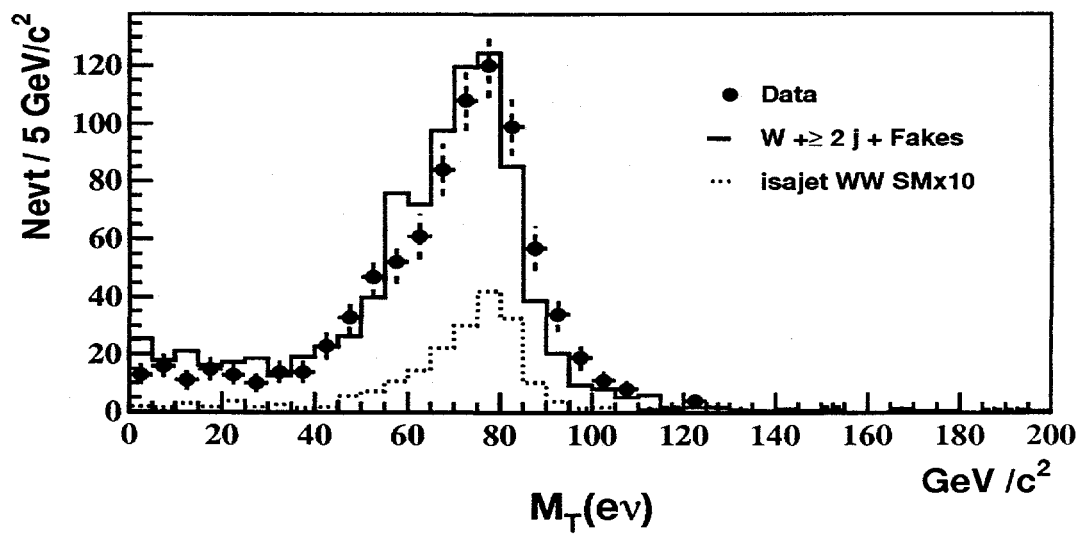
Figure 5.3: Distribution of the transverse mass of the electron and $\not{E}_T$ system.

invariant mass from the three leading jets are used. Fig. 5.4 shows the E_T^j distributions for the two leading jets, and Fig. 5.5 shows the M_{jj} distribution for data, and major backgrounds. Good agreement between the candidates and the sum of major backgrounds is evident.
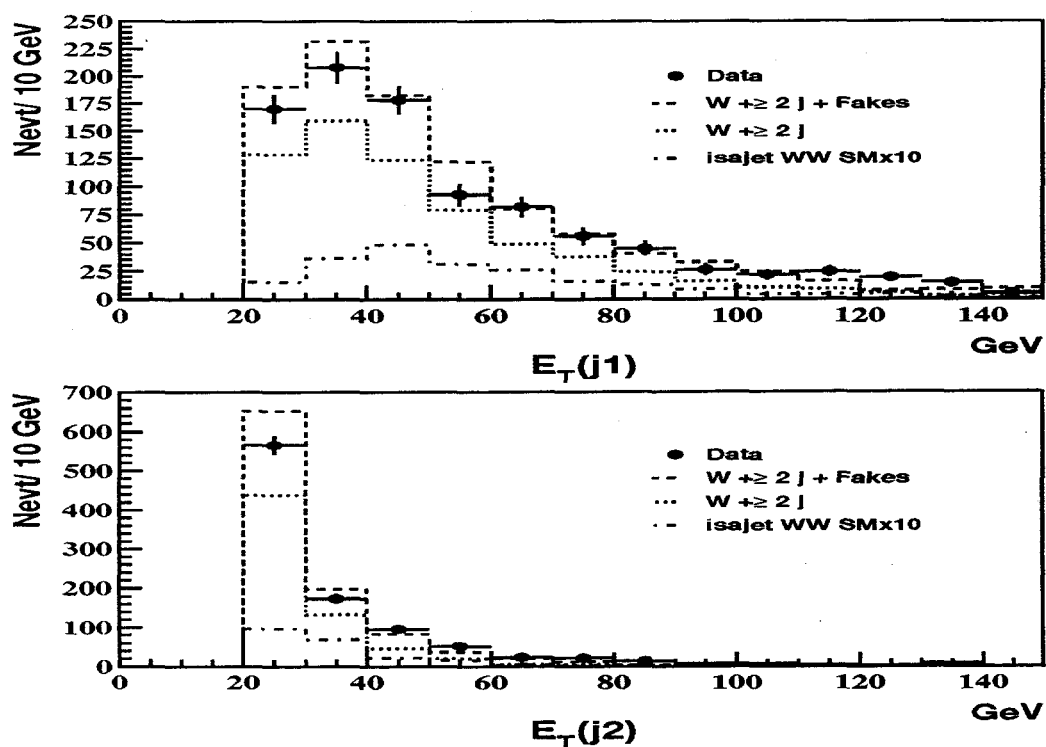
Figure 5.4: E_T^j distributions of the two leading jets in the samples.

The M_{jj} distributions for $WW \rightarrow e\nu jj$ and $WZ \rightarrow e\nu jj$ production for the SM couplings are shown in Fig 5.6. The peak of the distribution of $WW \rightarrow e\nu jj$ is at 77.3 GeV/c^2, which is about 3 GeV/c^2 lower than the nominal mass of the W (80.3 GeV/c^2). The peak of the distribution of $WZ \rightarrow e\nu jj$ is at 86.6 GeV/c^2, which is

about 4.6 GeV/c^2 lower than the nominal mass of the Z (91.2 GeV/c^2). The shift to

the lower masses may be due to: a possible error in the jet energy scale, losses due

to gluon radiation not accounted by the jet-out-of-cone correction, energy taken away

by extra jets due to Final State Radiation (FSR), or one of the two jets in the mass

calculation is from Initial State Radiation (ISR). For the cut we chose two sigma (-

30 GeV/c^2) to the left and two sigma (+ 30 GeV/c^2) to the right of the W peak (80

GeV/c^2). We did not take into account the WZ contribution for this cut since it is

less than 15%.
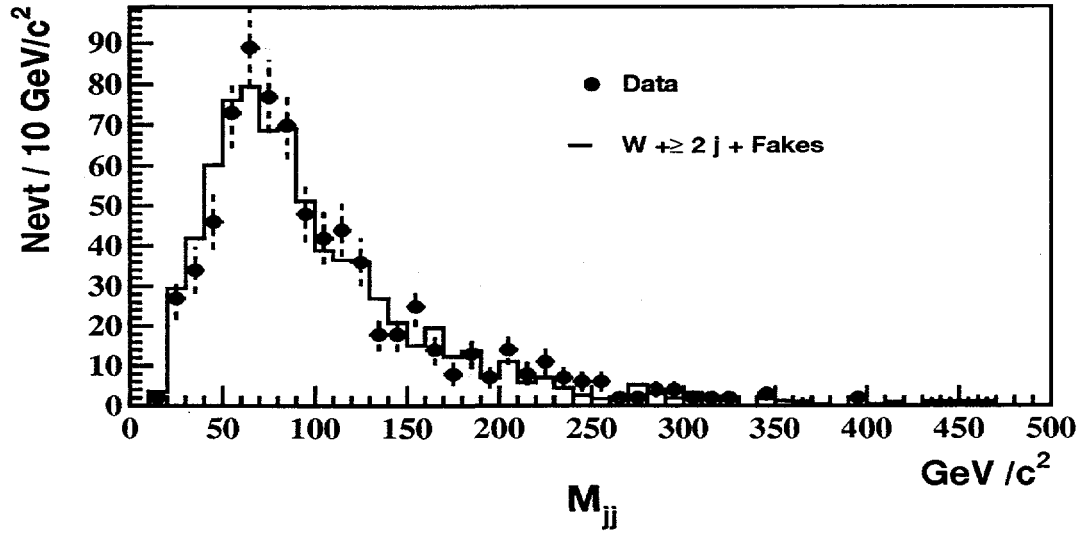
Figure 5.5: Invariant mass distribution of two jets.

Fig. 5.7 shows the distributions of $|p_T(e\nu) - p_T(jj)|$ for SM W pair production

events (upper plot) and $t - \bar{t}$ production events (lower plot). For the W pair production

events, this distribution should be peaked at zero and have a symmetric gaussian
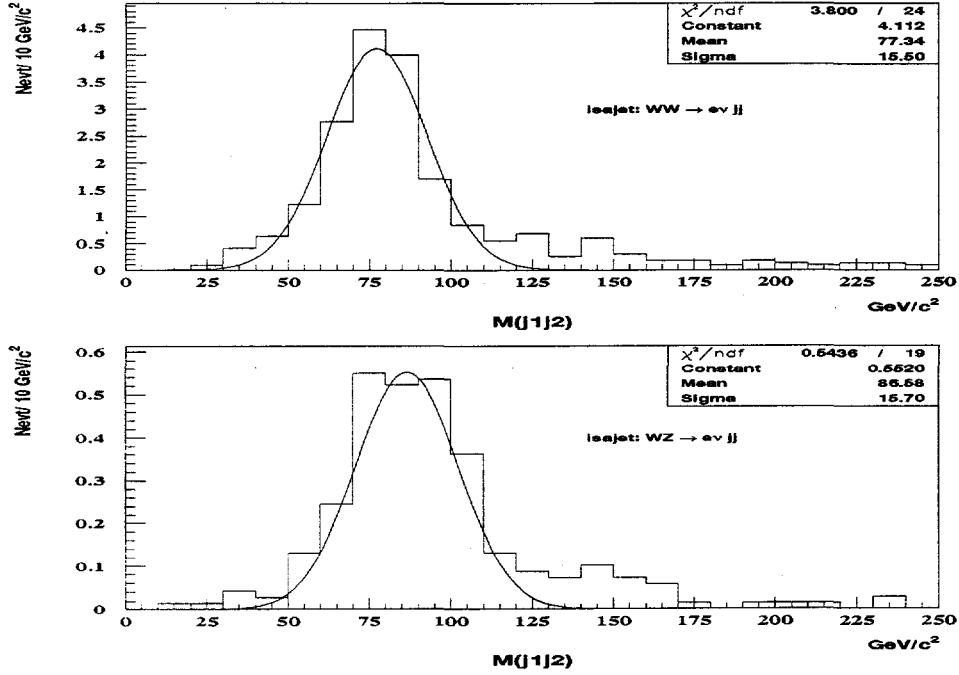
Figure 5.6: Distributions of the invariant mass of two jets in $WW \rightarrow e\nu jj$ (upper) and $WZ \rightarrow e\nu jj$ (lower) isajet SM events.

shape. The width of the gaussian distribution is determined mainly by the jet energy resolution. On the other hand for the $t - \bar{t}$ events, the distribution should have a positive average value and a broader and asymmetric shape due to additional b jets in the events. A cut on $|p_T(e\nu) - p_T(jj)|$ can reduce the background from $t - \bar{t}$ production. Based on this, we required that $|p_T(e\nu) - p_T(jj)|$ must be less than 40 GeV/c. This cut reduces approximately 1% of the SM signal, but at least 15% of the $t - \bar{t}$ background. The effect of this cut on other backgrounds is similar to its effect on the SM signal. The choice of 40 GeV/c (2.5 sigmas) is based on the WW SM signal resolution (16 GeV/c). If we had chosen a tighter cut of 2 sigmas, then we would have

lost 5% of the signal, but only around 20% of the $t - \bar{t}$ background.
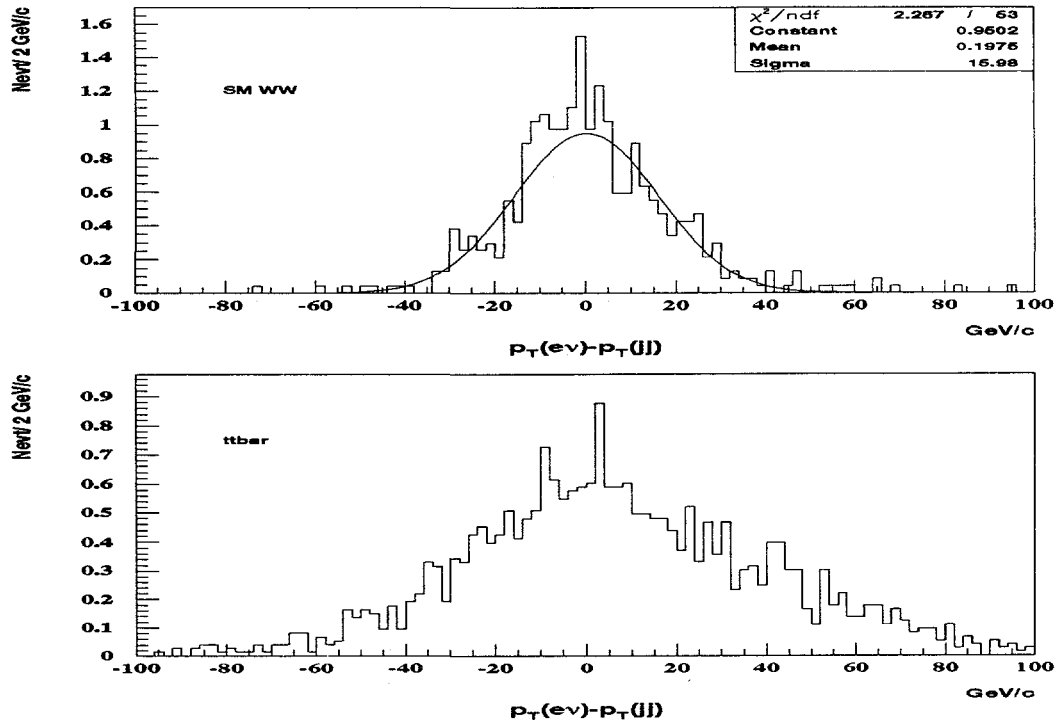
Figure 5.7: $p_T(e\nu) - p_T(jj)$ distributions for WW SM signal (upper) and top background (lower) after the 2 jet requirement.

The data satisfying the above selection criteria yielded 399 events. Fig. 5.8 (upper plot) shows the scatter plot of $p_T(e\nu)$ versus $p_T(jj)$ for candidate events after the mass window cut. The width of the band reflects both the resolution and the boost of the $e\nu jj$ system. The lower figure shows the scatter plot of $p_T(e\nu)$ versus M_{jj} before the mass window cut. There are no obvious structures in the distribution. The inclusion or exclusion of any candidate in the final sample is purely driven by the statistics and energy scale uncertainties, which are reflected in the statistical and

systematic errors for the results.
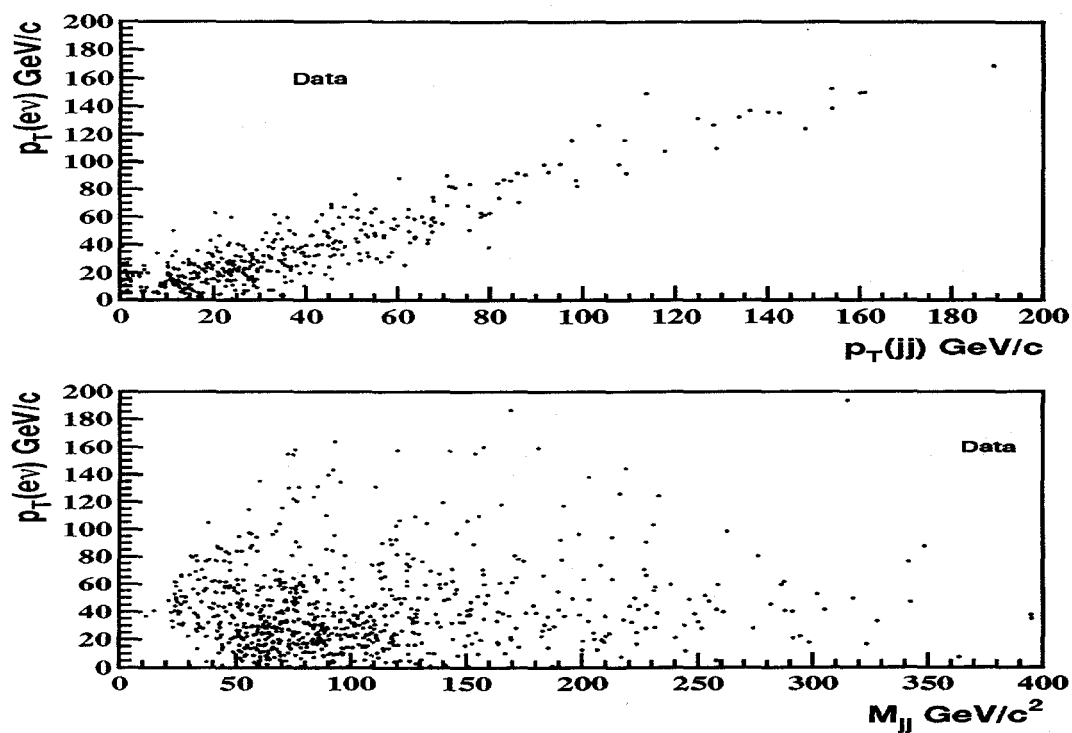
Figure 5.8: Scatter plots of $p_T(e\nu)$ versus $p_T(jj)$ (upper) and $p_T(e\nu)$ versus M_{jj} (lower).

Chapter 6

Background Estimations

There are many sources of background to $WW/WZ \rightarrow e\nu jj$. They are usually divided into two categories based on the nature of the final state objects. They are: physics backgrounds consisting of physical processes which resembles the signal of interest, and instrumental background which are events with final state objects misidentified or mismeasured.

6.1 Instrumental background

The major source of this background comes from QCD multi-jet events where one of the jet showers is mainly in the electromagnetic calorimeter and is misidentified so as an electron, and another jet is mismeasured sufficiently or fluctuates enough to pass the $\not{E}_T$ cut. Even though the probability for electron misidentification due to statistical fluctuations is small, the large cross section for multijet events makes this

background significant.

Events with high EM fraction jets and large $\not{E}_T$ can fake candidate events. To measure the fake contribution a QCD multijet background sample is used in which we require a 'bad electron' in the data sample; that is, an electromagnetic cluster satisfying electron triggers but failing electron-id. Now assuming that the measured $\not{E}_T$ is not strongly correlated to the misidentification of the jet as an electron, we can use the shape of the $\not{E}_T$ spectrum of this sample to describe the QCD–FAKE background. Furthermore, with the assumption that the contribution of the signal events in the low $\not{E}_T$ region in the QCD multijet sample is negligible, the fake sample can be normalized to the data in the low $\not{E}_T$ region and the $\not{E}_T$ distribution for the 'bad electrons' can be extrapolated under the signal region of the 'good' sample [64].

To estimate the multi-jet background we need to use a trigger without a $\not{E}_T$ requirement since the signal filter already has a cut in missing E_T. Run 1b data had several L2 filters useful for this purpose. Two of these were EM1_ELE_MON and ELE_1_MON which were described above. We extracted two samples from these background filters based on the electron quality: 'good' electrons and 'bad' electrons. The 'good' electron event required an electron with the same quality cuts as described in subsection 4.2.2, while the 'bad' electron event required an EM cluster with

EM fraction > 0.95,

Isolation ≤ 0.15,

H Matrix $\chi^2 \geq 250$ or track match significance $\geq 10\ \sigma$.

To avoid biases we add the requirement that the EM object must pass the same

Level 2 cuts as the signal filter. The $\not\!\!E_T$ distribution for the 'bad' electron sample is

then normalized to agree with the $\not\!\!E_T$ distribution for the 'good' sample in the low $\not\!\!E_T$

region ($\not\!\!E_T$ < 15 GeV). Fig. 6.1 shows these two distributions (the good sample and

the bad sample).
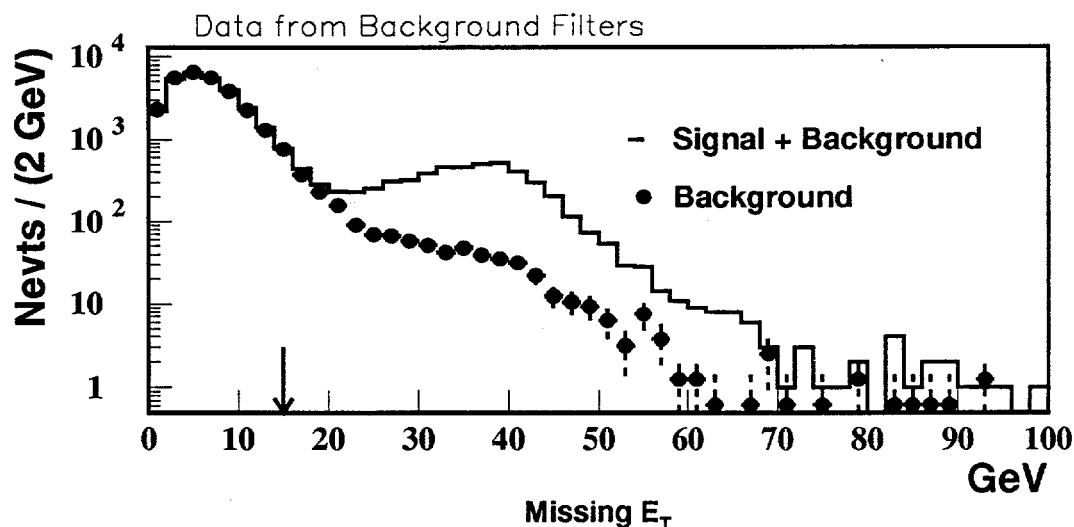
Figure 6.1: $\not\!\!E_T$ distributions for the two samples from background filters. The points have been normalized to the histogram for $\not\!\!E_T$ below 15 GeV.

The normalization factor, after the requirement of two jets is applied [1], calcu-

lated by the ratio of number of QCD–FAKE events over the number of candidate events

with $0 \leq \not\!\!E_T \leq 15$ GeV, is $N_F = 1.870 \pm 0.060$ (stat) ± 0.003 (sys). In the next

step we use the data from the signal filter, and extracte two samples one containing

---

[1]The normalization should take place only when the number of jets is specified, since the sources of fakes to W events with a different number of jets ($W+ \geq n$ jets) are different.

background and signal events ('good electrons' that we already got in the selection procedure) and the other containing only background events ('bad electrons'). The normalization factor N_F is then applied to the $\not{E}_T$ distribution for the background only sample [65]. The systematic uncertainty on the normalization factor is obtained by varying $\not{E}_T$ region from (0,12) to (0,18) GeV (based on the missing E_T resolution). Fig. 6.2 shows the distributions of $\not{E}_T$ for candidates and fakes, after the requirement of two jets.
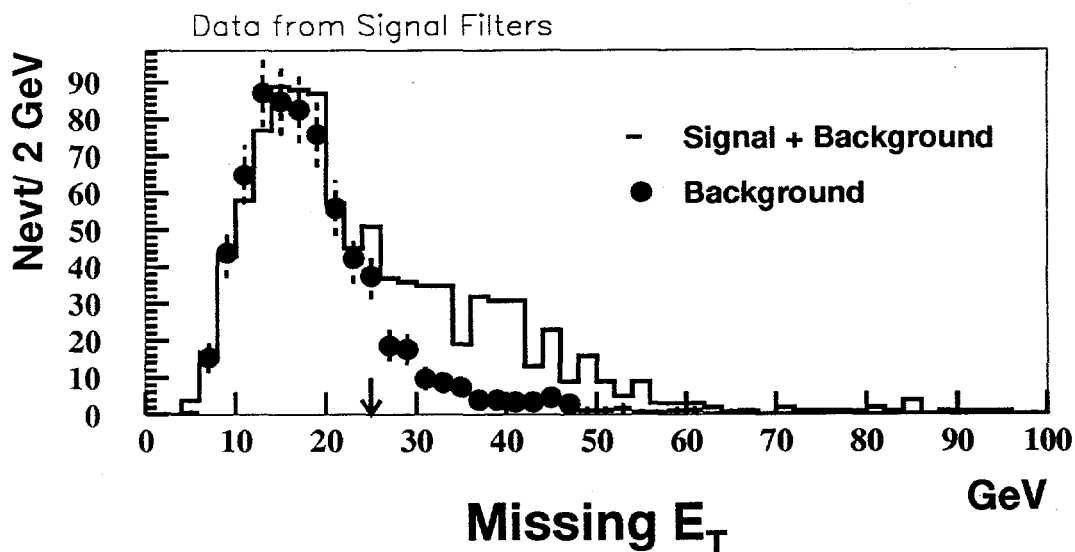
Figure 6.2: Distributions of $\not{E}_T$ of the candidate and fake samples.

The reason for the use of different filters to extract the normalization factor and the background fraction is due to the prescaled background filters, which would dominante the error on the background fraction if only the background filters were used, and due to the signal filter has already a cut in missing E_T.

After the selection procedure described above we estimate 104.3 ± 8.2 (stat) $\pm$ 9.1 (sys) background events. The systematic uncertainty (8.7%) includes: uncertainty on the normalization factor above (1%), variations when an alternative method [66, 67] is used to estimate this background (5.2%) (see appendix A), and variation for those in $\not{E}_T > 25$ GeV when the $\not{E}_T$ region (15,25) GeV is used for normalization (6.9%). The last variation estimates the possible contamination of signal in the fake sample.

6.2 Physics background

This type of background, as mentioned above, comes from physics processes with final state objects identical to our signal. They are estimated using Monte Carlo samples.

6.2.1 QCD $W + \geq 2$ j

$W + \geq 2$ jets QCD production is the most dominant background to our signal due to the large cross section for $W +$ jets event production. This background was estimated using a Monte Carlo sample generated with the program VECBOS followed by HERWIG to hadronize partons and DØGEANT for a detailed simulation of the detector. As mentioned above, the cross section value from the VECBOS program has a large error. The $W + \geq 2$ jets background events estimated with the VECBOS were therefore normalized to the signal data sample after the subtraction of QCD multijet contribution. In order to avoid the inclusion of true WW and WZ events in this
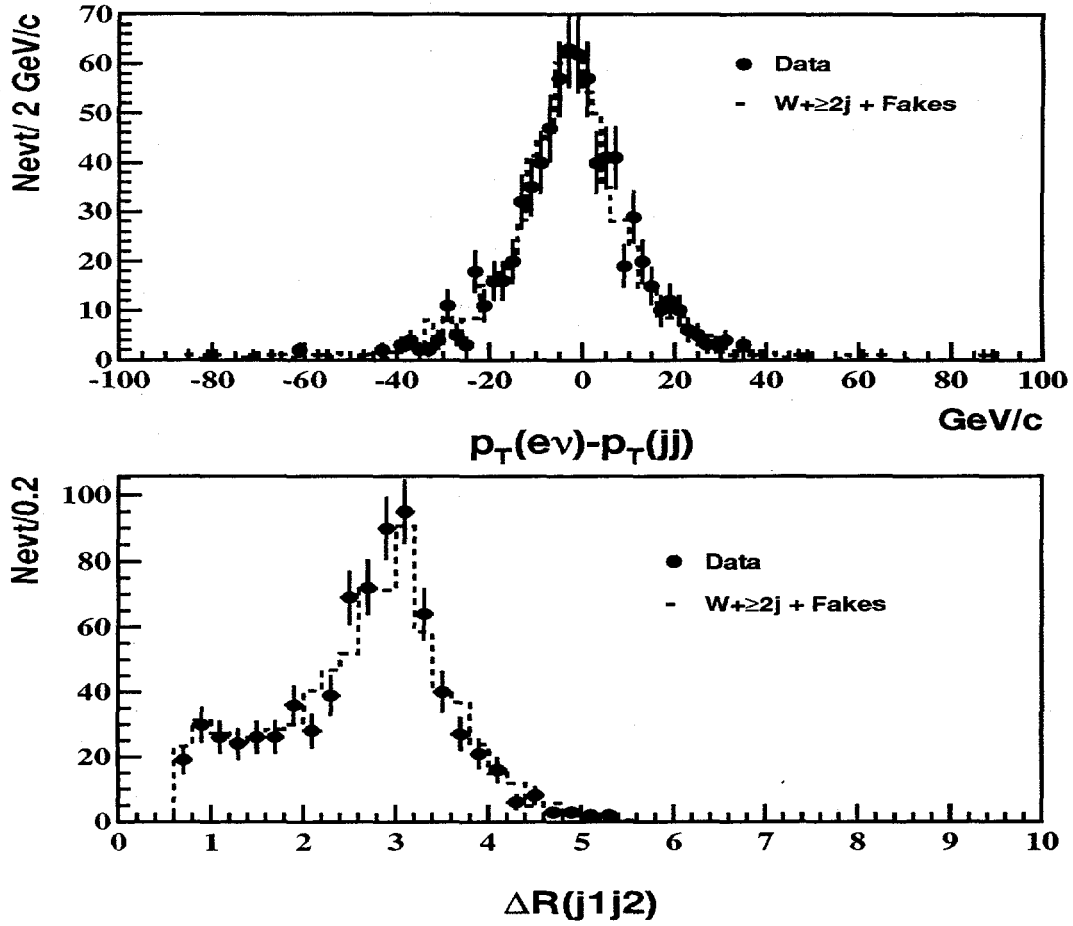
Figure 6.3: Upper plot: $P_T(e\nu) - P_T(jj)$ distribution before mass window cut. Lower plot: $\Delta R(jj)$ distribution for two jets.

procedure, we use only the event sample outside of the W mass peak ($50 < M_{jj} < 110$ GeV/c^2). Figure 5.5 shows two jet invariant mass distributions for data and the estimated background. The normalization factor is then

$$N_V = \frac{879}{392 - 251/(1.87 \pm 0.06)} = 3.41 \pm 0.31(stat) \pm 0.29(sys)$$

where 879, 392, and 251 are the numbers of VECBOS events, candidates, and QCD–FAKE

events outside the M_{jj} window respectively. Using this normalization factor we estimate 279.3 ± 27.2 (stat) ± 23.8 (sys) events in the candidate sample. The systematic uncertainty is due to the QCD-FAKE normalization (6.9%), jet energy scale (4%) and the variation when the M_{jj} cut is changed to (40,120) or (60,100) $\mathrm{GeV}/\mathrm{c}^2$ (3%). The cross section of $W+ \geq 2$ jets determined with this method is ($38795/([3.4\pm0.3]\times[76.5\pm4.1]$ $=)$ 149.15 ± 15.4 pb (where 38795 is the number of VECBOS events generated, 3.4 ± 0.3 is the normalization factor N_V and 76.5 ± 4.1 is the integrated luminosity of this analysis), which is consistent with the value (135 pb) given by the VECBOS program. Fig. 6.3 shows $|p_T(e\nu) - p_T(jj)|$ and $\Delta R(jj)$ distributions, which are important measures for how well background estimates describe the jets in the data. The backgrounds include the $W \geq 2$ jets and QCD-FAKE contributions. The data and the backgrounds agree well.

6.2.2 $\quad t\bar{t} \to W^+W^-b\bar{b} \to e\nu jjX$

The $t\bar{t} \to W^+W^-b\bar{b} \to e\nu jjX$ events feed in to the candidate sample, since no limit on the number of jets is applied for a higher efficiency. A sample, simulated with ISAJET with $m_t = 170$ $\mathrm{GeV}/\mathrm{c}^2$, were used to estimate this contribution. We found it to be small, 3.4 ± 0.3 (stat) ± 1.2 (sys) events. The normalization was done based on the DØ cross section measurement (5.2 ± 1.8 pb) [68]. The error in this measurement (35%) is included as systematic uncertainty in our analysis.

6.2.3 $WW/WZ \to \tau\nu jj \to e\nu\nu jj$

Since this contribution is small, and no separate signal simulation is available, we will treat it as background. After event selection we found $0.15\ ^{+0.16}_{-0.08}$ (stat) $\pm$ 0.01 (sys) events. This estimate was done using ISAJET. Normalization was done based on the cross section (9.5 pb for WW production and 2.5 pb for WZ production), and the systematic uncertainty is due to the largest side of the asymmetric theoretical prediction error (8.4%) [16].

6.2.4 $ZX \to e^+e^-X$

$ZX \to eeX$ processes can produce events which could fake the signal. These events may contaminate the candidate sample if one electron goes through a crack in the detector and is measured as missing transverse energy in the event. From a sample of 10000 ISAJET $ZX \to e^+e^-X$ events generated none of them survive the selection procedure. The background from events of this type is negligible.

6.2.5 $ZX \to \tau^+\tau^-X \to e\nu jjX$

$ZX \to \tau\tau X$ processes can produce events which could fake the signal if due to statistical fluctuations we pick one or two jets from the ISR or FSR with enough energy to feed in the mass window. From a sample of 10000 PYTHIA $ZX \to \tau\tau X$ generated events none of them survive our selection. The background events from this source is negligible.

Chapter 7

Efficiencies, Predictions, and

Uncertainties

When we measure a physical process, we are always interested in how often

this process occurs, what we know about such processes and how much confidence we

have in the measurement. In this chapter all these points are addressed.

7.1 Electron Identification Efficiency

The efficiencies of all the electron identification cuts, described in chapter 4,

were studied using the $Z \to ee$ event data sample from the 1993-1995 Run, which fired

the EM2_EIS_HI filter[1]. To select an unbiased sample of electrons with a reduced level

---

[1]The EM2_EIS_HI L2 filter required two L2 electron candidates with $E_T > 20$ GeV which satisfied electron shower shape and isolation cuts. It used the EM_2_MED L1 and L1.5 trigger conditions. This means that at L1 there must be two EM towers with $E_T > 7$ GeV, while at L1.5 at least one of these towers had to have $E_T > 12$ GeV and 85% of its energy in the EM section of the calorimeter.

of background we used events where one of the electron passed tag quality cuts[2] and therefore the second electron is unbiased. A given event may contribute twice if both electrons passed the tag cuts. Then the efficiency of the cuts for electrons is given by

$$\varepsilon = \frac{\varepsilon_s - \varepsilon_b f_b}{1 - f_b}$$

where ε_s is the efficiency measured in the signal region, ε_b is the efficiency measured in the background region, and f_b is the ratio of the number of background events in the signal region to the total number of events in the signal region. The signal region is defined as the region of Z invariant mass peak ($86 < m_{ee} < 96$ GeV/c^2). For the background estimation a sideband technique was used. The sideband regions are defined as ($61 < m_{ee} < 71$ GeV/c^2) and ($111 < m_{ee} < 121$ GeV/c^2). f_b in the signal region was estimated from an average of the number of events in the sidebands. The systematic uncertainties were estimated from comparisons with an alternative method which fits the M_Z spectrum to a Breit-Wigner curve convoluted with a Gaussian plus a linear background. The estimates from the two methods agree very well. The track-in-road efficiency is estimated in a similar manner, except that the $Z \to ee$ sample used for that measurement is allowed to include photons (i.e. possible electrons with a missing track) as the unbiased electron. Table 7.1 summarizes the estimated electron efficiencies.

---

[2]By tag cuts here we mean: EM fraction > 0.90, Isolation < 0.15, H-Matrix $\chi^2 < 100/200$ for CC/EC, and Track match significance $< 10\sigma$.

Cut	CC		EC	
description	Cut	ε	cut	ε
H-matrix χ^2	< 100	0.946±0.005	< 200	0.950±0.008
EM fraction	> 0.95	0.991±0.003	> 0.95	0.987±0.006
Isolation	< 0.10	0.970±0.004	< 0.10	0.976±0.007
Track match	< 5	0.948±0.005	< 5	0.776±0.012
Track-in-road		0.835±0.009		0.858±0.006
All cuts		0.736±0.011		0.619±0.012

Table 7.1: Electron identification cuts and their efficiencies.

7.2 $W \to jj$ Selection Efficiency

The $W \to jj$ selection efficiency was parametrized as a function of p_T^W using events generated with ISAJET and PYTHIA programs, followed by a detailed simulation of the detector. We used multi-samples generated with different p_T thresholds to simulate the behavior of the $p_T(jj)$ with different anomalous couplings as were shown in Ref [75]. Fig 7.1 shows the ratio of the events left after the selection criteria are applied over the initial number of events per each bin. It has been proved that the use of a cone size as narrow as $\mathcal{R} = 0.3$ for jet reconstruction ensures a higher efficiency. However, we have chosen to use a cone size of 0.5 to avoid the large uncertainties in the jet energy scale of the 0.3 cone algorithm, and the undesired splitting of jets. The roll-off of the efficiency above 250 GeV/c is high enough to contain all our data. The efficiency obtained from ISAJET was used as a lookup table to estimate the efficiencies of the $WW(WZ)$ process, which is smaller than that from PYTHIA in the high p_T region, and therefore gives more conservative results to the WW/WZ cross section and anomalous

coupling measurements. The differences between these two parametrizations will be included as a systematic uncertainty.
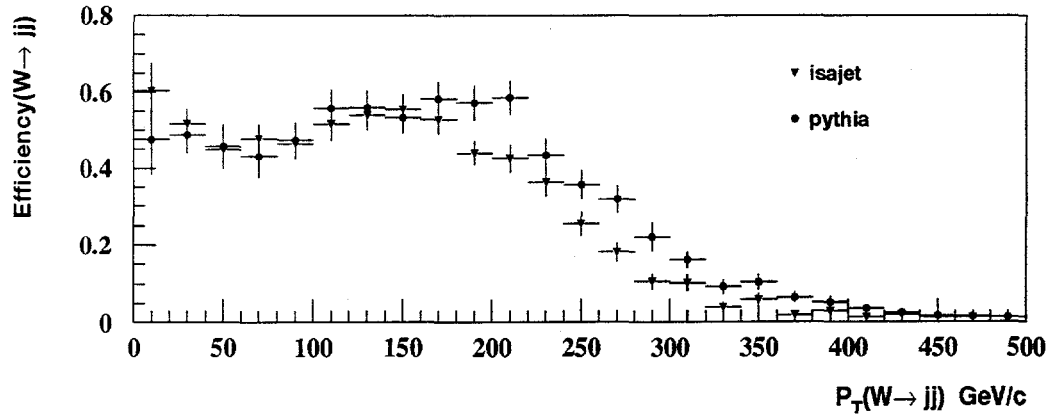
Figure 7.1: Efficiency for $W \to jj$ selection as a function of p_T^W

7.3 Overall Selection Efficiency

The overall selection efficiency reflects all the identification efficiencies, and kinematical and geometrical acceptance of a given process. We calculated the overall event selection efficiency as a function of the coupling parameters using the Zeppenfeld-Baur event generator and a fast detector simulation program which incorporates the detector resolutions. For the case of the Standard Model couplings we also calculated the overall efficiency using ISAJET to check the results from the fast generator. The estimated efficiencies from the two methods are consistent.

Using ISAJET (followed by a full simulation of the detector) we generated around 2500 $WW{\to}e\nu jj$ events and 1000 $WZ{\to}e\nu jj$ events with SM couplings. The structure function used was CTEQ2L [69]. We found that the event selection efficiency using these samples is estimated to be (13.44 ± 0.80) % for the $WW{\to}e\nu jj$ signal. and (15.70 ± 1.35) % for the $WZ{\to}e\nu jj$ signal. The errors are statistical only. The combined efficiency for $WW + WZ{\to}e\nu jj$ is given by

$$\frac{\epsilon_{WW} \cdot \sigma Br(WW{\to}e\nu jj) + \epsilon_{WZ} \cdot \sigma Br(WZ{\to}e\nu jj)}{\sigma Br(WW{\to}e\nu jj) + \sigma Br(WZ{\to}e\nu jj)} = (13.71 \pm 0.72)\%.$$

For the fast event simulation, we generated over 30000 events with various anomalous couplings. We calculated the total efficiency for SM couplings to be 14.7% $\pm$ 0.2% (stat) $\pm$ 1.2% (sys) for $WW{\to}e\nu jj$ and 14.6% $\pm$ 0.4% (stat) $\pm$ 1.1% (sys) for $WZ{\to}e\nu jj$. The systematic uncertainty (7.8%) includes: (1%) statistics of the fast MC, (1%) trigger and electron efficiency, (5%) $\not{E}_T$ smearing and p_T kick. (5%) different MC programs for $W{\to}jj$ parametrization, and (3%) jet energy scale for $W{\to}jj$ parametrization. (A more detailed description of these uncertainties is given below). The combined efficiency is 14.7% $\pm$ 0.2% (stat) $\pm$ 1.2% (sys). Within the errors, the combined efficiency estimated with the fast simulation is consistent with the value obtained from ISAJET.

7.4   Standard Model Prediction

The SM Prediction was calculated based on the ISAJET event generator followed by DØGEANT detector simulation program and the Zeppenfeld-Baur event generator followed by a fast detector simulation program.

Using ISAJET we found that the predicted number of events with SM couplings, after the event selection described in chapter 5, is 14.3 ± 1.3 (stat) events for WW production and 2.3 ± 0.2 (stat) events for WZ production, which means that we expected a total of 16.6 ± 1.4 (stat) SM events for $WW + WZ \rightarrow e\nu jj$ production. We have normalized the sample using the theoretical cross section (9.5 pb for WW and 2.5 pb for WZ).

In the case of the Zeppenfeld-Baur event generator with a fast detector simulation we used the estimated efficiencies above and the $\sigma \cdot Br$ from the event generator: $\sigma \cdot Br(p\bar{p} \rightarrow WW \rightarrow e\nu jj) = 1.26 \pm 0.18$ pb, and $\sigma \cdot Br(p\bar{p} \rightarrow WZ \rightarrow e\nu jj) = 0.18 \pm 0.03$ pb. The error here comes from the 14% of NLO uncertainty [10, 16]. The predicted number of events ($\mathcal{L}\epsilon\sigma$) with SM couplings are 16.2 ± 2.7 events based on 14.2 ± 2.4 WW events plus 2.0 ± 0.3 WZ events. The error (16.9%) is the sum in quadrature of the uncertainty in the efficiency above, uncertainty in the luminosity (5.4%) and that of the NLO corrections (14%). As we can see we found a very good agreement between the fast MC and ISAJET.

7.5 Anomalous Coupling Prediction

In order to study possible deviations of the SM couplings we calculated the predicted number of events for a number of values of the anomalous couplings. The couplings were varied in pairs. Since the predicted number of events depends on the form factor scale Λ_{FF}, we generated samples with this scale set to 1000, 1500 and 2000 GeV. Using the cross section times branching fraction from the event generator and the efficiency determined with the fast MC for events with each pair of coupling we obtained the predicted number of events for an integrated luminosity of 76.5 pb^{-1}. The combined prediction for $WW \to e\nu jj$ and $WZ \to e\nu jj$ assuming that the couplings for WWZ are equal to the couplings for $WW\gamma$ is shown in Fig. 7.2 using $\Lambda_{FF} = 1.5$ TeV.
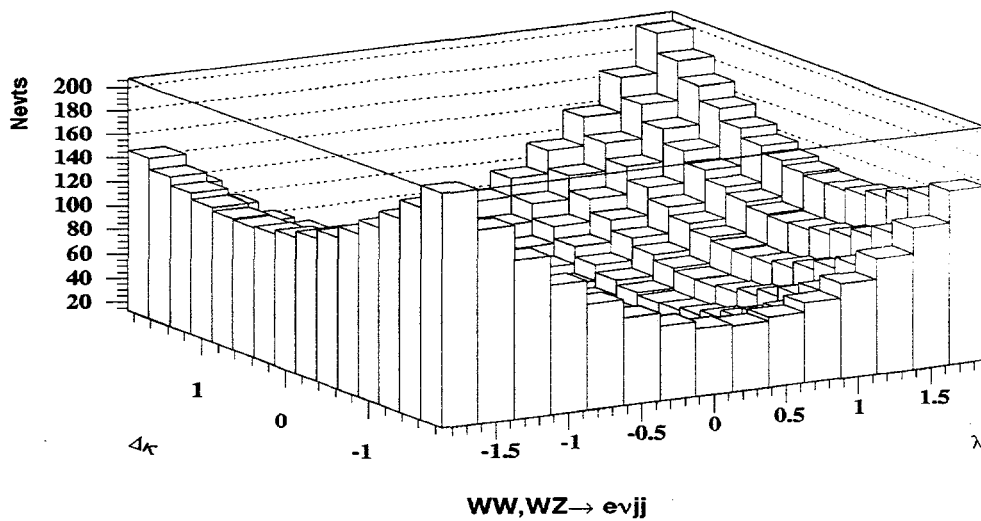
Figure 7.2: Predicted number of events as a function of λ and $\Delta\kappa$ after event selection.

For a given value of Λ_{FF}, the predicted number of events is described by a quadratic function of the anomalous couplings (λ, κ):

$$N_{pred}(\lambda, \Delta\kappa) = a + b\lambda + c\lambda^2 + d(\Delta\kappa) + e(\Delta\kappa)^2 + f\lambda(\Delta\kappa)$$

where a to f are coefficients, and the value of a gives the predicted number of SM events. In practice, to obtain $N_{pred}(\lambda, \Delta\kappa)$ at all values we generated Monte Carlo events for a small set of λ and $\Delta\kappa$ values and then fit the predicted number of events at each $\lambda - \Delta\kappa$ grid point to the above function form. For each form factor scale we fit a set of 49 points evenly spaced in the allowed region of couplings.

7.6 Systematic Uncertainties

The uncertainties on the predictions mainly come from the size of the sample generated, parametrizations, detector response and luminosity. We will describe them next.

7.6.1 Uncertainties from the MC generation

Since we generated over 20000 events for each pair of couplings the total statistical uncertainty for all the coupling values is less than 1%. The uncertainty of the choice of the parton distribution function (pdf) should not be included, because we are using the pdf which give us the lowest cross section at NLL, and therefore the results are the most conservative. But we must include the 14% uncertainty [10, 16]

for the effect of higher order QCD corrections when the '$K - factor$' is included in the leading-order result.

7.6.2   Uncertainties from lepton efficiencies

The uncertainties due to the parametrization of the detector response to leptons includes: 1% due to the electron efficiency parametrization, which is extracted from the uncertainty of the electron trigger and selection efficiency, 5% due to the smearing of $\not{E}_T$, which is the largest relative change of the predicted number of events at various couplings when the smearing and/or the p_T kick of the system are turned off.

7.6.3   Uncertainties from $W \to jj$ efficiency parametrization

The $W \to jj$ efficiency parametrization could be affected by the jet energy scale, the accuracy of ISR/FSR simulation and parton fragmentation as well as the statistics of the samples used to determine the parametrization.

The energy scale correction performed by CAFIX has an uncertainty that goes from 5% at 20 GeV to 2% at 80 GeV and then again goes to 5% at 350 GeV [51]. The impact of this uncertainty is studied recalculating the efficiency with the jet energy scale changed by $\pm 1\sigma$. Then the largest relative change of the accepted number of events for various couplings is found to be 3%.

To include any uncertainty in the accuracy of the ISR/FSR simulation or parton fragmentation we parametrized the $W \to jj$ efficiency using two sets of samples

generated with different event generators (ISAJET and PYTHIA). We found that the efficiency obtained with ISAJET is lower than that obtained with PYTHIA. The relative change of the numbers of accepted events at various couplings are less than 10%. We chose to use the efficiencies obtained from ISAJET because they give more conservative results to the WW/WZ cross section and anomalous coupling measurements. We take a half of the largest difference in these two parametrizations as an additional uncertainty (5%).

The relative change due to the statistical error of the $W \rightarrow jj$ parametrization (shown as error bars in Fig 7.1), is calculated for each coupling based on the formula

$$\Delta\epsilon = \frac{\sqrt{\sum_i^{p_T(W)bins}[(N_{in}^i \times \Delta\varepsilon_i)^2 + N_{in}^i \times \varepsilon_i^2]}}{\sum_i^{p_T(W)bins} N_{in}^i}$$

which was derived from the definition

$$\epsilon = \frac{\sum_i^{p_T(W)bins} N_{in}^i \times \varepsilon_i}{\sum_i^{p_T(W)bins} N_{in}^i}$$

where the relative error of $\sum_i^{p_T(W)bins} N_{in}^i$ was ignored. ε_i is the efficiency for $W \rightarrow jj$ selection for $p_T(W)$ bin i, and N_{in}^i is the number of events that fall in this $p_T(W)$ bin. The relative changes, $\Delta\epsilon/\epsilon$, at various couplings are found to be less than 2%.

7.6.4 Luminosity uncertainty

In chapter 3, we discussed how the luminosity is measured in DØ, as well as how the uncertainty is determined. Here we only quote the result, which is 5.4% [33].

7.6.5   Uncertainty on the parametrization of the predictions

Since we are using a small set of points to find $N_{pred}(\lambda, \Delta\kappa)$. we must include

the uncertainty of this parametrization (5%), which comes from the deviation between

the fit and the points known at various couplings when the errors from the fit are

propagated using the quadratic parametrization above.

7.6.6   Summary of Uncertainties

All the uncertainties to the $e\nu jj$ prediction are summarized in table 7.2. Also

shown are the calculated uncertainties for the background estimates, discussed in

chapter 6.

Source of Error	Relative uncertainty
Luminosity uncertainty	5.4%
QCD corrections	14%
Electron and trigger efficiency	1%
Statistics of fast MC	1%
$\not{E}_T$ smearing	5%
Jet energy scale	3%
ISAJET VS. PYTHIA	4%
Statistics for effic($W \rightarrow jj$)	2%
Parametrization of prediction	5%
Total Uncertainty in Prediction	17.5%
Total Background Uncertainties	7%

Table 7.2: Relative uncertainties calculated in Run 1B $e\nu jj$ analysis.

Chapter 8

Results

The experimental results are discussed in detail in this chapter. Comparisons between predictions with the Standard Model and anomalous couplings are made. At the end of the Chapter the results of this work is combined with our published results from Run 1A to obtain further improvements in the limits on anomalous couplings.

8.1 Comparison with SM Prediction

The observed data in the $e\nu jj$ channel is expected to be dominated by QCD $W + \geq 2$jets production. After the event selection we found 399 candidates for which we estimated 387.1 background events. The number of events expected from the Standard Model WW/WZ process is 16.2 events after the kinematic selection. The kinematic distributions, for all the variables shown in chapter 5, between data and

background estimates agree very well, and the small differences are within the estimated uncertainties. Table 8.1 summarizes the calculated numbers of events for data candidates, estimated backgrounds and SM predictions.

	N. of events
QCD Multijets	104.28±12.25
QCD $W+ \geq 2$ jets	279.25±36.14
$t\bar{t}{\rightarrow}e\nu$ jjX	3.40±1.21
$WW/WZ{\rightarrow}\tau\nu$ jj	$0.15^{+\ 0.16}_{-\ 0.08}$
Total Background	387.09±38.18
Data	399
SM $WW+WZ$ prediction	16.20±2.70

Table 8.1: Summary of $e\nu jj$ data and backgrounds

Fig. 8.1 shows the p_T distribution of the $e\nu$ system for data, background estimates, and SM predictions. The agreement is very good. We observed no statistically significant signal above the background. The ratio Signal/$\sqrt{\text{Background}}$ is less than 1.0. Although we observed no statistically significant signal above the estimated background, we can still set limits on the $WW/WZ \rightarrow e\nu jj$ production cross section by subtracting the backgound from the data. The upper limit on the SM cross section can be set using the efficiencies for SM WW and WZ production, the number of events for the candidates and the estimated backgrounds, the known branching fractions [6]: $Br(W{\rightarrow}e\nu)$, $Br(W{\rightarrow}hadrons)$ and $Br(Z{\rightarrow}hadrons)$, and assuming the SM ratio of the cross sections of $p\bar{p}{\rightarrow}W^+W^-X$ and $p\bar{p}{\rightarrow}W^{\pm}Z$
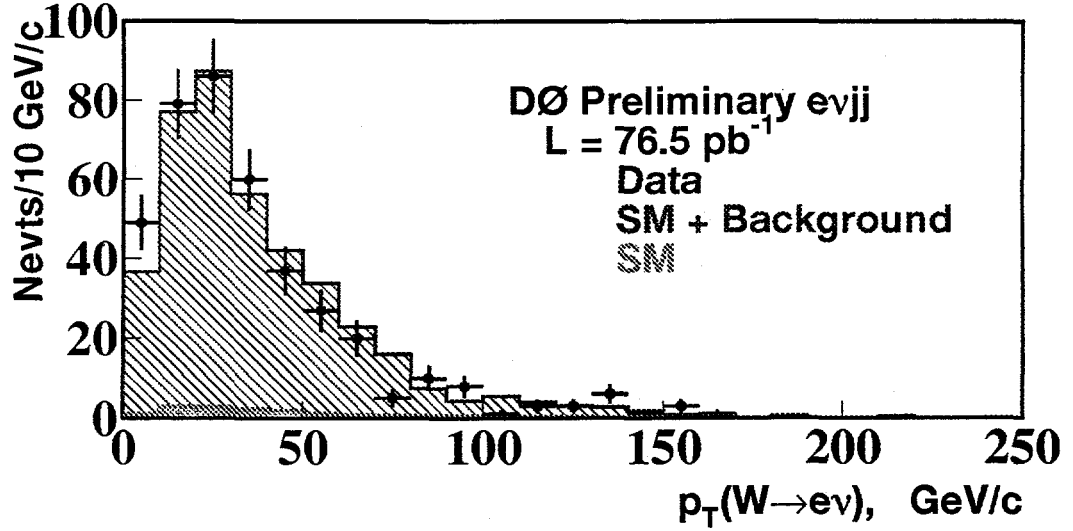
Figure 8.1: p_T distributions of the $e\nu$ system: data, total background plus SM prediction and SM prediction. The errors shown are just statistical.

$$\sigma(p\overline{p} \rightarrow WWX) < \frac{\sigma \cdot Br_{max}(CL)}{Br(W \rightarrow e\nu) \times \left(Br(W \rightarrow jj) + Br(Z \rightarrow jj) \cdot \frac{\sigma_{SM}(p\overline{p} \rightarrow W^+W^-X)}{\sigma_{SM}(p\overline{p} \rightarrow W^{\pm}ZX)} \right)}$$

where $\sigma \cdot Br_{max}$ is the cross section times branching fraction of the $WW + WZ$

production at a desired confidence level, given by

$$
\begin{aligned}
\sigma Br(WW \rightarrow e\nu jj) + \sigma Br(WZ \rightarrow e\nu jj) &= \frac{n-b}{\mathcal{L} \cdot \epsilon} \\
&= \frac{(399 \pm 19.97) - (387.09 \pm 38.18)}{(76.46 \pm 4.13) \cdot (0.15 \pm 0.02)} \\
&= 1.0 \pm 3.8
\end{aligned}
$$

where n is the number of candidates, b is the estimated background, $\mathcal{L}$ is the luminosity

and ϵ is the weighted efficiency for SM WW, WZ estimated from fast MC. Therefore

at 95% CL

$$\sigma \cdot Br_{max}(95\%CL) = 8.4 \text{ pb} \qquad \text{and} \qquad \sigma(p\bar{p}{\to}WWX) < 89.4 \text{ pb}$$

In the sample of 399 events satisfying the selection criteria, 18 events are found with $p_T > 100$ GeV/c, which are listed in table 8.2. 18.5 events are estimated to be background and 3.2 events SM production. Fig. 8.2 shows the lego plot for one of the high $p_T(e\nu)$ events. The absence of an excess of events with high p_T^W excludes large deviations from the SM couplings. The data is in good agreement with the $WW, WZ \to e\nu jj$ SM production.

Run	Event	$p_T(e\nu)$ [GeV/c]
77828	3108	106.3
78239	6824	165.7
82341	4310	131.7
82341	10956	145.9
85244	5513	136.3
88072	6520	125.1
88140	14875	152.0
88442	21692	135.4
89550	38785	153.0
90185	1990	118.9
90865	4127	157.9
90941	20709	119.8
90942	32687	110.4
91948	9522	130.2
91982	36502	131.2
92142	557	136.0
92738	2421	122.4
93018	14038	128.8

Table 8.2: Events passing the events selection and $p_T(e\nu) > 100$ GeV/c cut.
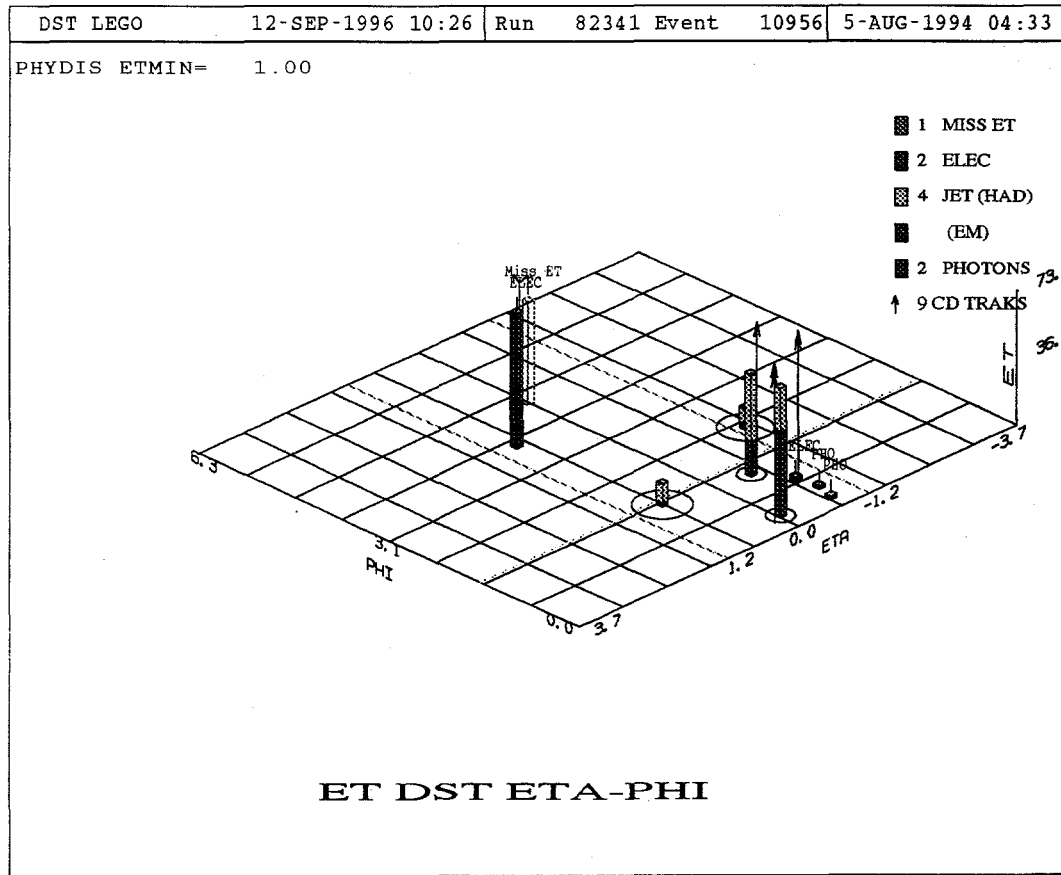
Figure 8.2: Lego plot of the candidate event, run 82341, event 10956.

8.2 Limits on the Anomalous Couplings

We have shown that there is a good agreement between the various distributions for data and estimated background, and concluded that there does not appear to be a signature for anomalous couplings. In this section, we will present the methods to set limits on anomalous couplings and the limits set with our data. Two methods

are used to estimate those limits, a counting method, and a likelihood fit to the p_T^W spectrum. Both methods are discussed. The limits are compared with limits from previous experiments.

8.2.1 Limit from the Counting Experiment

We have already discussed in the theoretical section and observed in chapter 7 that the number of events (cross section) increases for coupling parameters away from the SM values (see Fig. 7.2), especially at high p_T as shown in Fig. 2.2. Therefore, our analysis can be more sensitive to anomalous couplings if we set an appropriate threshold on p_T^W in order to remove almost all estimated background events, since the p_T distribution for background is softer than the predicted for WW and WZ production in the presence of anomalous couplings. It is obvious that with this cut the SM contribution is largely eliminated. The merit of such a cut is that the remaining events are more sensitive to the anomalous couplings than without this cut.

If we count the number of candidate events above this minimum p_T^W, make the background subtraction and take into account the uncertainties of the estimated backgrounds, we can set an upper limit on the number of observed events at a given confidence level (CL) α. Limits on the anomalous couplings can be extracted from the plane where:

$$N_{pred}(\lambda, \Delta\kappa) = N(\alpha)$$

The contour defined by this equation is an ellipse in the $(\lambda, \Delta\kappa)$ plane which defines

a finite area: the allowed deviation from the SM at α CL. The estimation of the upper limit $N(\alpha)$ is based on a Bayesian approach, and due to the small statistics the Poisson probability is used. The method takes the Poisson probability for the number of observed events and convolutes it with a Gaussian distribution for uncertainties in luminosity, efficiencies, and background [71].
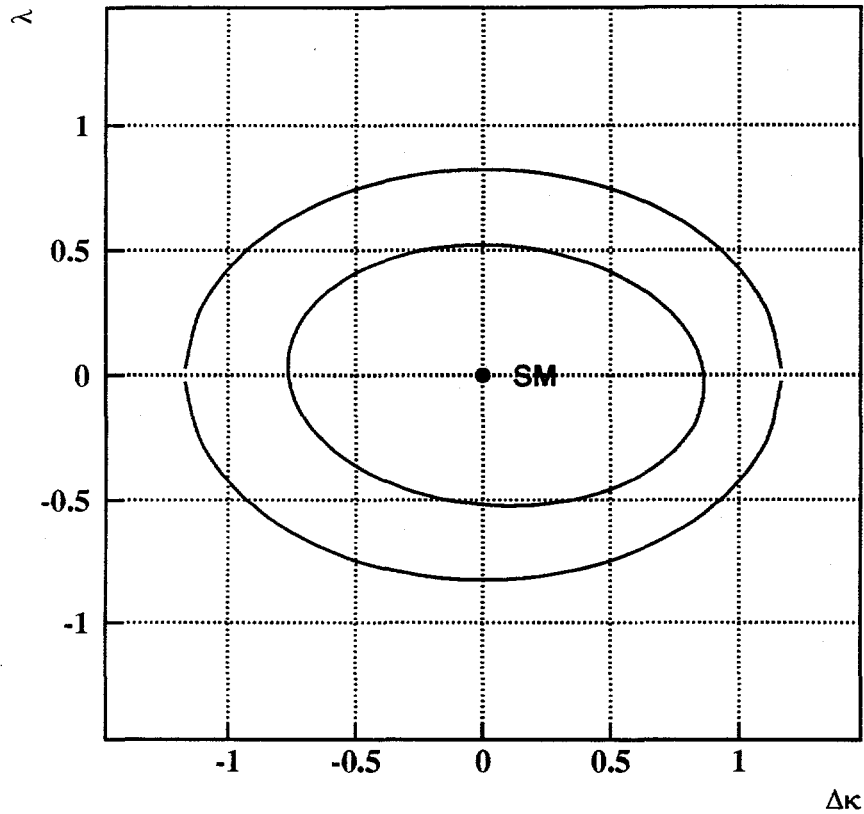
Figure 8.3: Limits using a p_T^W threshold of 170 GeV/c. Inner: Exclusion contour at 95% CL; Outer: Unitary limit with Λ =1.5 TeV.

The resulting limits for pairs $(\Delta\kappa, \lambda)$ calculated for $\Lambda_{FF} = 1.5$ TeV and $p_T^W >$ 170 GeV/c at 95%CL are shown in Fig. 8.3. We have assumed that the coupling for $WW\gamma$ and WWZ are equal. The numerical limits are summarized in table 8.3. The table also shows the limits for five different p_T^W thresholds. The limits shown in this table correspond to 95% CL limits for one degree of freedom, i.e. they are limits on the axis [6]. It is common to quote the limits of one coupling parameter when the other coupling is fixed to its Standard Model value.

p_T^W cut	candidates	background	SM $WW + WZ$	$\lambda_{\gamma=Z}$	$\Delta\kappa_{\gamma=Z}$
150	4	2.8	1.9	(-0.66,0.67)	(-0.96,1.08)
160	1	2.1	1.8	(-0.54,0.54)	(-0.79,0.89)
170	0	1.5	0.9	(-0.52,0.52)	(-0.76,0.86)
180	0	1.2	0.2	(-0.59,0.58)	(-0.87,0.96)
190	0	0.7	0.1	(-0.64,0.64)	(-0.96,1.05)
200	0	0.3	0.1	(-0.74,0.73)	(-1.13,1.20)

Table 8.3: Limits on λ and $\Delta\kappa$ at 95% CL as a function of p_T^W cut using the counting experiment method. The number of candidates, background estimates and SM predictions, are also shown. The limits are for $\Lambda_{FF} = 1.5$ TeV.

8.2.2 Limits from the p_T^W spectrum

The limits with the counting experiment method are relatively easy to obtain. However the method ignores extra information that may be found in the full p_T^W spectrum, and depends on the p_T cut choice as well as the overall normalization factors: i.e. luminosity, efficiencies, and QCD corrections. A more sophisticated method,

which avoids all these difficulties, is to fit the shape of kinematical distributions which are sensitive to anomalous couplings [72]. This method usually provides tighter limits, since it uses all the information contained in the differential distributions, and it is less sensitive to the overall normalization factors.

In the theoretical introduction has been indicated that the differential distribution which is most sensitive to anomalous couplings is the p_T^W distribution (for the case of WZ production the p_T^Z distribution is also very sensitive). This analysis uses the $p_T(W \to e\nu)$ spectrum rather than $p_T(W \to jj)$ or $p_T(Z \to jj)$ for a few reasons. In DØ the resolution of $p_T(e\nu)$(12.5 GeV/c) is better than $p_T(jj)$(16.7 GeV/c). Fig. 8.4 shows the difference of the momentum components between generated W and the reconstructed $e\nu$ or jj for MC $WW \to e\nu jj$ events. The corrections for jet energies are larger and more sophisticated than for electron energies. This point was discussed in chapter 4. There is also a small ambiguity for which of the two jets are assigned to the $W(Z)$.

The use of the differential cross sections in general and in particular to obtain limits on trilinear gauge boson couplings has been exploited by several analyses [8, 9, 12, 13, 14, 15, 25, 70]. In order to fit the p_T^W distribution, we can either use a binned or unbinned likelihood fit method. To decide which method is useful we have to look at the advantages and disadvantages of both. The unbinned fits rely on the exact shape of the background over the entire kinematic range, whereas a binned fit bins the background to avoid small fluctuations. Also the binned fit avoids the problem
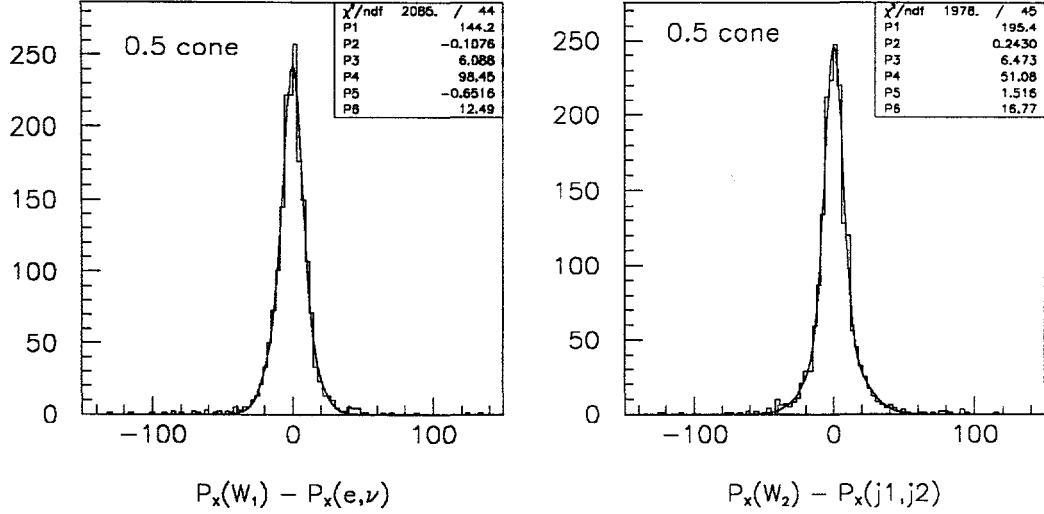
Figure 8.4: Difference of momentum components (p_x) of generated W and reconstructed $e\nu$ and jj of ISAJET WW events.

that arises from smearing of the data points with known detector resolutions when the bin width is comparable with these resolutions. For large statistics, estimators of the parameters, for a given distribution, should not depend on bin size. but for small statistics this is not the case. The bin width should be larger than the resolution of the data that is binned, but at the same time, there should be a sufficient number of bins to reflect the details of the shape. We use a modified binned p_T^W fit method [73] to obtain limits. The modification is based on adding an extra bin with no observed events to the p_T^W histogram, which improves the sensitivity to anomalous couplings. This modification is motivated by the observation that if the bin size is chosen using the standard approach of having approximately equal number of events per bin, the last bin would be extended to some large p_T^{max}. This would, however, neglect the

major difference between the Standard Model and anomalous coupling predictions. For the Standard Model the events are concentrated in the low p_T region, while in the anomalous couplings case a excess at high p_T is expected. Therefore the event with highest p_T contains essential information about the limits on the anomalous couplings. If the last bin is extended to some p_T^{max} this information is ignored. In order to maximize the sensitivity to the anomalous couplings, the last bin is chosen so that it contains no events. This uses the "null experiment" approach (the observation of no events above certain threshold) [73] to increase the sensitivity to anomalous couplings. The last bin should be chosen slightly above the p_T of the event with highest p_T so the smearing effect could not fluctuate the last data point into the last bin. This method is more or less insensitive to the total number of bins, as long as there are bins containing the observed events and a bin for the null experiment.

Based on the distribution of the $WW, WZ \rightarrow e\nu jj$ events, we have chosen two 25 GeV/c bins from 0 to 50 GeV/c, five 10 GeV/c bins from 50 to 100 GeV/c, two 20 GeV/c bins from 100 to 140 GeV/c, one 30 GeV/c bin from 140 to 170 GeV/c and a single bin above 170 GeV/c up to 500 GeV/c. The 500 GeV/c cutoff was introduced for technical reasons. The total cross section above this threshold is negligible for anomalous couplings of any strength allowed by the unitary limits. Each bin could be seen as an individual experiment and assumed uncorrelated. In each p_T^W bin i, the probability P_i for observing N_i events is given by the Poisson distribution:

$$P_i = \frac{(b_i + \mathcal{L}\epsilon\sigma_i(\lambda, \Delta\kappa))^{N_i}}{N_i!} e^{-(b_i + \mathcal{L}\epsilon\sigma_i(\lambda, \Delta\kappa))}$$

where b_i is the expected background in each bin, $\mathcal{L}$ is the luminosity, ϵ is the total detection efficiency and σ_i is the cross section for each bin. $\epsilon\sigma_i(\lambda, \Delta\kappa)$ is extracted from the fast Monte Carlo. The joint probability for all p_T^W bins is the multiplication of the individual probabilities P_i,

$$P = \prod_{i=1}^{Nbin} P_i.$$

Since the values $\mathcal{L}$, b_i, and ϵ are measured value with some uncertainty, we allow them to fluctuate around their nominal values with a Gaussian distribution of mean $\mu = 1$ and rms deviation of σ_x:

$$P' = \int \mathcal{G}_{f_n} df_n \int \mathcal{G}_{f_b} df_b \prod_{i=1}^{Nbin} \frac{e^{f_n n_i + f_b b_i}(f_n n_i + f_b b_i)^{N_i}}{N_i!},$$

where we have dropped $(\lambda, \Delta\kappa)$, $n_i = \mathcal{L}\epsilon\sigma_i$ is the predicted number of events, and

$$\mathcal{G}_x = \frac{1}{\sigma_x\sqrt{2\pi}} exp \frac{-(x-\mu)^2}{2\sigma_x^2}.$$

The integrals above are evaluated at 50 evenly spaced points between $\pm 3\sigma$. For convenience the log-likelihood, $L = logP'$, is used. The set of couplings that best describe the data is given by the the point in the $\lambda - \kappa$ plane that maximizes the likelihood given the above equation. The s-standard-deviation errors are evaluated along the contour $L_{max} - s^2/2$ [6].

As discussed in the previous subsection, it is common to quote the limits on one coupling when all the others are set to their Standard Model values. These axis limits in the "$\gamma = Z$" scenario at 95% CL ($s = 1.96$) are shown in table 8.4.
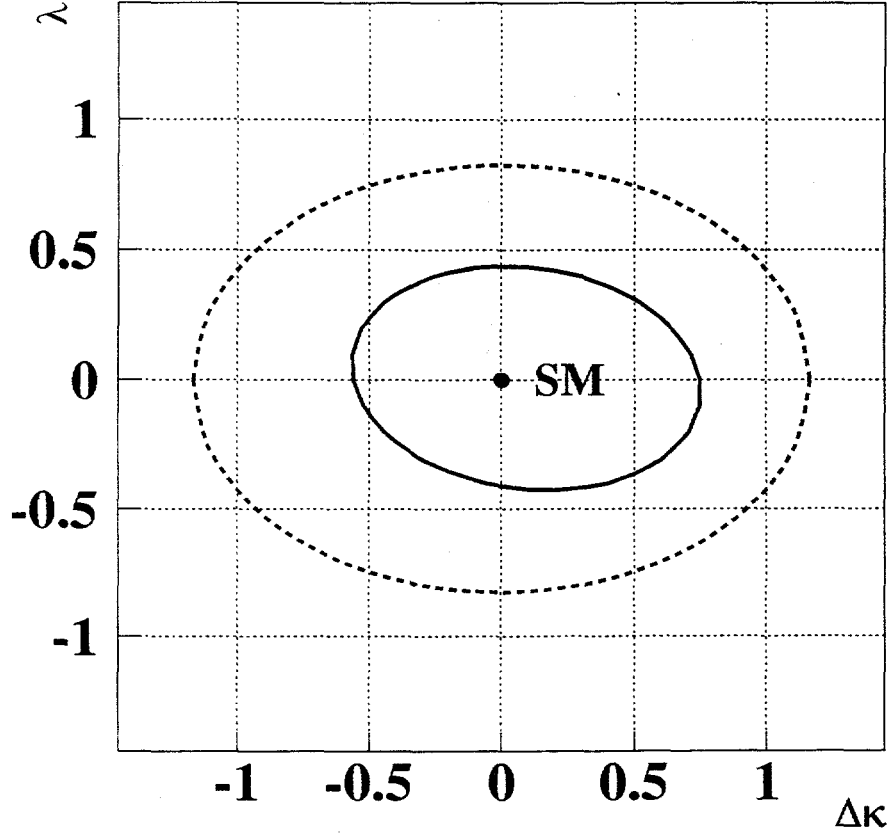
Figure 8.5: Limits from the p_T^W binned fit. Inner: 95% CL Exclusion contour, Outer: Unitarity limit with $\Lambda = 1.5$ TeV.

The corresponding contour with $\Lambda_{FF} = 1.5$ TeV is shown in Fig. 8.5. The limits for $\Lambda_{FF} = 1.5$ TeV, as well as the others, are tighter than those obtained from the counting experiment. The limits for $\Lambda_{FF} = 2.0$ TeV violate tree-level unitarity; they are just outside the unitary bound.

The method is somewhat more stable to different p_T^W minimum than the counting method, as discussed above and illustrated in Fig. 8.6, since the higher sensitivity to the anomalous couplings is contained in the highest p_T^W events.
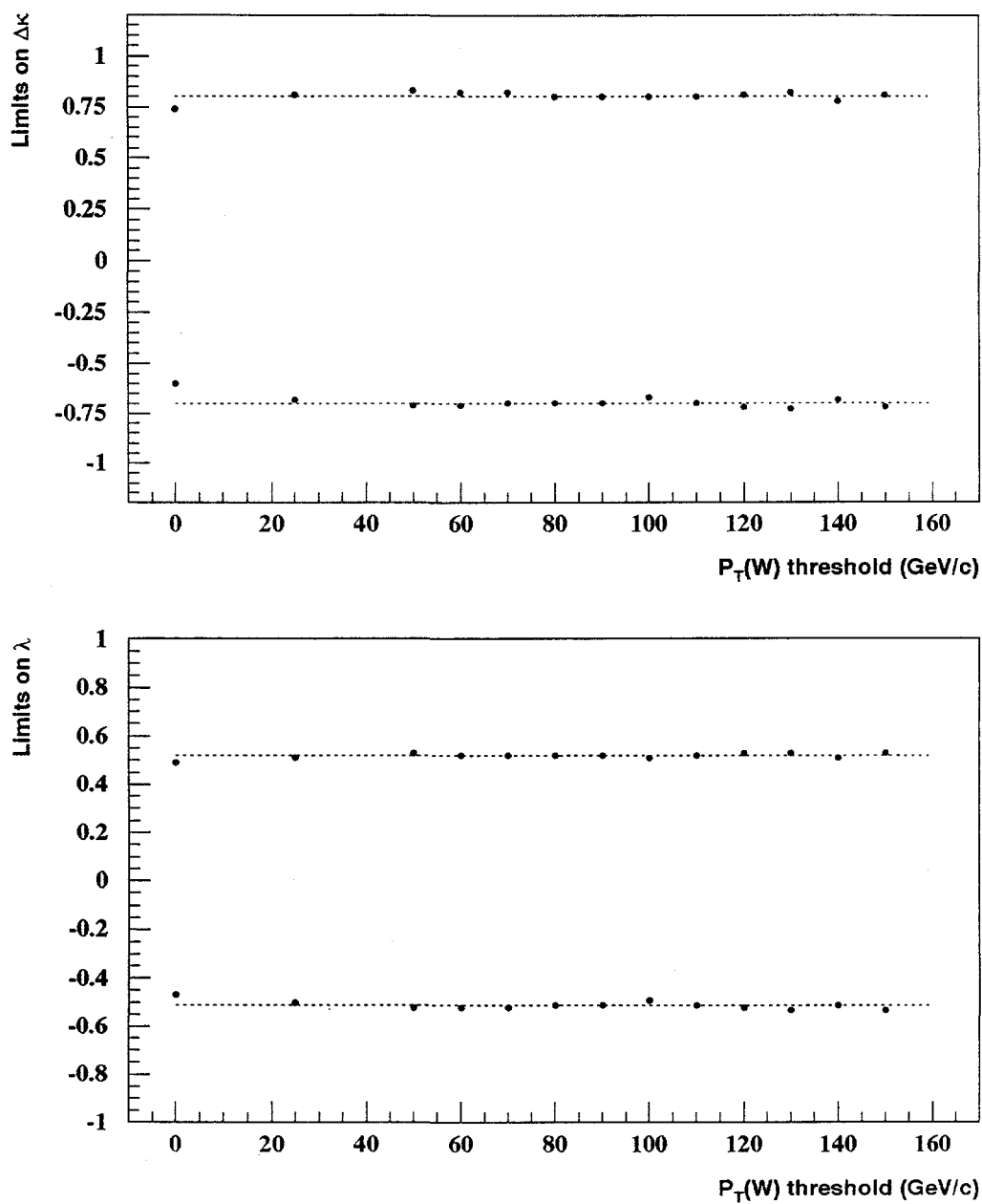
Figure 8.6: Limits on $\Delta\kappa$ (upper) and λ (lower) versus p_T^W threshold. The lines are just to guide the eye.

95% CL axis limits	Unitarity Limits	Λ_{FF} (TeV)
$-0.66 < \Delta\kappa < 0.90 \;\; (\lambda = 0)$	$|\Delta\kappa| < 2.62$	1.0
$-0.50 < \lambda < 0.53 \;\; (\Delta\kappa = 0)$	$|\lambda| < 1.85$	
$-0.56 < \Delta\kappa < 0.75 \;\; (\lambda = 0)$	$|\Delta\kappa| < 1.17$	1.5
$-0.42 < \lambda < 0.44 \;\; (\Delta\kappa = 0)$	$|\lambda| < 0.82$	
$-0.52 < \Delta\kappa < 0.70 \;\; (\lambda = 0)$	$|\Delta\kappa| < 0.66$	2.0
$-0.38 < \lambda < 0.42 \;\; (\Delta\kappa = 0)$	$|\lambda| < 0.46$	

Table 8.4: Limits from the p_T^W binned fit. The couplings for $WW\gamma$ are assumed to be the same as for WWZ.

Until now, we have assumed that the couplings $\Delta\kappa$ and λ for WWZ and $WW\gamma$ are equal. However, this is not the only possible relationship between them. In the literature we can find many other relations between the anomalous couplings that are derived from phenomenological arguments [21, 22]. Here we will study the sensitivity of one of them, the HISZ relations [21]. Those relations specify λ_Z, κ_Z, and g_{1Z} in terms of the independent variables λ_γ and κ_γ, thus reducing the number of independent WWV couplings from five to two:

$$\Delta\kappa_Z = \tfrac{1}{2}\Delta\kappa_\gamma(1 - \tan^2\theta_W)$$

$$\Delta g_Z = \tfrac{1}{2}\Delta\kappa_\gamma / \cos^2\theta_W$$

$$\lambda_Z = \lambda_\gamma$$

This subspace of anomalous couplings preserves $SU(2) \times U(1)$ gauge invariance and is not well constrained by indirect measurements, such as the Z studies at LEP [18]. The axis limits at 95% CL for these relations are shown in table 8.5. Fig. 8.7 shows the contour limits with $\Lambda_{FF} = 2.0$ TeV.
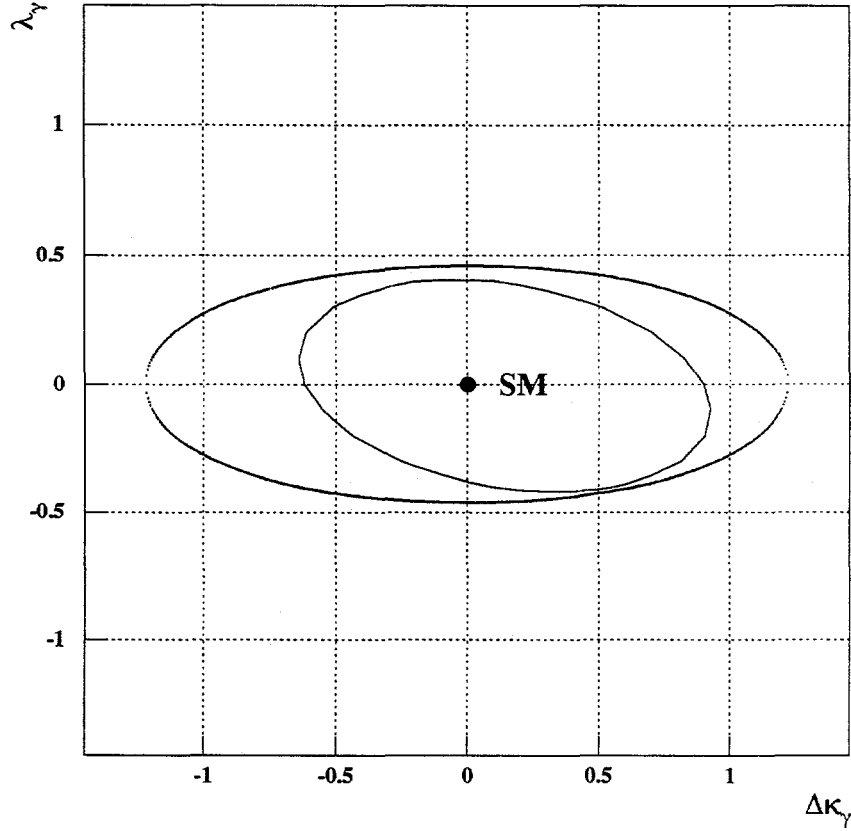
Figure 8.7: Limits at 95% CL (inner) on $\Delta\kappa_\gamma$ and λ_γ in the HISZ scenario. The outer contour is the unitary bound with $\Lambda_{FF} = 2.0$ TeV.

95% CL axis limits	Unitarity Limits	Λ_{FF} (TeV)
$-0.78 < \Delta\kappa_\gamma < 1.15 \ \ (\lambda_\gamma = 0)$	$|\Delta\kappa_\gamma| < 4.88$	1.0
$-0.50 < \lambda_\gamma < 0.53 \ \ (\Delta\kappa_\gamma = 0)$	$|\lambda_\gamma| < 1.85$	
$-0.68 < \Delta\kappa_\gamma < 0.98 \ \ (\lambda_\gamma = 0)$	$|\Delta\kappa_\gamma| < 2.17$	1.5
$-0.42 < \lambda_\gamma < 0.45 \ \ (\Delta\kappa_\gamma = 0)$	$|\lambda_\gamma| < 0.82$	
$-0.63 < \Delta\kappa_\gamma < 0.91 \ \ (\lambda_\gamma = 0)$	$|\Delta\kappa_\gamma| < 1.22$	2.0
$-0.39 < \lambda_\gamma < 0.42 \ \ (\Delta\kappa_\gamma = 0)$	$|\lambda_\gamma| < 0.46$	

Table 8.5: Limits at 95% CL for the HISZ relations.

Since the WWZ and $WW\gamma$ couplings are independent couplings, it is interesting to see the limits on one set of anomalous couplings when the other is set to their Standard Model values. Tables 8.6 and 8.7 summarize the axis limits at 95% CL for both assumptions: limits on ($\Delta\kappa_\gamma,\lambda_\gamma$) when SM WWZ is assumed, and limits on ($\Delta\kappa_Z,\lambda_Z$) when SM $WW\gamma$ is assumed. The results with the SM $WW\gamma$ assumptions are unique to $WW(WZ)$ production since the WWZ couplings are not accessible with $W\gamma$ production. The results also indicate that this analysis is more sensitive to WWZ couplings as expected from the larger overall couplings for WWZ than $WW\gamma$ and that it is complementary to the $W\gamma$ production process which is sensitive to the $WW\gamma$ couplings only. Fig. 8.8 shows the 95% CL for these two assumptions.

95% CL axis limits	Unitarity Limits	Λ_{FF} (TeV)
$-2.03 < \Delta\kappa_\gamma < 2.45 \ (\lambda_\gamma = 0)$	$\|\Delta\kappa_\gamma\| < 7.4$	1.0
$-1.54 < \lambda_\gamma < 1.58 \ (\Delta\kappa_\gamma = 0)$	$\|\lambda_\gamma\| < 3.9$	
$-1.79 < \Delta\kappa_\gamma < 2.12 \ (\lambda_\gamma = 0)$	$\|\Delta\kappa_\gamma\| < 3.3$	1.5
$-1.53 < \lambda_\gamma < 1.56 \ (\Delta\kappa_\gamma = 0)$	$\|\lambda_\gamma\| < 1.8$	
$-1.63 < \Delta\kappa_\gamma < 1.94 \ (\lambda_\gamma = 0)$	$\|\Delta\kappa_\gamma\| < 1.8$	2.0
$-1.38 < \lambda_\gamma < 1.44 \ (\Delta\kappa_\gamma = 0)$	$\|\lambda_\gamma\| < 1.0$	

Table 8.6: Axis limits at 95% CL when SM WWZ is assumed.

8.3   Combined Run 1 $e\nu jj$ Results

The limits on anomalous couplings presented in this thesis [74] are significantly tighter than our previous publication [14]. The main reason for the tighter limits is

95% CL axis limits	Unitarity Limits	Λ_{FF} (TeV)
$-0.86 < \Delta\kappa_Z < 1.12 \; (\lambda_Z = 0)$	$|\Delta\kappa_Z| < 3.35$	1.0
$-0.58 < \lambda_Z < 0.62 \; (\Delta\kappa_Z = 0)$	$|\lambda_Z| < 2.15$	
$-0.72 < \Delta\kappa_Z < 0.93 \; (\lambda_Z = 0)$	$|\Delta\kappa_Z| < 1.50$	1.5
$-0.49 < \lambda_Z < 0.51 \; (\Delta\kappa_Z = 0)$	$|\lambda_Z| < 0.96$	
$-0.67 < \Delta\kappa_Z < 0.87 \; (\lambda_Z = 0)$	$|\Delta\kappa_Z| < 0.83$	2.0
$-0.45 < \lambda_Z < 0.48 \; (\Delta\kappa_Z = 0)$	$|\lambda_Z| < 0.53$	

Table 8.7: Axis limits at 95% CL when SM $WW\gamma$ is assumed.
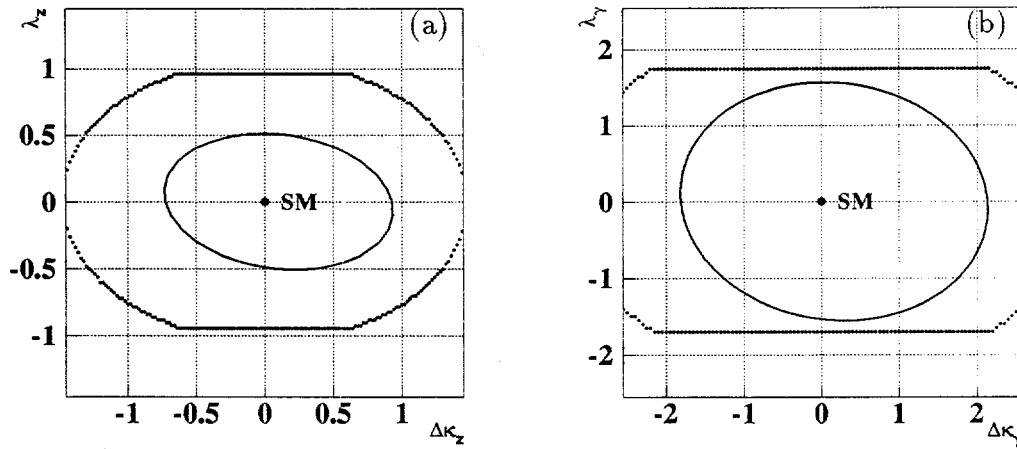
Figure 8.8: Contour limits on anomalous couplings parameters at 95% CL (inner curves) and unitarity limits (outer) with $\Lambda_{FF} = 1.5$ TeV, assuming (a) SM $WW\gamma$ couplings, and (b) SM WWZ couplings.

the increased statistics for Run 1B (about 6 times) in comparison with Run 1A, and

a better understanding of the backgrounds. We can obtain even tighter limits if we

combine the Run 1A and 1B results. The DØ $WW, WZ \rightarrow e\nu jj$ Run 1A analysis is

described in references [14, 75]. A summary of the signal and backgrounds for the two

different analyses [76] is shown in table 8.8.

	Run 1A	Run 1B
Luminosity	13.7 pb^{-1}	76.5 pb^{-1}
Backgrounds		
QCD Multijets	12.2± 2.6	104.3±12.3
QCD $W+ \geq 2$ jets	62.2±13.0	279.3±36.1
$t\bar{t} \rightarrow e\nu$ jjX	0.87±0.12	3.4± 1.2
$WW/WZ \rightarrow \tau\nu$ jj	0.22±0.02	$0.15^{+\ 0.16}_{-\ 0.08}$
Total Background	75.5±13.3	387.1±38.2
Data	84	399
SM $WW+WZ$ prediction	3.2±0.6	16.2±2.7

Table 8.8: Summary of $e\nu jj$ data and backgrounds for 1A and 1B.

Each of the two analyses can be considered as different experiments. Since
both experiments took place in the same detector, there are some correlated uncer-
tainties, such as uncertainties on theoretical prediction, luminosity calculation, and
lepton reconstruction and identification. Also the background estimate is common to
each experiment. Other uncertainties, such as uncertainties on the jet energy and effi-
ciencies, are uncorrelated. Combining limits is straightforward as long as one has all
the information and all these common systematics uncertainties are properly taken into
account. The uncertainties for both analyses are summarized in table 8.9. Each uncer-
tainty was weighted by the integrated luminosity in each experiment. Combining the
two results, we set the upper limit at 95% CL on the cross section $\sigma(p\bar{p} \rightarrow W^+W^-X)$
of 82.4 pb. Fig. 8.9 shows the combined spectra for p_T^W.

Source of Error	Run 1A	Run 1B
Common Systematic Uncertainties		
Luminosity uncertainty	5.4%	
QCD corrections	14%	
Electron and trigger efficiency	1.2%	
Statistics of fast MC	1%	
$\not{E}_T$ smearing	5.1%	
Total Common (σ_c)	15.9%	
Uncorrelated Systematic Uncertainties		
Jet energy scale	6%	3%
ISAJET vs. PYTHIA	9%	4%
Statistics for effic($W \to jj$)	4%	2%
Parametrization of prediction	4%	5%
Total Uncorrelated (σ_u)	12.2%	7.3%
Background Uncertainties		
All sources	13%	7%
Total Background (σ_b)	8%	

Table 8.9: Correlated and Uncorrelated systematic uncertainties for Run 1a and Run 1b $e\nu jj$ analysis.

To extract the limits on anomalous couplings we combine the results of the two analyses by calculating a combined likelihood function using the $p_T(e\nu)$ spectra. The individual uncertainties on the signal and backgrounds for each analysis are taken into account with the same Bayesian approach used above. Common systematics are further taken into account by convoluting the product of the two individual likelihood functions with a Gaussian distribution representing the common systematic uncertainty on both analyses as described by the equation:

$$P = \int \mathcal{G}_c dc \int \mathcal{G}_b db \left(\int \mathcal{G}_{u_{1a}} f_{1a} \, du_{1a} \otimes \int \mathcal{G}_{u_{1b}} f_{1b} \, du_{1b} \right)$$
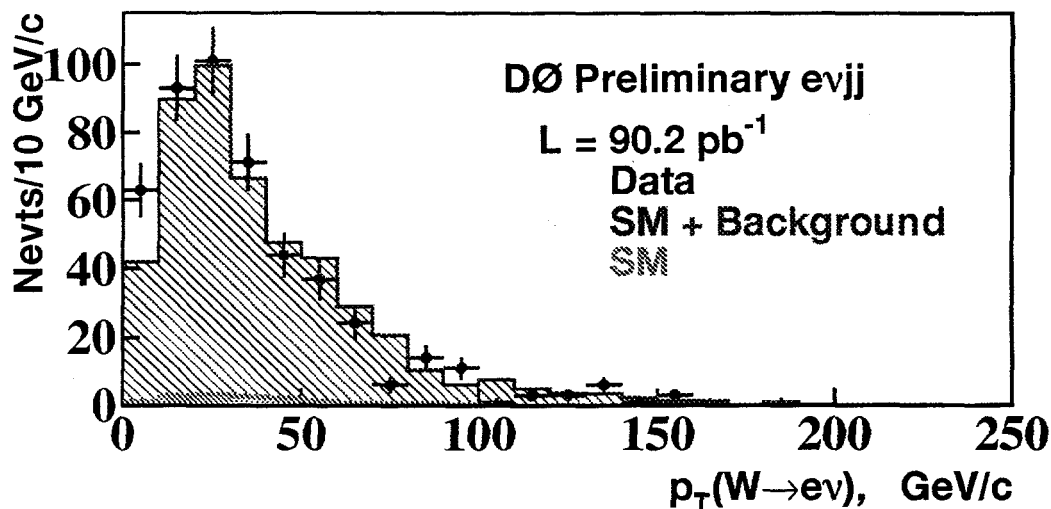
Figure 8.9: p_T^W spectrum for the 483 Run 1 $e\nu jj$ candidates. The points are data with 1σ error bars. The light-shaded histogram is the SM prediction plus the background estimates and the dark-shaded histogram is the SM prediction.

where $\mathcal{G}_c$ and $\mathcal{G}_b$ are the Gaussian distribution for the common and background uncertainties respectively, $\mathcal{G}_{u_{1a}}$ and $\mathcal{G}_{u_{1b}}$ are the Gaussian distribution for the uncorrelated error in each analysis, and f_{1a} and f_{1b} are the Poisson distribution for each analysis.

Couplings	$\Lambda_{FF} = 1.0$ TeV	$\Lambda_{FF} = 1.5$ TeV	$\Lambda_{FF} = 2.0$ TeV
$\lambda_{\gamma=Z}$	-0.43,0.46	-0.36,0.39	-0.34,0.37
$\Delta\kappa_{\gamma=Z}$	-0.57,0.81	-0.49,0.65	-0.44,0.60
λ_γ (HISZ)	-0.43,0.46	-0.37,0.39	-0.35,0.37
$\Delta\kappa_\gamma$ (HISZ)	-0.69,1.05	-0.58,0.87	-0.55,0.80
λ_γ (SM WWZ)	-1.30,1.35	-1.28,1.32	-1.15,1.22*
$\Delta\kappa_\gamma$ (SM WWZ)	-1.67,2.12	-1.48,1.78	-1.34,1.63
λ_Z (SM $WW\gamma$)	-0.49,0.53	-0.41,0.44	-0.38,0.41
$\Delta\kappa_Z$ (SM $WW\gamma$)	-0.76,1.02	-0.62,0.90	-0.56,0.74

Table 8.10: Axis limits at 95% CL with various assumptions for Run 1 Data.

The resulting, combined Run 1A and Run 1B, 95% CL contours are shown in Fig. 8.10. They are slightly improved limits compared with the result of the previous section. The 95% CL limits on the axes are listed in table 8.10. The comparison of the combined Run 1 limits with other experiments is given in the next chapter.

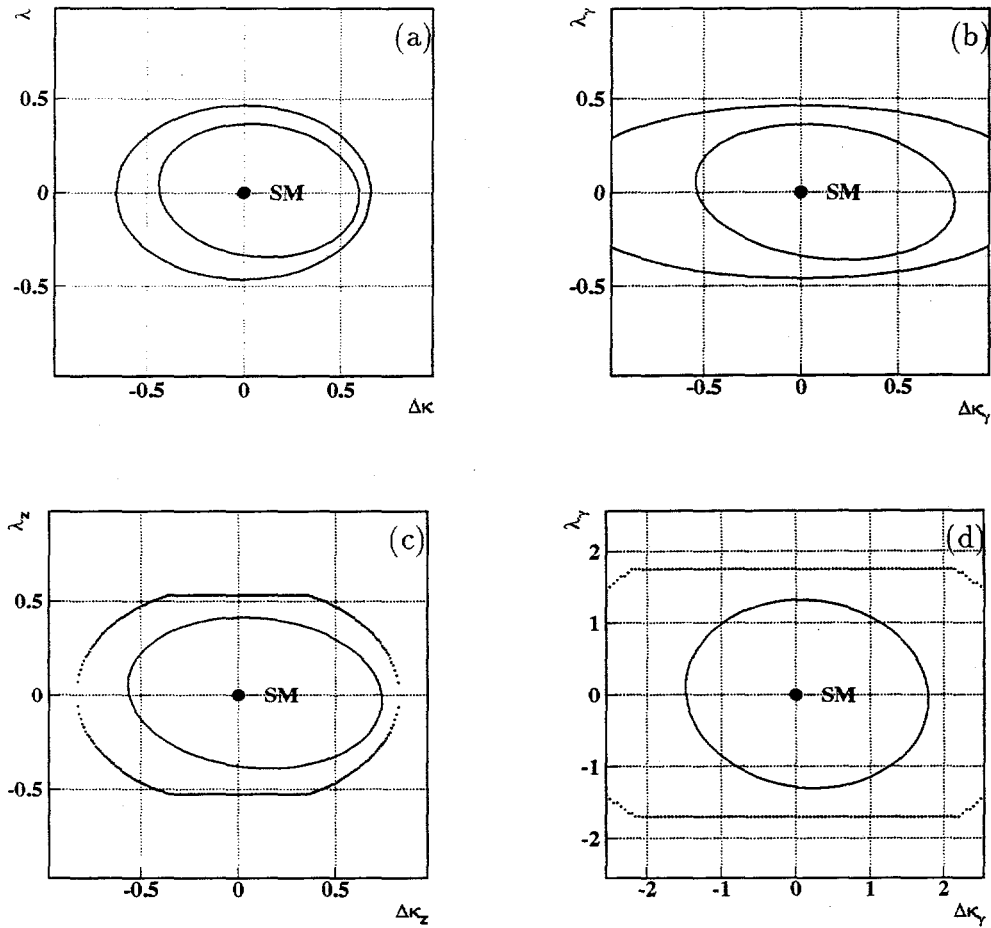Figure 8.10: Contour limits on anomalous couplings parameters at 95% CL (inner curves) and unitary bounds (outer curves), assuming (a) $\Delta\kappa \equiv \Delta\kappa_\gamma = \Delta\kappa_Z, \lambda \equiv \lambda_\gamma = \lambda_Z$; (b) HISZ relations; (c) SM $WW\gamma$, and (d) SM WWZ couplings. $\Lambda_{FF} = 2.0$ TeV is used for (a),(b) and (c); $\Lambda_{FF} = 1.5$ TeV is used for (d).

Chapter 9

Conclusions

A search for anomalous WW and WZ production in the $e\nu jj$ decay mode at $\sqrt{s} = 1.8$ TeV has been performed. In a total of 76.5pb^{-1} from the 1993-1995 Collider Run at Fermilab we have observed 399 candidate events with an expected background of 387.09 ± 39.75 events. The expected number of events for the SM WW/WZ production is 16.02 for this integrated luminosity. The sum of the SM prediction and the background estimates is consistent with the observed number of events, indicating that no new physics phenomena is seen. The 95% CL limit on the cross section $\sigma(p\overline{p} \to W^+W^- X)$ is calculated to be 93.8 pb, assuming the SM ratio of the cross sections of $p\overline{p} \to W^+W^- X$ and $p\overline{p} \to W^{\pm}ZX$. Comparing the p_T^W distributions of the observed signal with those from anomalous couplings predictions we have set limits on the $WW\gamma$ and WWZ anomalous couplings parameters $\Delta\kappa$ and λ. The preliminary limits under various assumptions are summarized in table 9.1.

Assumptions	Λ_{FF}	Limits on axes
$\Delta\kappa_\gamma = \Delta\kappa_Z$ $\lambda_\gamma = \lambda_Z$	1.5	$-0.56 < \Delta\kappa < 0.75$ $(\lambda = 0)$ $-0.42 < \lambda < 0.44$ $(\Delta\kappa = 0)$
HISZ	2.0	$-0.63 < \Delta\kappa_\gamma < 0.91$ $(\lambda_\gamma = 0)$ $-0.39 < \lambda_\gamma < 0.42$ $(\Delta\kappa_\gamma = 0)$
SM $WW\gamma$	1.5	$-0.72 < \Delta\kappa_Z < 0.93$ $(\lambda_Z = 0)$ $-0.49 < \lambda_Z < 0.51$ $(\Delta\kappa_Z = 0)$
SM WWZ	1.5	$-1.79 < \Delta\kappa_\gamma < 2.12$ $(\lambda_\gamma = 0)$ $-1.53 < \lambda_\gamma < 1.56$ $(\Delta\kappa_\gamma = 0)$

Table 9.1: Expected 95% CL limits on anomalous WWV $(V = \gamma, Z)$ couplings from Run 1B data.

The limits are significantly tighter than those from the same channel using the data from 1992-1993 Collider Run (13.7 pb^{-1}).

Assumptions	Λ_{FF}	Limits on axes
$\Delta\kappa_\gamma = \Delta\kappa_Z$ $\lambda_\gamma = \lambda_Z$	2.0	$-0.44 < \Delta\kappa < 0.60$ $(\lambda = 0)$ $-0.34 < \lambda < 0.37$ $(\Delta\kappa = 0)$
HISZ	2.0	$-0.55 < \Delta\kappa_\gamma < 0.80$ $(\lambda_\gamma = 0)$ $-0.35 < \lambda_\gamma < 0.37$ $(\Delta\kappa_\gamma = 0)$
SM $WW\gamma$	2.0	$-0.56 < \Delta\kappa_Z < 0.74$ $(\lambda_Z = 0)$ $-0.38 < \lambda_Z < 0.41$ $(\Delta\kappa_Z = 0)$
SM WWZ	1.5	$-1.48 < \Delta\kappa_\gamma < 1.78$ $(\lambda_\gamma = 0)$ $-1.28 < \lambda_\gamma < 1.32$ $(\Delta\kappa_\gamma = 0)$

Table 9.2: Expected 95% CL limits on anomalous WWV $(V = \gamma, Z)$ couplings from Run 1 Data.

The two results were combined and the 95%CL limit on the cross section for WW productions was set to 82.4 pb. The limits on anomalous coupling parameters improved significantly. These preliminary limits are shown in table 9.2. They are

essentially the same as those from CDF [10], but we use only the $e\nu jj$ channel and
they have used all the semileptonic channels available. Figures 9.1 and 9.2 compare
the limits on the couplings parameters with the CDF preliminary limits.

Figure 9.1: Comparison of the 95% CL limits on $\Delta\kappa$ and λ from this experiment with
the preliminary CDF results. The CDF results use $WW, WZ \rightarrow$ leptons+jets events
found in 110 pb^{-1} of data. The equal scenario is assumed ("$Z = \gamma$").

An extra improvement of 25% is expected when we combine the limits of this
work with the $\mu\nu jj$ and $eejj$ results from Run 1B, which is currently in progress

assuming no significant deviations from the Standard Model are observed.
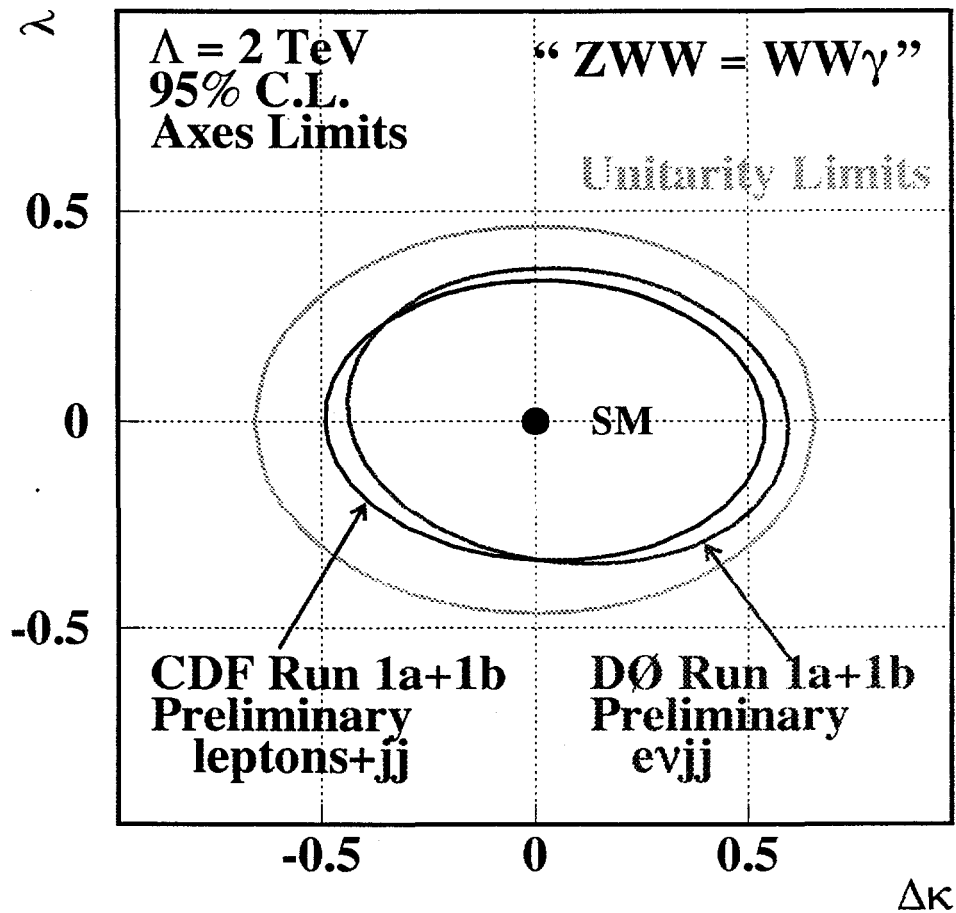

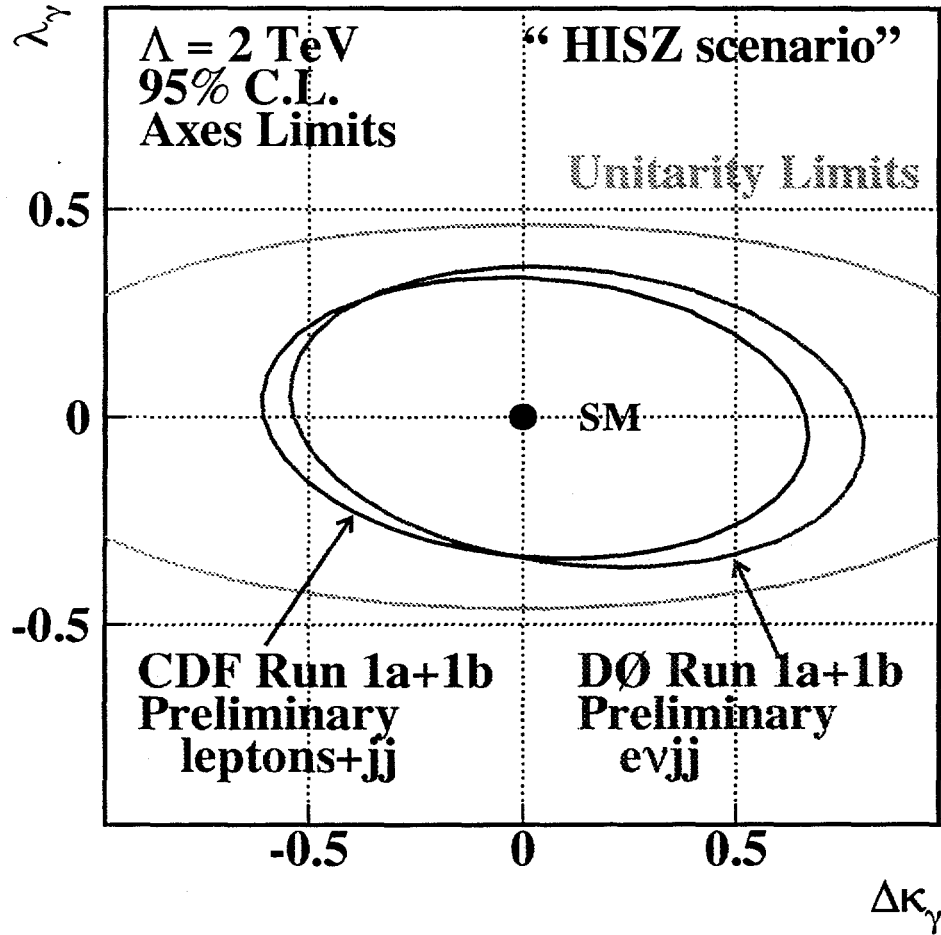Figure 9.2: Comparison of the 95% CL limits on $\Delta\kappa$ and λ from this experiment with the preliminary CDF results. The HISZ scenario is assumed.

Assuming that the Standard Model is correct, more drastic improvements in the limits of anomalous couplings are expected when more data and/or higher center-of-mass energies become available at future experiments such as LEP II, LHC, and the upgraded Tevatron.

Appendix A

An alternative Estimation of QCD Multijets Background

The QCD-FAKE background to $W \to e\nu$ signals can be estimated in a manner which is independent of the study performed in section 6.1. The technique has been used in other analyses [66, 67] with very good results. Here we will briefly describe the method.

Suppose that we start with some set of data. Event selection cuts are applied to this sample, dividing it into events that pass some set of cuts (good events, N_g) and events that fail the cuts (bad events, N_b), like in Fig. 6.1.

$$\text{Total} = N_g + N_b$$

each sample contains some signal (S) and some background (B), such that:

$$N_g = S_g + B_g$$

$$N_b = S_b + B_b$$

Our objective is to measure B_g. To achieve this we must remember that the quality cuts applied to the samples have some efficiency associated with them (ϵ), which can be easily extracted from data as described in chapter 7. But there is also an efficiency associated with the quality cuts applied to the background (r) which can be measured; for instance from the events with $\not{E}_T <$ 15 GeV. Therefore, since an efficiency is defined as the the number of events that pass a quality cut over the original number of events

$$\epsilon \rightarrow \frac{S_g}{S_g + S_b} \qquad r \rightarrow \frac{B_g}{B_g + B_b}.$$

Now we have four unknowns (S_g, B_g, S_b, B_b) and four measurable quantities (N_g, N_b, ϵ, r). It is possible to resolve for any of the unknowns in terms of the measurable quantities. In particular we are interested in

$$S_g = \left(N_g + N_b - \frac{N_g}{r} \right) \left(\frac{\epsilon r}{r - \epsilon} \right)$$

$$B_g = \left(N_g + N_b - \frac{N_g}{\epsilon} \right) \left(\frac{\epsilon r}{\epsilon - r} \right).$$

If we apply this technique to our analysis we found 98.9 ± 7.65 events. This estimation agrees with the standard method one, 104.3 ± 8.2 events, described in chapter 6. The differences are within 5%, as we can seen from the p_T^W spectrum in figure A.1. This difference is included as systematic uncertainty in the background estimates.
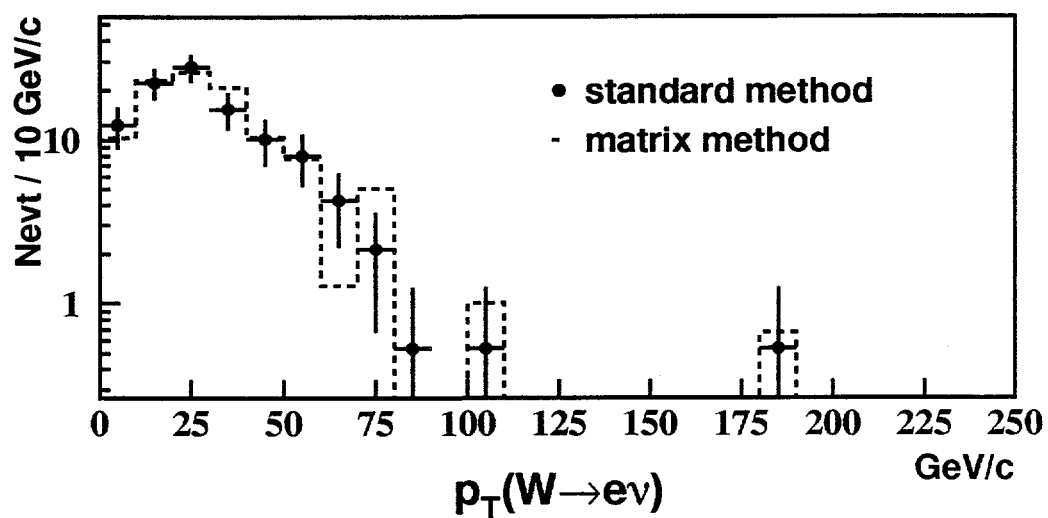
Figure A.1: Comparison of the standard method and the matrix method to estimate the QCD–FAKE background.

Bibliography

[1] S.L. Glashow, Nucl. Phys. **22**, 579 (1961);

S. Weinberg, Phys. Rev. Lett. **19**, 1264 (1967);

A. Salam, *Elementary Particle Theory*, ed. N. Svartholm (Almquist and Wiksells, Stockholm, 1969) p. 367.

[2] D.H. Perkins, "Introduction to High Energy Physics" Addison-Wesley, (1987).

[3] Contemporary Physics Education Project, "The Particle Adventure", (1996), (URL: http://www-pdg.lbl.gov/cpep/adventure.html).

[4] C. Quigg, "Gauge Theories of Strong, Weak, and Electromagnetic Interactions", Addison-Wesley, (1983).

[5] V. Barger and R. Phillips, "Collider Physics", Frontiers In Physics Lecture Note Series, Addison-Wesley, (1987).

[6] R.M. Barnett, *et al.* (The Particle Data Group), Phys. Rev. **D54**, 65,85,207,210 (1996).

[7] G. t'Hooft, Nucl. Phys. **B33**, 173 (1971);Nucl. Phys. **B35**, 167 (1971).

[8] F. Abe, *et al.*, (CDF Collaboration), Phys. Rev. Lett. **74**, 1936 (1995).

[9] F. Abe, *et al.*, (CDF Collaboration), Phys. Rev. Lett. **74**, 1941 (1995).

[10] F. Abe, *et al.*, (CDF Collaboration), Phys. Rev. Lett. **75**, 1017 (1995);

L.J. Nodulman, in Proccedings of the 28th International Conference on High Energy Physics (ICHEP96), Warsaw, Poland 1996, FERMILAB-Conf-96/326-E.

[11] S. Abachi, *et al.*, (DØ Collaboration), Phys. Rev. Lett. **75**, 1023 (1995).

[12] S. Abachi, *et al.*, (DØ Collaboration), Phys. Rev. Lett. **75**, 1028 (1995).

[13] S. Abachi, *et al.*, (DØ Collaboration), Phys. Rev. Lett. **75**, 1034 (1995).

[14] S. Abachi, *et al.*, (DØ Collaboration), Phys. Rev. Lett. **77**, 3303 (1996).

[15] S. Abachi, *et al.*, (DØ Collaboration), "Limits on Anomalous $WW\gamma$ Couplings from $p\bar{p} \rightarrow W\gamma X$ Events at $\sqrt{s} = 1.8$ TeV", submitted to *Phys. Rev. Lett.*

[16] K. Hagiwara, *et al.*, Phys. Rev. **D41**, 2113 (1990);

J. Ohnemus, Phys. Rev. **D44**, 1403 (1991).

[17] R.W. Brown and K.O. Mikaelian, Phys. Rev. **D19**, 922 (1979);

R.W. Brown, D. Sahdev, and K.O. Mikaelian, Phys. Rev. **D20**, 1164 (1979).

[18] D. Schaile, "Precision Data from LEP", Proceedings of the International Conference on Vector Boson Self-Interactions, ed. by U. Baur, *et al.*, AIP (1995).

[19] K. Hagiwara, *et al.*, Nucl. Phys. **B282**, 253 (1987).

[20] W.J. Marciano and A. Queijeiro, Phys. Rev. **33**, 3449 (1986).

[21] K. Hagiwara, *et al.*, Phys. Rev. **D48**, 2182 (1993).

[22] P. Hernández, "Triple Gauge Couplings: Does Lep-1 obviate Lep-2", Proceedings of the International Conference on Vector Boson Self-Interactions, ed. by U. Baur, *et al.*, AIP (1995).

[23] K. Kim and Y-S. Tsai, Phys. Rev. **D7**, 3710 (1973).

[24] U. Baur and D. Zeppenfeld, Phys. Lett. **B201**, 383 (1988).

[25] U. Baur, E.L. Berger, Phys. Rev. **D41**, 1476 (1990).

[26] H. Georgi, *et al.*, Phys. Rev. Lett. **40**, 692 (1978).

[27] M.J. Duncan, *et al.*, Nucl. Phys. **B272**, 517 (1986).

[28] J. Alitti, *et al.*, (UA2 Collaboration), Phys. Lett. **B277**, 194 (1992).

[29] J. Thompson, "Introduction to Colliding Beams at Fermilab," DØ Note 2367, FERMILAB-TM-1909 (1994) unpublished.

[30] S. Abachi, *et al.* (DØ Collaboration), Nucl. Instr. Meth. **A338**, 185 (1991). S. Snyder, "The DØ Detector," DØ note 2500 (1995) unpublished.

[31] J. Bantly, *et al.*, IEEE **41**, 1274 (1994).

[32] N. Amos, *et al.*, (E710 Collaboration), Phys. Lett. **B243**, 158 (1990);

F. Abe, *et al.* (CDF Collaboration), Phys. Rev. **D50**, 5518 (1994).

[33] J. Bantly, *et al.* "Improvement to the DØ Luminosity Constant", DØNote 2544 (1995) unpublished.

[34] M. Abolins, *et al.*, Nucl. Instr. Meth. **A289**, 543 (1990).

[35] M. L. Kelly, "Test of the Standard Model of Electroweak Interactions by measuring the Anomalous $WW\gamma$ Couplings at $\sqrt{s} = 1.8$ TeV", Ph. D. Thesis, Notre Dame (1996).

[36] J. Thompson, DØ News 3124 WZ folder (1996).

[37] DØ Collaboration, "DØ Sofware Documentation",

(URL: http://d0sgi0.fnal.gov/software/software.html).

[38] M. Goosens, *et al.*, CERN Library Program No. Q100 (1991).

[39] I. Adam, *et al.* "The Micro DST Format", DØ note 2327 (1994) unpublished.

[40] D. Zhao, "PAW and PIAF server at DØ",

(URL: http://d0sgi0.fnal.gov/software/challenge/paw_piaf.html).

[41] D. Casey, *et al.* "QCD/WZ Ntuples", DØ note 3124 (1996) unpublished.

[42] DØ Collaboration, M. Narain, in Proceedings of 7th Meeting of the American Physical Society Division of Particles and Fields, Fermilab, Nov. 1992, *edited by*

C. Albright, P. Kasper, R. Raja, and J. Yoh; FERMILAB-Conf-93/054-E, 1992; DØ Conf-92-25.

[43] S. Abachi, *et al.*, (DØ Collaboration) Phys. Rev. **D52**, 4877 (1995).

[44] R. Raja, "H Matrix anlaysis of top $\rightarrow$ lepton + jets", McPhysics Workshop II, DØ note 1192 (1991) unpublished.

[45] U. Heintz, "A Measurement of the Calorimeter Response Using π^0 Decays", DØ Note 2268 (1994) unpublished.

[46] I. Adam, *et al.*, "Observation of J/psi to ee Decays at DØ", DØ note 2481 (1994) unpublished.

[47] S.Abachi, *et al.*, (DØ Collaboration) Phys. Rev. Lett. **77**, 3309 (1996).

[48] S. M. Glenn, "A search for Self-Interactions of Neutral Electroweak Gauge Bosons", Ph. D. Thesis, UC Davis (1996).

[49] R. V. Astur, "Study of Fake Jets in the DØ Detector", DØ note 1662 (1993) unpublished.

[50] V. D. Elvira, J. Blazey and R. Astur; "A Study of Standard Jet Cuts and their Efficiencies Using DØ Collider Data", DØ note 1763 (1993) unpublished.

[51] R. Astur, "On Correcting jets by Correcting the Electromagnetic and Hadronic Calorimeters Separately", DØ note 2575 (1995) unpublished.

R. Astur and R. Kehoe, "Determination of the Hadronic Energy Scale of DØ Calorimetry", DØ note 2908 (1996) unpublished.

[52] F. Hsieh and H. Lan, "Post-CAFIX jet Corrections for Top Mass Analysis", DØ note 3055 (1996) unpublished.

[53] F. Paige and S. Protopopescu, BNL Report BNL38034, (1986) unpublished. release V7.13

[54] T. Sjöstrand, Computer Physics Commun **82**, 74 (1994).

[55] G. Marchesini *et al.*, Computer Physics Commun **67**, 465 (1992).

[56] W. Giele, E. Glover and D. Kosower, Nucl. Phys. **B403**, 633 (1993).

[57] J. Womersley FERMILAB-Conf-92/306, Proceedings of the XXVI International Conference on H.E.P, Dallas, August 1992.

[58] S. Glenn, "A Parametric Detector Simulation for Dibosons", DØ Note 2846 (1996) unpublished.

[59] F. Carminati *et al.*, "GEANT Users Guide," CERN Program Library, (1991) unpublished.

[60] H.L. Lai, *et al.*, (CTEQ Collaboration) Phys. Rev. **D51**, 4763 (1995).

[61] D. Duke and J. Owens, Phys. Rev. **D30**, 49 (1984).

[62] J. Tarazi, DØ News 306 and 389 WZ folder (1995).

[63] W. Carvalho and T. Taylor, "Multiple Interaction Tool Study for Run 1", DØ note 2798 (1995) unpublished.

[64] S. Chopra and M. Narain, "Determination of QCD backgrounds in e+jets events" DØ note 2105 (1994) unpublished.

[65] T. Joffe-Minor, "A Measurement of the Ratio of $W + 1$ Jet to $W + 0$ Jets Cross Sections and Comparisons to QCD " DØ note 3019 (1996) unpublished.

[66] G. Manning, "Estimation of the background to W+jets and Z+jets", DØ Note 2452 unpublished;

B. Cobau, private communication.

[67] M. Kelly, "Prospects for a $Z \to \tau\tau$ Analysis", DØ Note 3113 (1996) unpublished.

[68] M. Narain (for the DØ Collaboration), presented at 1996 Recontre de Physique de la Vallée d'Aoste, La Thuile, Italy (Mar 1996), DØ Conf-96-5.

[69] J. Botts, *et al.*, (CTEQ Collaboration) Phys. Lett. **B304**, 159 (1993).

[70] J. Cortés, *et al.*, Nucl. Phys. **B278**, 26 (1986).

[71] R. Partridge, "Top Limit Calculation", DØ note 1806, (1993) unpublished.

[72] B. P. Roe, "Probability and Statistics in Experimental Physics", Springer-Verlag, New York (1992).

H. Cramer, "Mathematical Methods of statistics", Princeton University Press, (1946).

[73] G. Landsberg, in Proc. Workshop on Physics at Current Acceleratos and the Supercollider, ANL-HEP-CP-93-92, 303 (1992) unpublished;

G. Landsberg, "Test of the Standard Model of Electroweak Interactions by Measuring the Anomalous $ZZ\gamma$ and $Z\gamma\gamma$ Couplings ", Ph. D. Dissertation, SUNY @ Stony Brook (1994).

[74] A. Sánchez-Hernández, "Experimental bounds on $WW, WZ \to e\nu jj$ production at DØ", DØ note 3129 (1996) unpublished.

[75] L. P. Chen, "Study of $WW\gamma$ and WWZ coupling with WW and $WZ \to e\nu jj$ events at DØ", DØ notes 2424, 2424A, 2424B, 2424C, and 2424D (1995) unpublished.

[76] A. Sánchez-Hernández, "Combined Run 1 $e\nu jj$ Results", DØ note 3144 (1997) unpublished.